ISTANBUL TECHNICAL UNIVERSITY ★ GRADUATE SCHOOL OF SCIENCE ENGINEERING AND TECHNOLOGY

RECEPTOR-TARGETED CARBON NANOTUBES AS NANOMATERIALS FOR DIAGNOSTICS AND TARGETED TREATMENT OF CANCER

Ph.D. THESIS

Mehdi PARTOVI MERAN

Department of Chemical Engineering

Chemical Engineering Programme

SEPTEMBER 2019

ISTANBUL TECHNICAL UNIVERSITY ★ GRADUATE SCHOOL OF SCIENCE ENGINEERING AND TECHNOLOGY

RECEPTOR-TARGETED CARBON NANOTUBES AS NANOMATERIALS FOR DIAGNOSTICS AND TARGETED TREATMENT OF CANCER

Ph.D. THESIS

Mehdi PARTOVI MERAN
(506112007)

Department of Chemical Engineering

Chemical Engineering Programme

Thesis Advisor: Prof. Dr. Fatma Seniha GÜNER

SEPTEMBER 2019

ISTANBUL TEKNİK ÜNİVERSİTESİ ★ FEN BİLİMLERİ ENSTİTÜSÜ

KANSER TEŞHİS VE TEDAVİSİ İÇİN RESEPTÖR-HEDEFLİ KARBON NANOTÜP NANOMALZEMELERİN GELİŞTİRİLMESİ

DOKTORA TEZİ

Mehdi PARTOVI MERAN
(506112007)

Kimya Mühendisliği Anabilim Dalı

Kimya Mühendisliği Programı

Tez Danışmanı: Prof. Dr. Fatma Seniha GÜNER

EYLÜL 2019

Mehdi PARTOVI MERAN, a Ph.D. student of İTU Graduate School of Science Engineering and Technology student ID 506112007 successfully defended the thesis/dissertation entitled "RECEPTOR-TARGETED CARBON NANOTUBES AS NANOMATERIALS FOR DIAGNOSTICS AND TARGETED TREATMENT OF CANCER", which he prepared after fulfilling the requirements specified in the associated legislations, before the jury whose signatures are below.

Thesis Advisor :   **Prof. Dr. F. Seniha GÜNER**   ....
Istanbul Technical University

Jury Members :   **Prof. Dr. Gürkan HIZAL**   ....
Istanbul Technical University

Prof. Dr. Sevil YÜCEL   ....
Yildiz Technical University

Assoc. Prof. Dr. Serap DERMAN   ....
Yildiz Technical University

Asst. Prof. Dr. Özge KÜRKÇÜOĞLU   ....
Istanbul Technical University

Date of Submission : 12 July 2019
Date of Defense   : 09 September 2019

To my parents,

FOREWORD

I would like to express my profound gratitude to my supervisor, Prof. Dr. F. Seniha Güner. I am very grateful for her permanent support, scientific guidance, constant optimism and encouragement throughout this long walk.

I am also very glad and thankful for having met and worked with Prof. Dr. Gürkan Hızal from the ITU Department of Polymer Science and Technology, for his willing collaboration and advices offering a valuable interdisciplinary view.

I am also very grateful to Prof. Dr. Nilgün Karatepe Yavuz from the ITU Energy Institute for providing SWNTs and important considerations and suggestions in order to improve the quality of the thesis study.

I would like express a special appreciation to Asst. Prof. Dr. Ayşe Özge KÜRKCÜOĞLU LEVİTAS for the very important contributions that enriched the molecular dynamics simulation studies, all the dedication, patience and support.

I deeply appreciate and thank the collaboration from Asst. Prof. Dr. Ayhan Ünlü from Istanbul University and Trakya University for providing all the necessary means for the *in vitro* and *in vivo* experiments, the good advices, cheerful mood and support whenever needed.

I also would like to thank my friends, Dilek DALGAKIRAN, Elif BAYSAK, Bircan DİNÇ, Banu ARABACIOĞLU, Fulya GÜLMEZ and Gizem KELEŞ, for their valuable help and advices, specifically. The gerat time we worked together is definitely one of the most beautiful memories. I will never forget their supports.

Finally, I wish to express my love and my gratitude to my family for their constant support, encouragement, never-ending patience, without whose love, this work would never be possible.

September 2019   Mehdi PARTOVI MERAN
                                                                    (M.S. Chemical Engineer)

x

TABLE OF CONTENTS

ABBREVIATIONS

CNT	**:**	Carbon Nanotubes
SWNT	**:**	Single Walled Carbon Nanotubes
MWNT	**:**	Multi Walled Carbon Nanotubes
PEG	**:**	Polyethyelen Glycole
NIR	**:**	Near Infrared
pyr	**:**	Pyrene
FTIR	**:**	Fourier Transform Infrared Spectroscopy
TGA	**:**	Thermogravimetric Analysis
^{1}HNMR	**:**	Proton Nuclear Magnetic Resonance
GS	**:**	Gas Chromatography
DOX	**:**	Doxorubicin
FA	**:**	Folic Acid
RDF	**:**	Radial Distribution Function
CDC	**:**	Centers for Disease Control and Prevention
NNI	**:**	National Nanotechnology Initiative
DMAP	**:**	Dimethylaminopyridine

SYMBOLS

$\vec{f_i}$ **:** Force

m **:** Mass

μ **:** Chemical Potential

$\vec{a_i}$ **:** Acceleration

σ_{ij} **:** Potential Energy

Ω **:** Microcanonical

Q   **:** Canonical

Δ **:** Isobaric-isothermal

Θ **:** Capacitive reactance

ω **:** RBM Band Property

E_b **:** Binding Energy

ρ **:** Density

N   **:** Number of Molecuels

δ **:** Kronecker delta

r_i **:** Position Vector

LIST OF TABLES

LIST OF FIGURES

RECEPTOR-TARGETED CARBON NANOTUBES AS NANOMATERIALS FOR DIAGNOSTICS AND TARGETED TREATMENT OF CANCER

SUMMARY

Heart disease and cancer are the first and second leading causes of deaths in the world for more than a decade. However, the statistics from the American Cancer Society show that cancer death rate has dropped progressively over the past 25 years in the United States. The decline in cancer mortality is attributed to the gradually drops in smoking and developments in early diagnostics and treatment. Uncontrolled and rapidly growth of cells in the body results in cancer tissues. Appearance of cancer tumor in one part of body may spread to other organs in case of late detection and treatment. Breast cancer is one of the diseases with mortality rate among women. In this regard, treatment of cancer with drug delivery systems offer great advantages over the conventional drug applications.

The objective of this study, was to develop receptor targeted carbon nanotube based nanocarrier with optimized properties for breast cancer therapy. Due to the outstanding physical, chemical, optical and NIR fluorescence properties, carbon nanotubes have been widely investigated as nanocarrier. Single walled carbon nanotubes (SWNTs) were used to compose the key part of the designed system. Two different single walled carbon nanotubes (short and long) were utilized to develop the nanocarrier. After fabrication of nanotubes, purification process was applied to the SWNTs in order to remove impurities from the samples. Thereafter, to incorporated biocompatibility to the nanocarriers, poly ethylene glycol (PEG) as biocompatible polymer was used. Owing to its hydrophilicity, this polymer can provide the required biocompatibility to the nanocarriers. Four different PEG polymers in terms of length were prepared to coat both SWNTs. PEG_{2000}, PEG_{5000}, $PEG12_{000}$ and branched PEG_{5000} were prepared in the first step. The start point in the synthesis process was methoxy PEG. In next step, these PEG polymers were converted to PEG-COOH. In the next step, noncovalent approach was employed for surface modification of SWNTs. An esterification reaction between PEG-COOH and pyrene methanol was taken place in order to obtain pyrene bearing PEG. In the final step, physical coating of the SWNTs were successfully achieved by utilizing of the mentioned pyrene bearing PEGs. ^{1}HNMR, FTIR, TGA, UV-vis and fluorescence spectroscopy analysis were performed to characterize the synthesized samples. The result of TGA analysis indicated that the amount of PEG binding to short SWNTs was higher than long SWNTs. To gain primary insight into the biocompatibility of the fabricated nanocarriers, in vitro cytotoxicity and in vivo blood circulation time assays were conducted for PEGylated SWNTs. The results of in vitro cytotoxicity for PEGylated short and long SWNTs exhibited that short SWNTs have higher cell viability with respect to long SWNTs samples. Moreover, as the molecular weight of PEG polymer decreased cell viability reduced due to inhibition cell proliferation. Confocal fluorescence microscopy imaging confirmed the results in vitro cytotoxicity. In the next step, in vivo blood circulation time studies were carried out on mice. Interestingly, branched PEG_{5000} coated SWNTs showed higher blood circulation time with near to 13 hours.

In the next phase of the study, Doxorubicin (DOX) as an anticancer agent was used to load to the SWNTs. In the study, DOX loading studies were conducted in two step. At first step, short and long SWNTs were dissolved in buffer solutions with different pH to understand its effect on the amount of DOX loading. UV–vis spectrometer was used to explore the amount of DOX loading and release. To gain a clear understanding to the characteristic peak of DOX wavelength scan was conducted between 350-650 nm. It is observed that 490 nm can be exploited for further studies. Accordingly, 490 nm was used for DOX loading and release studies.

In order to impart receptor-targeted feature to the samples, Folic Acid (FA) was employed as ligand. Folic acid (FA) functionalized SWNTs are promising carbon based nanocarriers for targeted delivery of biomolecules to tumor sites. FA is a type of B vitamin that as medication can be used in the treatment folic acid deficiency. FA has high affinity to the folate receptor α (FR-α) and binds to folate receptors that overexpressed on the surface of many types of cancer cells.

One of the low molecular weight agents that have been used extensively with PEGylated SWNTs as nanoplatfrom for therapy purpose is DOX. DOX is a chemotherapy medication drug used for the treatment of various types of cancer such as breast cancer, esophageal carcinomas, acute lymphocytic leukemia, bladder cancer and lymphoma since late 1960s. To improve the pharmacokinetics and bioavailability of this anticancer drug, several studies have been conducted in order to enhance the efficiency of the DOX. After incorporation of pyrene-FA to SWNTs, PEGylation of the samples were conducted and finally, DOX molecules were introduced to the nanocarriers.

The loading of DOX at different pH values to the short and long SWNTs exhibited that basic pH 9 led to higher DOX loading onto SWNTs. The release performance of the nanocarriers were performed in physiological pH 7.4 and acid pH 5.4 to mimic the intracellular environment. The results showed the all samples have higher release rate at pH 5.4 with respect to pH 7.4. Moreover, FA-conjugated SWNTs nanocarriers showed higher release rate at both pH. In the final step, in vitro cytotoxicity were conducted for the DOX loaded SWNTs samples. It was observed that FA-conjugated SWNTs have lower cell viability with respect to nonFA-conjugated SWNTs.

In vast majority of the studies that have been conducted regarding CNTs, these nanostructures were considered as perfect arrangement of carbon atoms in aromatic cylindrical settings. However, through the nucleation and growth process and also exposing to the electron irradiation these nanomaterials inescapably hold structural defects. Undoubtedly, the density and site of these structural defects may have substantial impact on their unique physical, chemical electrical and mechanical properties. Therefore, it is very crucial to address this fundamental issue in CNTs with structural defects.

Despite the outstanding promise of non-covalently coated SWNTs for biomedical imaging and molecular therapy applications, a quantitative understanding of structural defects on the non-covalent interactions is lacking. In previous chapters, short and long SWNTs were used in in vitro and in vivo studies. However, it is believed that through the growth and purification phase of the SWNTs production, it is not avoidable to achieve defect-free SWNTs. Consequently, in this chapter, we will investigate the effect of defect bearing SWNTs on van der Waals interaction between nanotubes and pyrene bearing structures. Accordingly, to explore the role of π-stacking interaction in defect bearing SWNTs, molecular dynamics and experimental studies were conducted

with a set of hydroxyl and carboxyl functionalized compounds designed to adsorb onto the SWNT sidewalls.

We introduce a multisegment SWNT model consisting of pristine, Stone-Wales defects bearing, and carboxyl functionalized/ Stone-Wales defects bearing SWNTs to theoretically and experimentally explore SWNTs behaviors with structural defects. In the model, the mentioned segments were separately created in Material Studio 8.0 software and each segment of the model was allowed to interact with strongly polar organic groups in aqueous medium. Therefore, in the last part of the study, an integration investigation on the effect of topological Stone-Wales defects on SWNTs on the amount of binding pyrene bearing compound were conducted.

The rearrangement of two π-bonded carbon atoms in CNTs, fullerenes and graphene creates a crystallographic defect, which is supposed to have important impact on the chemical, electrical, and mechanical properties of these materials. Topological Stone-Wales (SW) defects can be formed by changing the connectivity of C-C bonds in the SWNT sidewall by rotating them 90°. This rotating leads to the formation of two pentagons connected by two heptagons with a 5-7-7-5 topological defect. First, molecular dynamic studies were performed on SWNTs with defect-free, defect bearing nonfunctionalized and –COOH functionalized. Pyrene-COOH, pyrene-$(OH)_2$ and pyrene-OH as coating compounds were used. The results binding energy and Radial Distribution Function (RDF) showed that pyrene-COOH can establish higher H-bond with water molecules therefore, are able to disperse SWNTs in the aqueous medium. Moreover, defect bearing –COOH functionalized SWNTs due to the disruption on their aromaticity may not provide effective π-π stacking with aromatic molecules such as pyrene. Therefore, binding of pyrene to the surface of SWNTs in not stable. In the final part, pyrene-COOH, pyrene-$(OH)_2$ and pyrene-OH compounds were synthesized and were employed for physical coating of SWNTs. As expected pyrene-COOH coated SWNTs provided higher dispersion for the fabricated nanocarriers.

KANSER TEŞHİS VE TEDAVİSİ İÇİN RESEPTÖR-HEDEFLİ KARBON NANOTÜP NANOMALZEMELERİN GELİŞTİRİLMESİ

ÖZET

Kanser, küresel ölçekte ölüm sebeplerinin başında gelmektedir ve vücuttaki hücrelerin hem kontrolsüz hem de hızla büyümesi kanser dokularının oluşmasına neden olmaktadır. Kanser tümörünün geç tanı ve tedavisi durumunda, tümörün vücudun diğer kısımlarına yayılabilmesi olağandır. Meme kanseri, kadınlar arasında ölüm oranı yüksek olan hastalıklardan biridir. Bu bakımdan, kanserin ilaç salım sistemleriyle tedavisi, geleneksel ilaç uygulamalarına göre büyük avantajlar sağlamaktadır.

Bu çalışmanın amacı, meme kanseri tedavisi için optimize edilmiş özelliklere sahip reseptör hedefli karbon nanotüp bazlı nano-taşıyıcı geliştirmektir. Karbon nanotüplerin öne çıkan fiziksel, kimyasal, optik ve NIR floresan özellikleri nedeniyle, taşıyıcı olarak geniş çapta araştırılan malzemelerdir. Tasarlanan sistemin anahtar bölümünü oluşturmak için tek duvarlı karbon nanotüpler (TDKNT'ler) kullanılmıştır ve nano taşıyıcının geliştirilmesi için iki farklı tek duvarlı karbon nanotüp tercih edilmiştir. Nanotüplerin imal edilmesinden sonra, numunelerdeki safsızlıkları gidermek için SWNT'lere saflaştırma işlemi uygulanmıştır. Daha sonra, nano-taşıyıcılara biyouyumluluk özelliklerinin kazandırılması için, biyouyumlu bir polimer olan polietilen glikol (PEG) kullanılmıştır. Literatürde belirtildiği gib PEG'in hidrofilikliği sayesinde polimer nano taşıyıcılara gereken biyouyumluluk sağlanabilmektedir. İlk adımda, her bir TDKNT'yi kaplamak için zincir uzunlukları farklı olan 4 adet PEG (PEG_{2000}, PEG_{5000}, PEG_{12000} ve dallı PEG_{5000}) polimeri hazırlanmıştır. Bu çalışmadaki sentez işleminde başlangıç noktası metoksi PEG'dir. Bir sonraki adımda, PEG polimerleri PEG-COOH'ye dönüştürülmüştür ve TDKNT'lerin yüzey modifikasyonu için kovalent olmayan bir yaklaşım kullanılmıştır. piren taşıyan PEG elde etmek için, PEG-COOH ile piren metanol arasında bir esterifikasyon reaksiyonu gerçekleştirilmiştir. Son adımda ise, TDKNT'lerin fiziksel kaplamaları, söz konusu piren taşıyan PEG'ler kullanılarak başarıyla gerçekleştirilmiştir. Sentezlenen numuneleri karakterize etmek için ^{1}HNMR, FTIR, TGA, UV-vis ve floresan spektroskopisi analizi yapılmıştır. TGA analizinin sonucu, kısa TDKNT'lere PEG bağlanma miktarının, uzun TDKNT'lerden daha yüksek olduğunu göstermiştir. Üretilen nano-taşıyıcıların biyouyumluluğuna dair bilgi edinmek için, PEG ile kaplanmış TDKNT'ler için in vitro sitotoksisite ve in vivo kan dolaşım süresi analizleri yapılmıştır. PEG ile kaplanmış kısa ve uzun TDKNT'ler için yapılan in vitro sitotoksisite sonuçlarından, kısa TDKNT'lerdeki hücre canlılığının uzun TDKNT numunelerine göre daha yüksek olduğu anlaşılmıştır. PEG polimerinin moleküler ağırlığı azaldıkça, hücre çoğalmasının önlenmesi sonucunda hücre canlılığı azalmıştır. Ayrıca, konfokal floresan mikroskopi görüntüleriyle in vitro sitotoksisite sonuçları birbirini doğrulamıştır. Bir sonraki adımda, fareler üzerinde in vivo kan dolaşım süresi incelenmiştir. İlginç bir şekilde, dallanmış PEG_{5000} kaplı TDKNT'lerin kan dolaşımında 13 saate yakın kalarak daha uzun bir süre dolaşıma dahil olduğu görülmüştür.

Çalışmanın bir sonraki aşamasında, TDKNT'lere yüklemek için bir antikanser ajan olarak Doksorubisin (DOX) kullanılmıştır. Çalışmamızda DOX yükleme çalışmaları iki adımda gerçekleştirilmiştir. İlk adımda, kısa ve uzun TDKNT'ler, DOX yüklemesinin miktarını ve verimini araştırmak için 3 farklı pH'lı tampon çözeltilerinde hazırlanarak incelenmiştir. DOX yükleme ve salım miktarını araştırmak için UV-spektrometresi kullanılmıştır. DOX dalga boyunun karakteristik pikine dair net bir bilgi elde etmek için 350-650 nm arasında taram yapılmıştır. 490 nm'nin karakteristik pik olarak seçilip ileri çalışmalar için kullanılabileceği gözlenmiştir. Bundan sonra, TDKNT'ler için in vitro sitotoksisite araştırılmasıyla ile birlikte DOX-yüklü nanotaşıyıcıların ilaç salım performanslarının daha dikkatli bir incelemesi için, ilaç salım profillerinin matematiksel yaklaşımla incelemesi yapılmıştır.

Bir sonraki aşamada, nanotaşıyıcılara reseptör hedefli özellik kazandırmak için, Folik Asit (FA) ligand olarak kullanılmıştır. Piren-FA'nın TDKNT'lere eklenmesinden sonra, numunelerin PEGilasyonu gerçekleştirilmiş ve son olarak, nanotaşıyıcılara DOX ilacı yüklenmiştir. DOX'un farklı pH değerlerinde (5.5, 7.4 ve 9) kısa ve uzun TDKNT'lere yüklenmesi incelenerek, pH 9 da TDKNT'lere DOX yüklemesine daha yüksek olduğu gözlemlenmiştir. Nano taşıyıcıların salım performansı, normal ve kanser hücrelerinin içi ortamını taklit etmek için sırasıyla fizyolojik pH 7.4 ve asit pH 5.4'te incelenmiştri. Sonuçlar, tüm nanotaşıyıcıların pH 5.4'te daha yüksek salım miktarına sahip olduğunu göstermiştir. Ayrıca, FA kaplı TDKNT nanotaşıyıcıları, her iki pH'ta da daha yüksek salım performansı göstermiştir. Son aşamada, DOX yüklü TDKNT örnekleri için in vitro sitotoksisite gerçekleştirildi. FA kaplı TDKNT'lerin, FA kaplı olmayan TDKNT'lere göre daha düşük hücre canlılığına sahip olduğu gözlenmiştir.

Önceki bölümlerde, in vitro ve in vivo çalışmalarda hasarsız TDKNT'ler kullanılmıştır. Bununla birlikte, TDKNT üretimi ve saflaştırma aşaması boyunca, hasarsız TDKNT'lerin elde edilmesinin önlenemeyeceği düşünülmektedir. Bu çalışmanın devamında, hasarlı nanotüpler ve piren taşıyıcı yapılar arasındaki van der Waals etkileşimi üzerindeki etkisini araştırılmıştır. Buna göre, hasarlı TDKNT'lerde π-π etkileşiminin rolünü araştırmak için, TDKNT yan duvarlarına adsorbe etmek üzere tasarlanmış bir dizi hidroksil ve karboksil fonksiyonelleştirilmiş bileşik ile moleküler dinamik ve deneysel çalışmalar yapılmıştır. Topolojik Stone-Wales hasarlarının TDKNT'ler üzerindeki etkisinin, piren taşıyıcı bileşik yapılarının bağlanma miktarı üzerindeki etkisi araştırılmıştır. İlk aşamada, 3 farklı TDKNT (hasarsız, hasarlı ve –-COOH fonksiyoneleştirilmiş hasarlı karbon nanotüplerin moleküler dinamik çalışmalar yapılmıştır. Kaplama bileşikleri olarak piren-COOH, piren-$(OH)_2$ ve piren-OH kullanılmıştır. Bağlanma enerjisi ve Radyal Dağılım Fonksiyonu (RDF), piren-COOH'nin su molekülleri ile daha yüksek hidrojen bağı oluşturabildiğini, dolayısıyla TDKNT'leri sulu ortamda dağıtabildiklerini göstermiştir. Ayrıca, aromatik yapısında bozulma nedeniyle -COOH fonksiyonelleştirilmiş hasarlı TDKNT'leri, piren ile etkili bir π-π etkileşiminin sağlayamadığı gözlemlenmiştir. Bu nedenle, pirenin TDKNT'lerin yüzeyine bağlanması kararlı değildir. Son aşamada, piren-COOH, piren-$(OH)_2$ ve piren-OH bileşikleri sentezlenerek ve TDKNT'lerin fiziksel kaplanması için kullanılmıştır. Beklendiği gibi, piren-COOH kaplı TDKNT'ler, sentezlenmiş TDKNT nanotaşıyıcıları için daha yüksek dağılım sağlamıştır. Piren-COOH, piren-$(OH)_2$ ve piren-OH kaplı TDKNT'lerin dispersiyonu hakkında görsel bilgi edinmek için, TDKNT'lerin t = 0, 1,3,5 saat zaman aralıklarında su içindeki dispersiyonu fotoğraflandı. Sonuçlar, TDKNT'lerin 1 saat sonra su içinde başarıyla dağıldığını açıkça göstermiştir. Pyr-OH ve pyr-$(OH)_2$ ile kaplanmış TDKNT'lerin çökmesi zaman

ilerledikçe gerçekleştiği görülmğüştür. Pyr-OH ve pyr- $(OH)_2$ ve su molekülleri arasında düşük H-bağı oluşumu ve daha hidrofobik yapıları nedeniyle TDKNT'lerin daha düşük bir dispersiyouna sahip olduğu gözlemlenmiştir. Pyr-COOH ile kaplanmış SWNT'lerde ise, 5 saat sonra tamamen homojen bir şekilde dipsers olduğu saptanmıştır. Dispersiyon davranışındaki farkın, pyr-COOH içindeki karboksil grupları ve su arasındaki etkili H-bağı etkileşimlerin moleküler dinamik simülasyon sonuçları ile mükemmel uyum içinde olduğu görülmüştür

1. INTRODUCTION

Heart disease and cancer are the first and second leading causes of deaths in the world for more than a decade. However, the statistics from the American Cancer Society [1] show that cancer death rate has dropped progressively over the past 25 years in the United States. The decline in cancer mortality is attributed to the gradually drops in smoking and developments in early diagnostics and treatment.

Cancer refers to the rapid and abnormal cell growth in the body [2–4] . Unlike to normal cells, in cancerous tissues cells divides in an uncontrolled manner into malignant. These cancer cells are not restricted in fixed sites and may spread more rapidly leading to development of tumor. Breast cancer is the second most diagnosed cancer in women in the world [1], after skin cancer, affecting one in eight woman aged up to 80 years. The disease arises when breast cells mutate and reproduce uncontrollably and form tumor. Early diagnostics play crucial role in treatment of cancer [5]. Cancer cells have the capability to spread to all over the body and may develop other cancer types [3]. Women with a family history of the disease carry higher risk for breast cancer. The delivery of a therapeutic agent to the specific part of the body has always been a major challenge in diseases treatment. Weak biodistribution, lack of selectivity and limited efficacy are main disadvantages of conventional drugs application. At this point, controlled drug delivery systems offer great prospects to overcome these limitations. Controlled drug delivery systems have the following advantages [6–10] over the conventional drug application: 1) lower clearance from the circulatory system 2) delivery of the drug to the site of action 3) lower harmful side effects and 4) lower drug concentration required.

1.1 Nanoparticels

According to the National Nanotechnology Initiative (NNI) classification, nanoparticles size in the range of 1 and 100 nm can be assumed as one dimension. In order to characterize a nanoparticle as potential delivery tools, nanoparticles should have optimized physical, chemical and biological features (Figure 1.1). Moreover, the

size of the nanocarrier has to be in appropriate range to be taken up easily by targeted cell tissues [11].
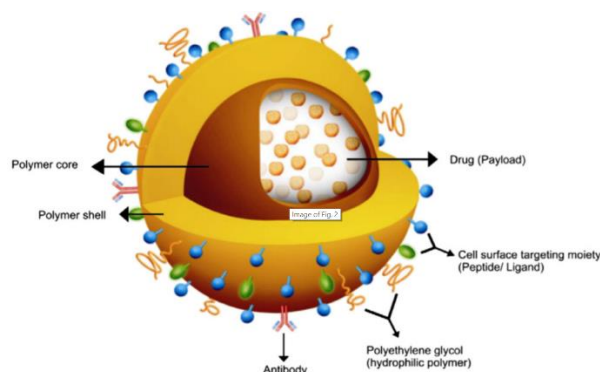
Figure 1.1 : A polymeric nanohybrid device vector [12].

Thus far, various nanocarriers were offered as drug delivery systems (Figure 1.2). The first nanocarrier that was used as drug carriers is liposomes. These spherical vesicles nanocarriers are in 80–300 nm size range [13] and mostly composed of phospholipids bilayers. It was shown that liposomal nanocarriers enhance the pharmacokinetic properties of the therapeutic agents by improving their solubility and biodistribution [14]. After the encapsulation of the drug in liposomal nanocarrier, the release can be triggered by changing the pH of the medium, its concentration, or osmotic gradient. Thus far, several therapeutic agents including anti-inflammatory [15], antibiotics [16], [17] neurotransmitters (serotonin) [18] and anticancer drugs [14] were successfully used to be delivered by liposomal formulation.

Polymeric nanoparticles are main class of nanocarriers that have been widely employed for drug delivery applications. PEGylated PLGA for DOX delivery [19], polyacrylate in delivery of β-lactam [20], PLA-co-PLG for antifungal drug Clotrimazole delivery [21] and poly(ethylene oxide-g-acrylamide) for delivery of anticancer prodrug of Capecitabine [22] are some examples of polymeric nanoparticles that were used for biomedical applications.

1.2 Carbon Nanotubes

Carbon nanotubes (CNT) are novel class of nanomaterials attracted tremendous attention due to their promising characteristics for biological settings [23–27]. CNTs with three dimensional hexagonal arrangements of carbon atoms which are considered one of the high stiff materials [28, 29] and characterized with excellent optical intensity

[30], thermal [28, 31, 32] and electrical [33][34] and strong Raman signals [35, 36] CNTs can be classified mainly into two types based on their diameter, length and number of walls as shown in Figure 1.3. Single walled carbon nanotubes (SWNTs) and multi walled carbon nanotubes (MWNTs) are two types of carbon nanotubes that are widely used in various application.
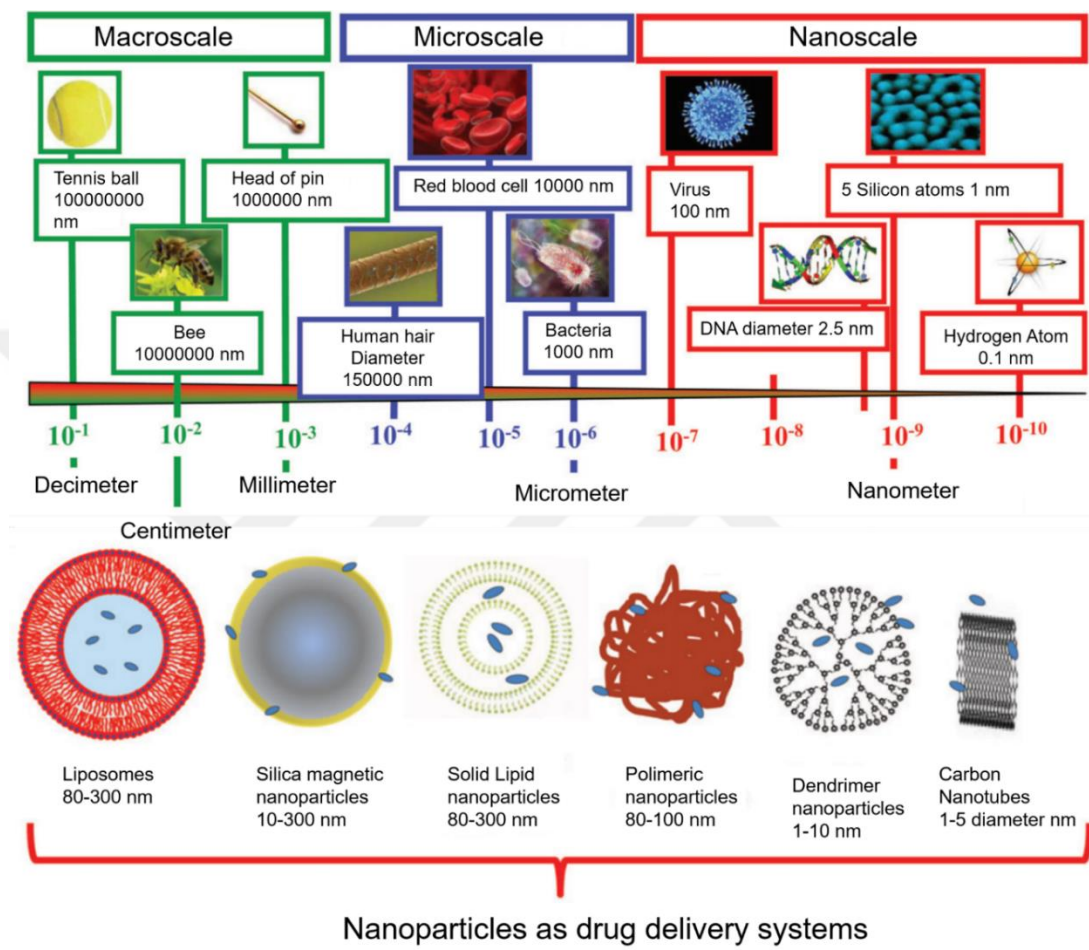
Figure 1.2 : Classification of particles based on their size [11].

Owing to their intrinsic physiochemical and Near Infrared (NIR) photoluminescence properties, these nanomaterials hold great application for drug delivery systems especially for cancer imaging and therapy. CNTs can be considered as nanocarrier as they contain the following properties [37] :1) Needle like structure 2) high aspect ratio 3) NIR fluorescence emission. However, these nanomaterials have some drawback just like any other nanomaterials. One of the disadvantages of these nanoparticles are the cytotoxicity in biological applications. In this regards, surface modification of these nanoparticles is required to be employed in drug delivery systems. Two different methods were offered to overcome this challenge. Covalent functionalization and

noncovalent coating of these nanomaterial are two approach that have used to improve their cytotoxic properties.
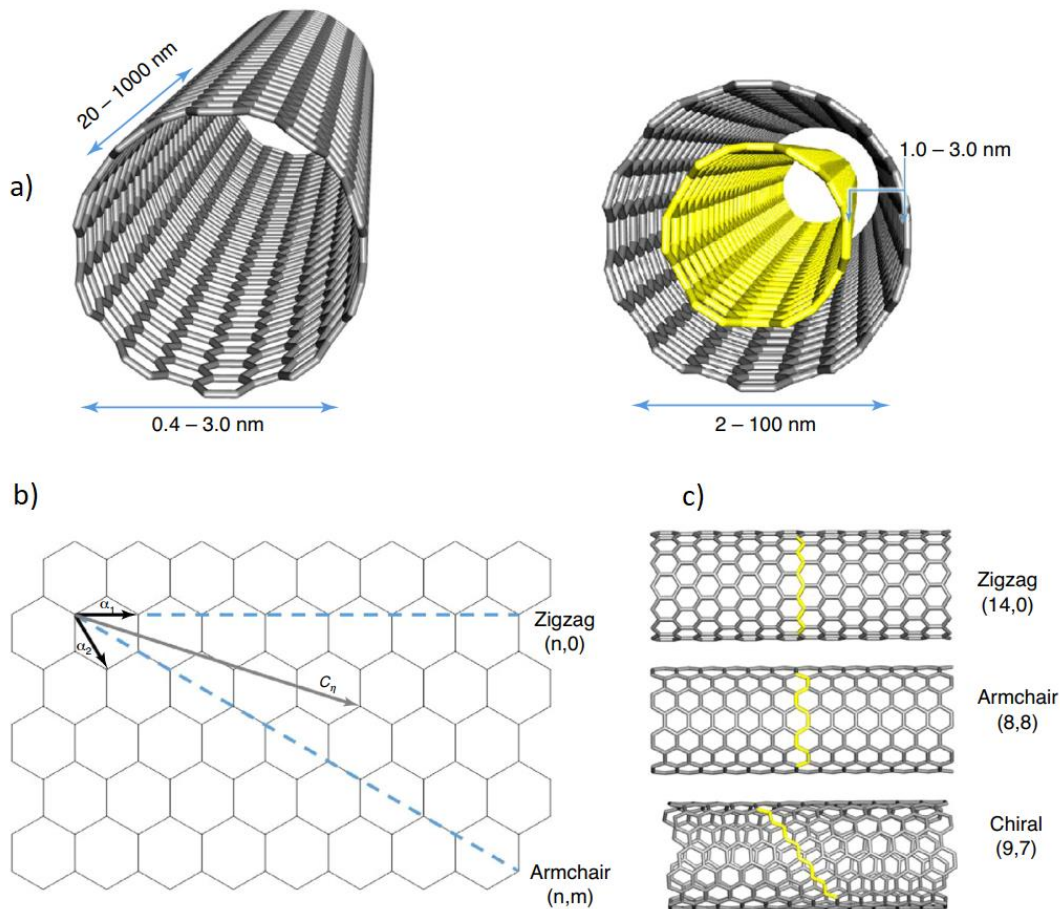
Figure 1.3 : Classification of CNTs: (a) Single wall carbon nanotubes (b) Multiwall carbon nanotubes [37].

Noncovalent surface modification of CNTs can be achieve by coating the surface of these nanomaterials by supramolecular structures such surfactants, DNA, RNA, biopolymers and proteins. Due to their sp^2 graphitic carbon atoms, these nanomaterials have hydrophobic structures. Therefore, they can easily provide van der Waals and π-π stacking interaction with similar structures.

Sodium dodecyl sulfate based materials [38, 39], DNA [40, 41], protein[42–44] and phospholipid−polyethylene glycol (PL−PEG) are some of the supramolecular structures that was used for surface modification of these nanomaterials [37].

Covalent functionalization is another approach that was employed by researchers for surface modification of CNTs. This method results in the introduction of heteroatoms (mostly O and N) to the side wall or end cap of nanotubes which leads to the disruption

of SP^2 hybridization of carbon atom. However, through these kind of atoms surface functionalization of CNT is achievable by conjugation of biocompatible structures.

1.3 Molecular Dynamics

Molecular dynamics (MD) is a computer simulation technique for understanding the atoms and molecules structure-to-function relationships. Over the last several decades MD has become an integral part of theoretical study for engineering, material sciences, biophysics, chemistry, and biology. In MD technique, the time evolution of many-body systems is assessed by numerically integrating Newton's equations of motion. Thanks to recent progress in high performance computing (HPC) machine, it is now possible to achieve time scales that compatible with biological processes.

In this part of the chapter in summary we present how molecular dynamics simulation was performed to light up the invisible microscopic details for the designed nanocarrier system. Moreover, it is discussed how MD concept and technique have been applied to make the main principle operational and therefore to predict experimental results.

1.3.1 Classical molecular dyanmics

In classical MD simulations for a system of N interacting particles, Newton's equations of motion are described by [45]:

$$\vec{f_i} = m_i \vec{a_i} \tag{1.1}$$

$$\vec{f_i} = -\frac{\partial}{\partial \vec{r_i}} \mu(r_i, r_j) \tag{1.2}$$

where m_i and $\vec{f_i}$ are the mass of particle i and the force acting on atom i due to the interactions with nearby atoms, respectively. $\vec{a_i}$ and μ denote the acceleration created by the force $\vec{f_i}$ and the potential energy between the atoms, respectively.

1.3.2 Force fields

In molecular modeling, a Force Fields (FF) is a mathematical expression describing the time evolution of bonding interaction consisting of bond lengths, bond angles and torsions and nonbonding interaction consisting of van der Waals and electrostatic interactions between atoms [46].

$$U(\vec{R}) = \sum_{bonds} k_i^{bond} (r_i - r_0)^2 + \sum_{angles} k_i^{angle} (\theta_i - \theta_0)^2$$

$$+ \sum_{dihedrals} k_i^{dihe} [1 + \cos(n_i \emptyset_i + \delta_i]$$

$$+ \sum_i \sum_{j \neq i} 4\epsilon_{ij} \left[\left(\frac{\sigma_{ij}}{r_{ij}}\right)^{12} - \left(\frac{\sigma_{ij}}{r_{ij}}\right)^6 \right] + \sum_i \sum_{j \neq i} \frac{q_i q_j}{\epsilon r_{ij}}$$

(1.3)

1.3.3 Statistical ensembles

In statistical mechanics, an ensemble is a probability distribution refers to an idealized tool, which is used for studying the evolution of a thermodynamic system. The ensemble involves a large number of virtual copies with a set of fixed and known thermodynamic variables (Table 1.1).

Table 1.1 : List of statistical ensemble used in molecular daynamics.

Symbol	Ensemble Name	Fixed Variables
Ω	Microcanonical	N, V, E
Q	Canonical	N,V,T
Δ	Isobaric-isothermal	N,P,T
Θ	Grand canonical	μ, V,T

1.3.3.1 Microcanonical

The microcanonical ensemble (NVE) refers to constant-energy, constant-volume system which can be defined by solving Newton's equation without any temperature and pressure control. This system is completely isolated from its surroundings.

1.3.3.2 Canonical ensemble

In statistical mechanics, a canonical ensemble is the statistical ensemble that represents the possible states of a mechanical system in thermal equilibrium with a heat bath at a fixed temperature. The system can exchange energy with the heat bath, so that the states of the system will differ in total energy.

In canonical ensemble (NVT), temperature, volume and number of particles of the system (a solid, liquid or a gas) are kept constant throughout the run. The ensemble is

6

obtained by being immersed in a heat bath at a temperature T and fixing the volume of the system.

1.3.3.3 Isothermal-Isobaric ensemble

This ensemble is typically abbreviated in terms of constant number of particles, pressure, and temperature (NPT). This ensemble enables us to have control over both the temperature and pressure.

1.3.3.4 Grand canonical

The grand canonical ensemble (μVT) can be described by constant-chemical potential, μ, constant-volume V and constant-temperature T variables. In μVT ensemble, the total particle number N is therefore allowed to fluctuate.

2. EXPERIMENTAL

2.1 Materials

Poly (ethylene glycol) monomethyl ether with 2000, 5000 and 12000 g/mol molecular weight were obtained from Sigma Aldrich and were used as received. Dichloromethane (CH_2Cl_2) was purchased from Aldrich and distilled over P_2O_5 before usage. Tetrahydrofuran (THF; 99.8%, J.T. Baker) was dried and distilled over benzophenone–Na. Other solvents were purified using standard procedures. Succinic anhydride, dimethylaminopyridine (DMAP), trimethylamine (TEA), N, N'-dicyclohexylcarbodiimide (DCC), Folic acid (FA), 1-pyrenemethanol 98% and 1-pyreneacetic acid were all purchased from Aldrich and used as received without further purification. Human Umbilical Vein Endothelial cells (HUVEC) were obtained from American Type Culture Collection (Manassas, Va.). Nitric acid (78%) and phosphate-buffered saline powder were purchased from Sigma-Aldrich.

Short and long SWNTs and doxorubicin (DOX) were kindly provided by Prof. Dr. Nilgün Yavuz from Energy Institute of Istanbul Technical University and Dr. Ayhan Ünlü from Trakya University, respectively.

2.2 Synthesis Methods

2.2.1 Preparation of PEG –COOH

Succinic anhydride (1.46 g, 14.6 mmol) and dimethylaminopyridine (DMAP) (209 mg, 1.71 mmol) were completely dissolved in 15 mL of anhydrous THF and kept at 0 °C for 30 min. PEG_{2000} (4.28 g, 4.28 mmol) and trimethylamine (TEA) (1.8 mL, 12.8 mmol) were mixed in 15 mL of THF and transferred slowly into the succinic anhydride solution using a syringe. The solution was stirred at 0 °C for 2 h, and the reaction was continued at room temperature for 24 h under the nitrogen atmosphere. Then $PEG_{2000}COOH$ was precipitated in cold diethyl ether. The precipitates were dissolved in dichloromethane again and then reprecipitated in cold diethyl ether. The precipitates were dried under vacuum at room temperature overnight. The same procedure was applied to synthesize $PEG_{5000}COOH$ and $PEG_{12000}COOH$.

2.2.2 Preparation of pyrene bearing polymers (pyr-PEG)

A relatively straightforward method was used to synthesize poly (ethylene glycol) monomethyl ether pyrene. Firstly, 1-pyrenylmethanol (1.0 g,4.3 mmol), $PEG_{2000}COOH$ (3.5 g, 1.1 mmol), and 25 mL of dry THF were added to an around-bottomed flask. Then, to the reaction mixture, dicyclohexylcarbodiimide (1.33 g, 9.47 mmol) and dimethylaminopyridine (DMAP) (0.21 g, 1.71 mmol) in 15 mL of dry THF was added dropwise over a period of 30 min at 0 $^{\circ}$C under nitrogen and then stirred at room temperature overnight. At the end of reaction time, the reaction solution was concentrated and the crude product was dissolved in diethyl ether, washed with dilute $NaHCO_3$ aqueous solution for two times, and dried over anhydrous Na_2SO_4.

2.2.3 Functionalization of SWNTs with pyrene-PEG

50 mg SWNTs, 0.25 g pyrene-PEG_{2000} (polymer to nanotubes ratio: 5, w/w), and 150 mL of dry THF were added to a round-bottomed flask. The obtained mixture was sonicated for 30 min, in a low-power sonic bath and stirred vigorously for additional 72 h at room temperature. The mixture was filtered through a filter (Sartorius, PTFE; pore size, 0.2 μm) to remove nonattached pyrene-PEG (pyr-PEG). Then remaining solid on the filter was sonicated well with using an excessive amount of fresh THF and filtered again. This procedure repeated until the free filtrate was obtained. The achieved black powder was then dried under vacuum at 35 $^{\circ}$C for 24 h. The same procedure was applied to obtain pyrene-PEG_{5000} and pyrene-PEG_{12000}.

2.2.4 Preparation of branched PEG$_{5000}$(pyr-PEG$_{b5000}$)

(6,10-dihydropyren-1-yl)methyl 2,2,5-trimethyl-1,3-dioxane-5-carboxylate (pyrene ketal) (0.5 g, 1.4 mmol), PEG_{5000}-COOH (2.73 g, 4.2 mmol) and DMAP (0.17 g, 1.4 mmol) was dissolved in 100 mL of CH_2Cl_2 were added to the reaction mixture in that order. After stirring 5 minutes at room temperature, DCC (0.87 g, 4.2 mmol) dissolved in 50 mL of CH_2Cl_2 was added. Reaction mixture was stirred two days at room temperature and ammonium salt by-product was filtered. The product was purified by column chromatography over silica gel eluting with ethyl CH_2Cl_2/acetate (1:1) to get the unreacted materials then CH_2Cl_2/methanol(1:1) to obtain pyr-PEG_{5000}-PEG_{5000}. Then the polymer was precipitated in diethyl ether.

2.2.5 Synthesis of 4-oxo-4-(pyren-1-ylmethoxy)butanoic acid (pyr-COOH)

First, pyrene methanol (2.0 g, 8.61 mmol) was dissolved in 100 mL of CH_2Cl_2. To the reaction mixture, Et_3N (6 ml, 43.1 mmol), DMAP (1.05 g, 8.61 mmol) and succinic anhydride (2.58 g, 25.8 mmol) were added in the given order. The mixture was stirred for overnight at room temperature. Then, the reaction solution was discharged into ice-cold water (150 mL), stirred for 30 min at room temperature before pouring into separating funnel. The organic phase was extracted with 1M HCl (100 mL). The aqueous phase extracted with CH_2Cl_2 and combined organic phases dried over Na_2SO_4 and concentrated.

2.2.6 Synthesis of (6,10-dihydropyren-1-yl)methyl 3-hydroxy-2 (hydroxymethyl)-2-methylpropanoate (pyr-Diol)

In order to obtian pyren-$(OH)_2$ (pyr-Diol), acid ketal (3.0 g, 7.7 mmol) was dissolved in a mixture of 100 mL of THF and 60 mL of 1 M HCl. The reaction mixture was stirred for 2 h at room temperature. Afterward, the reaction solvent was evaporated and product was extracted with 320 mL of CH_2Cl_2 and 80 mL of water. The combined organic phase was dried with Na_2SO_4 and concentrated.

2.2.7 Synthesis of pyrene bearing folic acid (pyr-FA)

Typically, 1.5 mg of the 1-pyreneacetic-acid was added to a 50-mL round-bottom flask containing 0.2 g of folic acid (Aldrich, N97%) and 25 mL of N,N dimethylformamide (DMF; Aldrich, 99.8%). The mixture was refluxed overnight. After refluxing, pyr-FA was filtered using a 0.45-μm PTFE membrane (Membrane Solutions). Finally, pyr-FA was redispersed in water, filtered, and washed with deionized water.

2.2.8 Functionalization of SWNTs with pyrene bearing folic acid

50 mg SWNTs, 0.15 g pyr-FA and 150 mL of dry THF were added to a round-bottomed flask. The obtained mixture was sonicated for 30 min, in a low-power sonic bath and stirred vigorously for additional 48 h at room temperature. The mixture was filtered through a filter (Sartorius, PTFE; pore size, 0.2 μm) to remove nonattached pyr-FA. Then, the remaining solid on the filter was sonicated well with using an excessive amount of fresh THF and filtered again. This procedure repeated until the free filtrate was obtained. The achieved black powder was then dried under vacuum at 35 °C for 24 h.

2.2.9 Functionalization of SWNTs with pyr-FA and pyr-PEG

50 mg SWNTs/pyr-FA, 0.25 g pyr-PEG$_{b5000}$ and 150 mL of dry THF were added to a round-bottomed flask. After sonication for 30 min in a sonic bath the mixture was stirred vigorously for additional 72 h at room temperature. Finally, the mixture was filtered through a filter (Sartorius, PTFE; pore size, 0.2 μm) to remove nonattached pyr-PEG$_{b5000}$. Then, the remaining solid on the filter was sonicated well with using an excessive amount of fresh THF and filtered again. This procedure repeated until the free filtrate was obtained. The achieved black powder was then dried under vacuum at 35 °C for 24 h. The same procedure was applied to obtain pyr-PEG$_{12000}$ coated SWNTs/pyr-FA nanostructure.

2.2.10 Doxorubicin (DOX) loading onto SWNTs

DOX hydrochloride (1.5 mM) was stirred with short and long SWNTs nanocarriers (0.1 mg/ml) in different buffer solutions (pH=5.5, 7,4 and 9) for 20 h at room temperature. The product was collected by separation and washed several times with buffer until the supernatant became color free. UV–vis absorbance spectra of DOX-loaded samples were measured by using Perkin Elmer LS 45 spectrometer. The concentration of DOX loaded SWNTs nanocarriers was measured at the characteristic value of DOX which is 490 nm. To achieve DOX loaded PEGylated SWNTs, noncovalent binding method was used. Different PEGylated SWNT samples were separately dissolved in buffer solution at pH 9 and sonicated for 30 min to achieve a satisfactory SWNT dispersion. Then, SWNT solution was simply stirred with DOX for 20 h at room temperature in the dark. To remove any free and unbound DOX in solution repeated fltering were carried out. The formation of different PEGylated SWNT/DOX complex was verifed by the reddish color of the solution.

2.2.11 Doxorubicine release studies

In order to explore the release performance of DOX from different SWNT samples two different pH values were used (pH 7.4 and 5.5). DOX loaded SWNT (1 mg) sample was dissolved in 5 ml buffer solution at 37 °C in pH 7.4 and pH 5.5. At different time intervals, 0.8 ml of the solution was withdrawn and the concentration was detected by Perkin Elmer LS 45 spectrometer at 490 nm. The releasing measurement of SWNT samples were repeated in triplicate. After UV-vis record, the outer SWNT solution were instantaneously returned back to the releasing medium. The release

measurement of all samples were pursued until the DOX releasing profile turned to flat.

2.3 Materials Characterization

Thermal gravimetric analysis (TGAs) were performed on Perkin–Elmer Diamond TA/TGA in the temperature range of 30–800 ºC, with a heating rate of 10 ºC /min under nitrogen. UV–vis spectra were recorded on an Agilent Cary 100 spectrophotometer in CH_2Cl_2. High-resolution transmission electron microscopy (HR-TEM) micrographs were collected using a JEOL 2100 instrument operating at 200 kV. HR-TEM samples were prepared by drop coating a dilute solution of the sample (in THF) on a holey carbon-coated copper grid. The 1H spectra were recorded in $CDCl_3$ with $Si(CH_4)_3$ as internal standard on an Agilent VNMRS 500 instrument (500 MHz for 1H). The FTIR spectra for poly (ethylene glycol) monomethyl ether, PEG−COOH, and pyrene-PEG were recorded by FTIR spectrometer [Spectrum RX I (Perkin-Elmer, Waltham, MA)] by using both ATR system (powder form directly usable). Raman spectra was recorded using a Raman Microscopy System (U.K.) with excitation at 514 nm and 10× objective, 10% laser power.

2.3.1 Fluorescence microscope images

MDA-MB-231 cells were cultured and after 48 h incubation, cells were trypsinized and reseeded into 9.5 cm^2 6-well coverslips containing culture plate of Nest that there were 500,000 cells in every plate. After 24 h incubation the DOX loaded long and short CNTs applied to the cells at concentrations 0, 10, 100 µg/ml, 2 wells for each. After 24 h waiting, cell culture media was removed from each well and washed twice with PBS. After washing and removing PBS, we added 1% Triton x-100 and % 99 PBS solutions to each well and waited 20 min at room temperature. The cells again washed twice with PBS and 1 ml of %2 paraformaldehyde and % 98 PBS solution was added to each well and incubated 1 h at + 4 °C. The cells washed twice with PBS last time and 1 ml of 1/1000 actin phalloidin TRICH and BSA–PBS solution was added to each well in the darkness and incubated at 37 °C, 30 min. Coverslips were carefully removed from the wells and blotted to remove any excess water. One drop of Prolong Dapi antifade was dispensed onto the microscope slide per coverslip. The coverslips

were mounted with the cells facing towards the microscope slide and visualized using Olympus BX51 fluorescence microscope.

2.3.2 Laser scanning confocal microscopy (LSCM)

HUVECs were seeded on round coverslip with 106 cells in each well. The day after, cells were incubated with pyr-PEG coated SWNTs for 6 h. Cells were washed with PBS and incubated for 30 min for increasing the membrane permeability with 0.1% Triton X-100-PBS. This was followed by 3 washes with PBS, which was repeated at the end of each step. Paraformaldehyde-PBS (2%) was used for the fixation for 1 hour at 4 °C, and then Phalloidin-TRITC (1:1000, Sigma) was used to determine the intracellular actin distribution. For labelling the nuclei, 4', 6-diamidino-2-phenylindole (DAPI, Invitrogen) was implemented and the preparations were imaged with a confocal laser scanning microscope (Leica, TCS-SPE) equipped with lasers providing 532 nm and 405 nm laser lines by Leica Application Suit Advanced Flourescence 3.3 (LAS AF) software [47].

2.4 Cell Culture and Cell Viability Assay

Human Umbilical Vein Endothelial Cells (HUVECs) were cultured in Dulbecco's Modified Eagle Medium F-12 (DMEM/F12, Gibco, UK) supplemented with 10% fetal bovine serum and 100 U/ml penicillin and 100 µg/ml streptomycin at 37 °C. Cells were seeded into 6-well plate (106 cells/well) and were incubated for 48 h prior to treatment with increased concentrations (5, 10, 50, 100 µg/ml) of pyr-PEG coated SWNTs. Cytotoxic effect of pyr-PEG coated SWNTs was tested with two different assays; 3-(4,5-dimethylthiazol-2-yl)-2,5-diphenyltetrazolium bromide (MTT, Sigma, USA) and water-soluble tetrazolium salt (WST-1, Sigma, USA). After incubation of HUVECs with pyr-PEG coated SWNTs for 48 h, MTT (final concentration 0.1 mg/ml) was added and incubated for 4 h at 37 °C. Following the decantation of supernatants, DMSO was added and incubated at room temperature in the dark for 30 min. Absorbance was measured at 570 nm with a plate reader (Biotek, USA). WST-1 cell proliferation/viability assay was realized according to the manufacturer's instructions.

2.5 In Vivo Blood Circulation Time Assay

To investigate in vivo blood circulation time for the PEGylated SWNTs, eight-week-old BALB/c mice were used. 4 mice were used for each SWNT sample. Each sample in saline solution was intravenously injected into the tail vein. At different time intervals, ~ 2 µl blood sample were collected and the same amount of lysis buffer added to the blood samples. The lysis buffer consists of buffer 40 mM Tris acetate, 1% Triton X-100, 1% SDS, 10 mM DTT and 10 mM EDTA. Raman spectroscopy was employed to measure the amount of SWNTs in the circulatory system of the mice using the density of the G bands. To achieve this, PEGylated SWNT solutions with known concentrations of 0.01 to 5 mg / ml were prepared and the density of the G bands were recorded at 808 nm to plot the calibration curve.

2.6 Statistical Analysis

All experimental studies were performed at least three times and each concentration was assayed in triplicate, to achieve independent experiments for the viability assays. Results were expressed as mean ± standard deviation (SD). Statistical analysis was carried out using one-way analysis of variance (ANOVA), followed by Student's t-test by GraphPad Prism 6.01. Differences were considered significant from $p \leq 0.05$ and $p \leq 0.01$.

2.7 Computational Methods

In the first step, one SWNTs was modeled to reveal the effect of functional groups on the interactions between pyr-COOH, pyr-$(OH)_2$ and pyr-OH and SWNT. We used the *Build* module of Materials Studio to generate a SWNT having (6,6) chirality with a diameter of 8.0 Å and a length of 22.0 Å. Model SWNT dimensions agree with the synthesized nanotubes. Using the same module, we built pyrene bearing pyr-COOH, pyr-$(OH)_2$ and pyr-OH molecules. Generated structures were subjected to the energy minimization satisfying an energy threshold of 0.001 kcal/mol using a combination of steepest descent, Newton-Raphson and quasi-Newton methods.

Using the *Adsorption Annealling* module for each system 7 pyrene bearing molecules and one SWNT were randomly packed together to the simulation box of a aqueous medium, fixing the density to 1.2 g/cm^3. Water was selected as solvent in order to

mimic both the polar solvent in the coating experiments and the hydrophilic property of body fluids. Simulation boxes were large enough to accommodate the SWNT and 7 pyrene bearing molecules. After energy minimization of the simulation cell MD simulations were performed with the *Forcite* module using the COMPASS force field for molecular interactions. Periodic boundary conditions were employed for the NVT ensemble at 300 K that was maintained by applying Berendsen thermostat with a decay constant of 0.1 ps. Electrostatic interactions were computed using the Ewald summation technique. For the long-range van der Waals interactions, the cutoff distance was taken as 12.5 Å. Each system was run for 5 ns, which was sufficient to monitor the rapid coating process of SWNTs with pyrene bearing molecules. Each simulation was replicated at least three times leading to a total 15 ns of simulation time.

3. RESULTS AND DISCUSSION

Owing to their intrinsic chemical, physical and biological properties, Single-walled carbon nanotubes (SWNTs) have been on spotlight as one of the most promising nanomaterials for biomedical applications such as cellular imaging [48, 49] bone scaffolding [50] MRI contrast agents [51] tumor destruction agents [52, 53] and intracellular protein transporters [23]. Although, pristine SWNTs have been reported to have the capability to transport their cargo without metabolism in the circulatory system and directly enter into the intracellular medium [24, 35, 54, 55] several studies revealed that carbon nanotubes have cytotoxic effects on cultured cells and adverse health outcomes on animals. Inhibition of cell proliferation [56, 57], induction of oxidative stress [25, 58] and apoptosis/necrosis are some of the negative impacts of SWNTs. The challenging task of employing of pristine SWNTs is their limited solubility in any biological environment due to their hydrophobic structure, which is prone to form bundles. Covalent modification or noncovalent attachment of biocompatible macromolecules to SWNTs are two common approaches, which trigger off the required dispersion into the biological media. Compared to the covalent functionalization, the noncovalent attachment is preferred to retain the desired properties of SWNT for cellular media, especially for NIR-II fluorescence imaging applications. Moreover, SWNTs wrapped by polymers, DNA or proteins prevent the disruption of the π-network of pristine carbon nanotubes.

Poly(ethylene glycol) (PEG) is a FDA approved polymer and one of the most effective polymers for surface coating of SWNTs [59]. Due to the hydrophilic, flexible nature and surface passivation of SWNTs, PEG chains provide the required resistance against immune system macrophages, which results in PEG-modified SWNTs to be recognized as biomaterials followed by prolonged blood circulation time and delayed clearance from the body[60]. Several strategies have been developed to synthesize PEG-coated SWNTs [49, 50, 61]. One of the versatile synthesis methods is the adsorption of aromatic moieties functionalized with PEG chains onto pristine SWNTs. Pyrene is an example of an aromatic compound made of four benzene rings fused

together. Pyrene conjugated PEG chains can strongly bind to SWNTs surface via $\pi-\pi$ interactions leaving the PEG chains extruding out from the sidewall [62, 63]. Here, the SWNTs size and the degree of PEGylation of SWNTs play crucial roles in affording the required biodistribution to the fabricated nanoplatforms for potential clinical applications. However, thus far there have been a few studies investigating these paramaters from this aspect. PEG chains with at least 2 kDa molecular weight can provide sufficient biodistribution and protection against immune system macrophages [64, 65]. The Dai group explored the uptake of SWNTs noncovalently functionalized by PEGylated phospholipids in the reticuloendothelial system (RES) of mice [66]. They observed that PEG chains with branched structures (7 kDa) had the desired blood circulation behavior and biodistribution excellent for in vivo applications. Low solubility of SWNTs in the biological environment is another issue that is strongly a size-dependent characteristic. As the size of SWNTs increase, due to strong van der Waals attractions between them, SWNTs tend to aggregate and form bundle structures leading to highly cytotoxic activity against cell lines and animal species [67, 68]. In this part of the study, the effect of PEG chain length (PEG_{2000}, PEG_{5000}, PEG_{12000} and branched PEG_{5000}) and SWNT size on cell viability of Human Umbilical Vein Endothelial Cells (HUVEC) along with in vivo blood circulaton time on mice were investigated.

3.1 SWNT Characterization

TEM images of the fabricated SWNTs are shown in Figure 3.1 TEM, is significantly the highest-resolution technique that enables to capture fine detail of carbon nanotube samples.
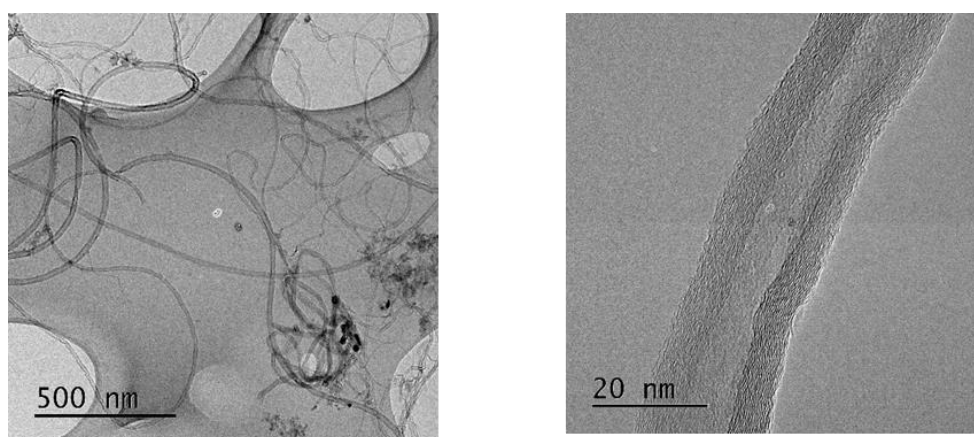
Figure 3.1 : TEM images of SWNTs synthesized at 800 °C.

It is evident that the structures synthesized by chemical vapor deposition method are carbon nanotubes. Raman spectroscopy is a powerful technique for the characterization of the structure of carbon nanotubes. Figure 3.2 shows Raman spectra for synthesized carbon nanotubes deposit excited by 532 nm laser. Two different spectra of CNTs were observed at the G band (around 1580 cm^{-1}) and D band (around 1350 cm^{-1}). It can be seen that the intensity of the G band is considerably higher than the D band. The intensity ratio of D to G band (ID/IG) expresses the quality of SWNTs. The higher ratio explains the higher amorphous carbon content and defect formation. The intensity ratio of G to D band of the synthesized SWNT sample was found as 0.69. This observation leads to a conclusion: SWNTs have low amorphous carbon content and defects. As seen in Figure 3.2, the spectrum in the RBM band, which is a characteristic of SWNT, was observed in the sample. The reason for this spectrum is that the tube diameter is below 2 nm and this result is consistent with other studies found in the literature [69]. If nanotube diameter is greater than 2 nm, RBM spectrum becomes difficult to be observed.
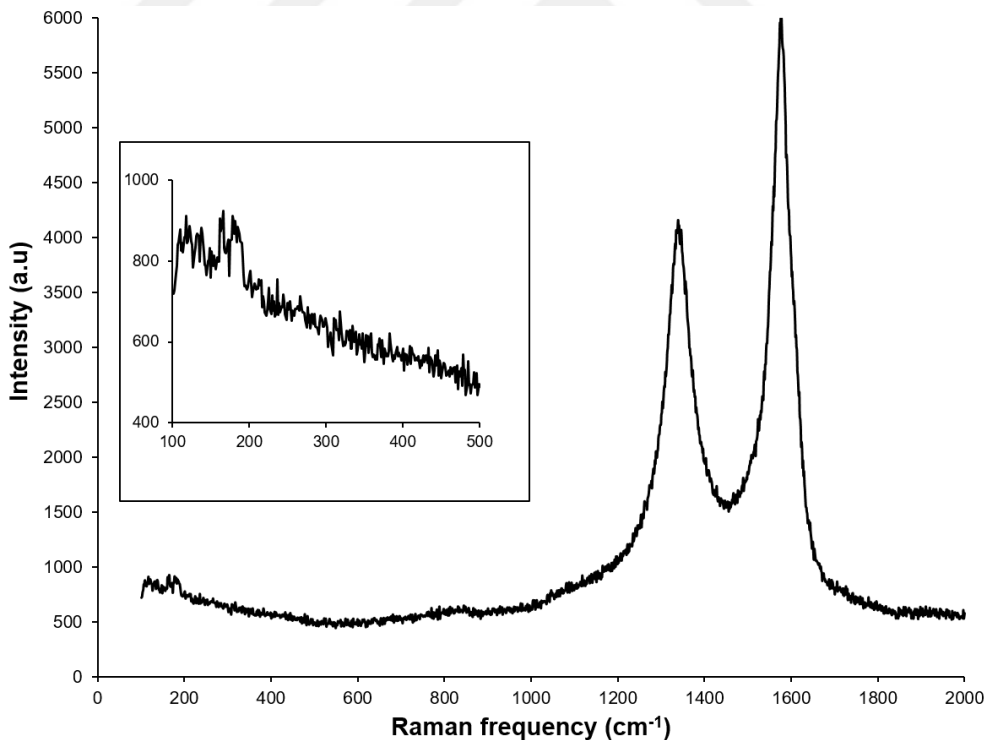
Figure 3.2 : Raman spectra of SWNTs synthesized at 800 °C.

RBM band has a property that can be used to calculate the mean diameter of SWNTs by the equation (3.1);

$$\omega(cm^{-1}) = A/d(nm) + B(cm^{-1}) \tag{3.1}$$

where; A and B are constants (A= 223 cm^{-1}.nm^{-1}, B=10 cm^{-1}) and d is the diameter of SWNT. The calculated mean diameter of the synthesized SWNT sample was found as approximately 1.4 nm.

3.2 Synthesis and Characterization of PEG-coated SWNT

The synthetic routes used for the preparation of pyr-PEG functionalized short SWNT (sSWNT) and long SWNT (lSWNT) is illustrated in Figure 3.3. Poly (ethylene glycol) monomethyl ethers with molecular weights of 2000, 5000, 12000 and branched PEG$_{5000}$ designated as PEG$_{2000}$, PEG$_{5000}$, PEG$_{12000}$ and PEGb$_{5000}$ were selected to synthesize pyr-PEGs. As shown in Scheme 1, hydroxyl end group of the PEG$_{2000}$, PEG$_{5000}$, PEG$_{12000}$ and PEGb$_{5000}$ were first transformed into the carboxylic acid group via reaction of PEG with succinic anhydride. The reactions for all PEG-COOH was carried out under mild conditions at room temperature through the catalysis of TEA and DMAP.
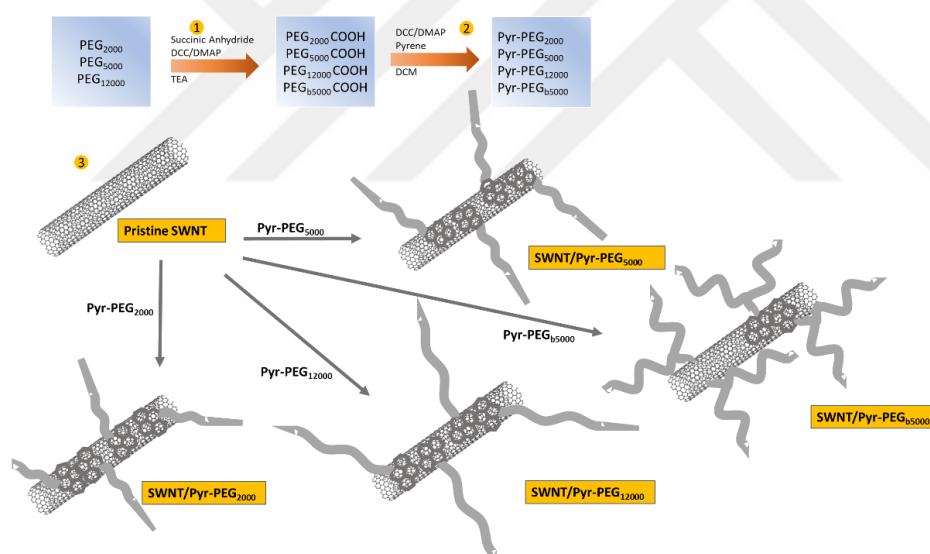
Figure 3.3 : Schematic illustration of the reactions involved in the preparation of the PEGylated SWNT.

To investigate the effect of PEG chain length, along with PEG$_{2000}$, PEG$_{5000}$, and PEG$_{12000}$ branched PEG$_{5000}$ was also synthesized. The synthesis protocol was given in previous chapter in detail. FTIR along with ^{1}HNMR analysis were used to investigate the conversion of the hydroxyl group of methoxy PEG to PEG-COOH. Figure 3.4 shows the characteristic FTIR spectra of PEG$_{5000}$ and PEG$_{5000}$COOH. According to FTIR analysis, methoxy PEG exhibited its characteristic peak at 2882 cm^{-1} due to –O CH$_2$CH$_2$ units of PEG backbone [69].
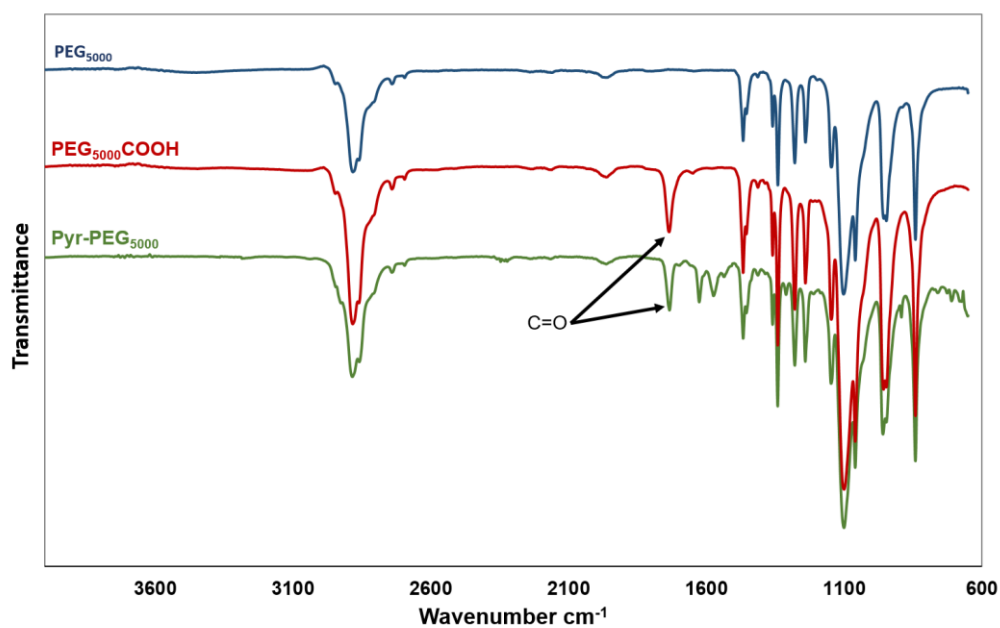
Figure 3.4 : Schematic FTIR characterization of PEG$_{5000}$ and PEG$_{5000}$COOH.

The characteristic peaks for carboxyl group of the PEG$_{5000}$COOH appeared at 1734 cm^{-1} confirming the transform of hydroxyl to the carboxyl groups.
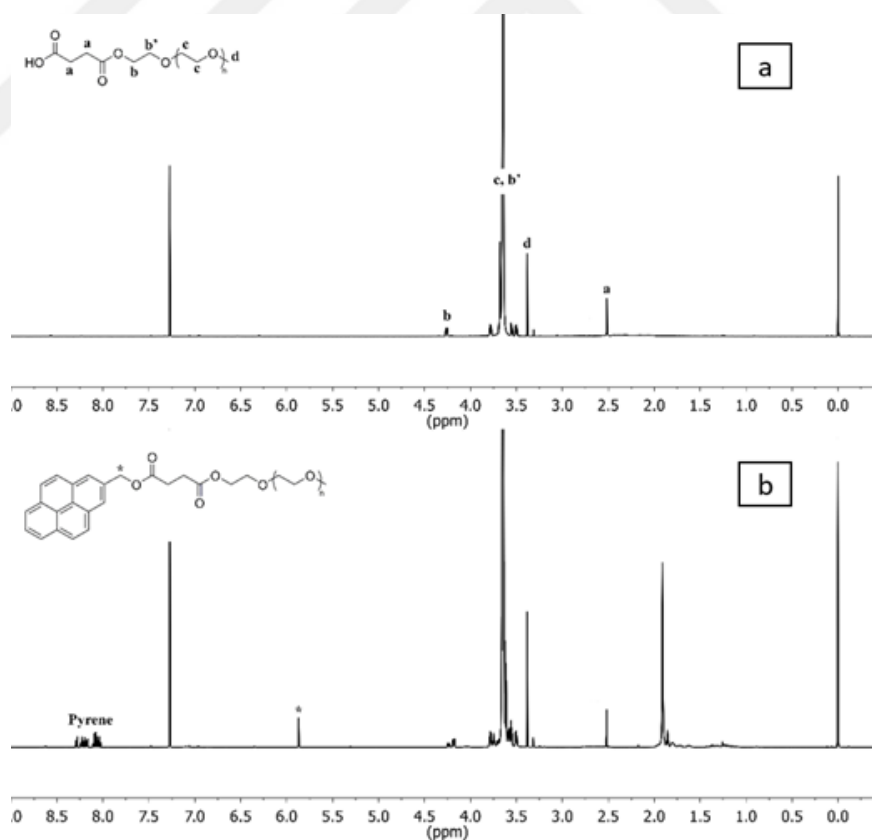
Figure 3.5 : ^{1}HNM characterization of (a) PEG$_{5000}$COOH, (b) pyr-PEG$_{5000}$.

Figure 3.5a shows the ^{1}HNMR characteristic peaks of CH$_2$ group (δ = 2.5 ppm) of succinic anhydride, which proved the formation of PEG$_{5000}$COOH. The formation of pyr-PEG was confirmed by the FTIR and ^{1}HNMR measurements. As shown in Figure 3.4, the FTIR characteristic peaks of aromatic double bond for pyr-PEG was obtained at 1574 cm^{-1} and 1625 cm^{-1}[70, 71].
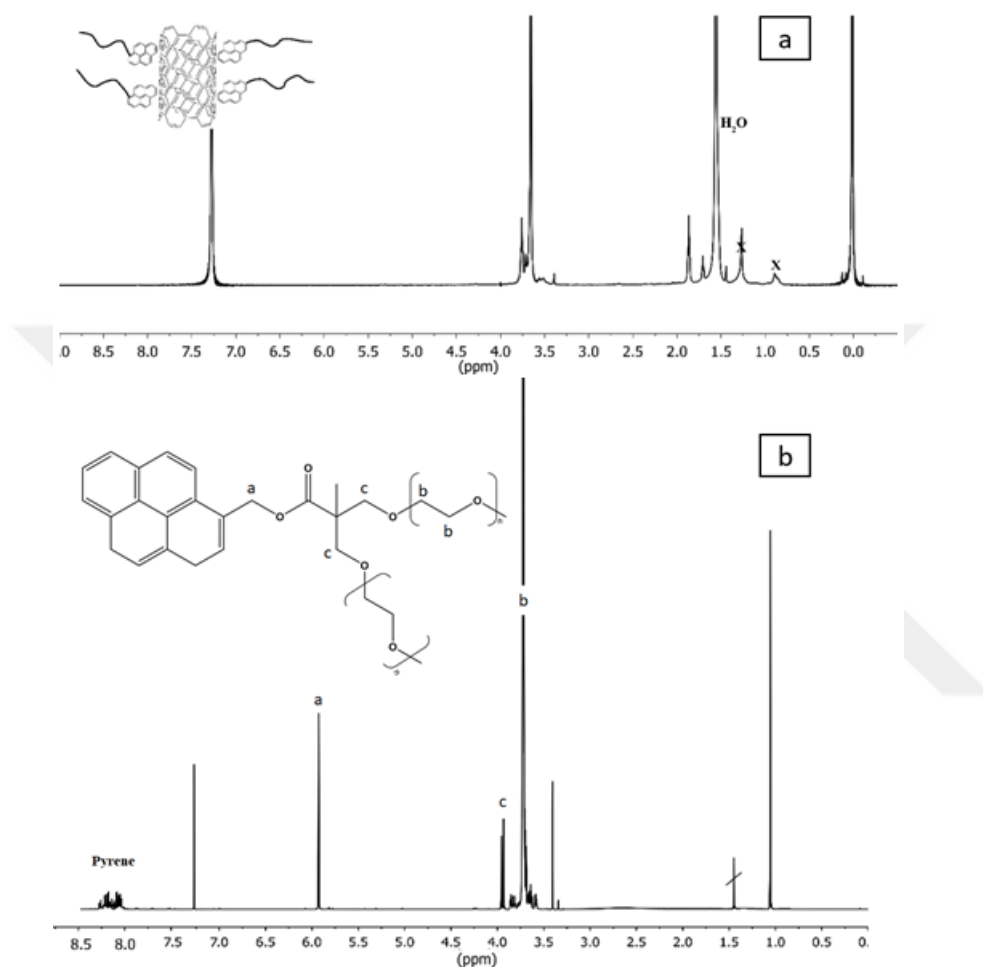
Figure 3.6 : [1]HNM characterization of (a) pyr-PEG functionalized SWNT (b) pyr-PEGb$_{5000}$.

The formation of pyr-PEG via esterification reaction was also corroborated by ^{1}HNMR. As it can be seen from Figure 3.5 and Figure 3.6, all expected signals attributed to the pyrene (δ = 8–8.2 ppm, ArH) and PEG (δ = 3.62 ppm, OCH$_2$CH$_2$O) segments can be seen for the synthesized pyr-PEG$_{5000}$. While pyr-PEG was introduced to SWNTs, the ^{1}HNMR characteristic peaks of pyrene (δ = 8–8.2 ppm, ArH) was disappeared due to the formation of $\pi-\pi$ stacking interactions between the pyrene bearing PEG molecules and SWNTs. ^{1}HNMR analysis for the branched PEG$_{5000}$ are illustrated in Figure 3.6. The related characteristic peaks for branched PEG$_{5000}$ and pyrene anchor are appeared in different ppm values as represented in the 3.6b. In the

final step of SWNTs PEGylation, the synthesized pyr-PEG was noncovalently (π−π stacking) linked to SWNTs. The anchor molecule pyrene can attach irreversibly onto the graphitic surface of SWNTs due to van der Waals interactions [72]. This binding characteristic between pyrene molecule and SWNTs was used by Dekker and coworkers [73] to study the effect of the enzyme on the electrical conductance of SWNT.

The noncovalent functionalization of SWNTs based on a pyrene moiety were also studied by Robert et al. [62] in the fabrication of protein immobilized SWNTs by using a bifunctional molecule 1-pyrenebutanoic acid, succinimidyl ester. They observed that the pyrenyl group irreversibly bound onto the sidewalls of SWNTs in an organic solvent. A similar modification strategy involves the attachment of pyrene-modified miktoarm star polymer to the sidewalls of the nanotubes was reported by Hakan et al [74]. In this case, the group introduced the amphiphilic miktoarm star polymer, polystyrene-poly(ethylene glycol)-poly(methyl methacrylate), bearing a pyrene group at the end of polystyrene arm (Pyrene-PS-PEG-PMMA) onto the multi-walled carbon nanotubes (MWNT) by noncovalent binding.

Fluorescence spectra of pyr-PEG$_{5000}$ and sSWNT_Pyr-PEG$_{5000}$ at 375 nm excitation wavelength are shown in Figure 3.7.
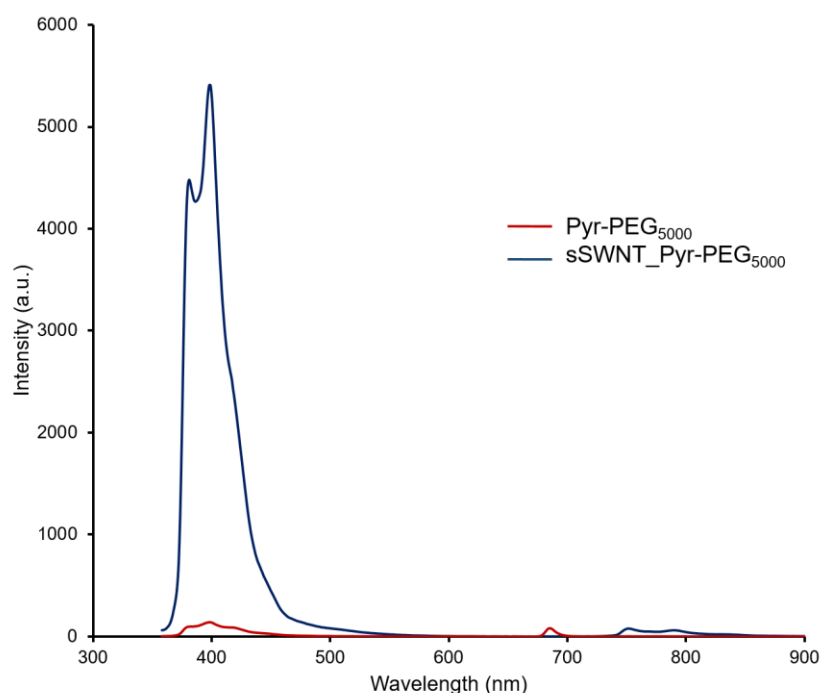
Figure 3.7 : Fluorescence emission spectra of pyr-PEG$_{5000}$ and sSWNT_ pyr-PEG$_{5000}$.

The pyr-PEG$_{5000}$ displayed the characteristic fluorescence peak of pyrene unit, however, after the incorporation of Pyr-PEG$_{5000}$ to SWNTs, this characteristic peak was completely quenched. This result is consistent with the literature [62] and verifies that the pyrene side chain directly interacted with the nanotubes surface as expected. Accordingly, both fluorescence spectroscopy and ^{1}HNMR measurements proved the successful formation of PEGylated SWNT.

To gain a quantitative insight into the relative amount of the incorporated pyr-PEG on the SWNTs, thermogravimetric analysis (TGA) was carried out under the condition as described in the experimental section. According to TGA results, while short and long SWNTs are thermally stable up to 800 °C, pyr-PEG coated SWNTs experienced significant weight losses.

The thermal degradation of SWNT coated with pyr-PEG is a multistage process (Figure 3.8). At temperatures up to 150 °C, a slight weight loss was detected regarding the evaporation of the adsorbed water. The degradation between 250 and 450 °C was attributed to the decomposition of PEG chains. Additional weight loss observed from 500 to 600 °C can be ascribed to the decomposition of pyrene attached to the PEG chains.
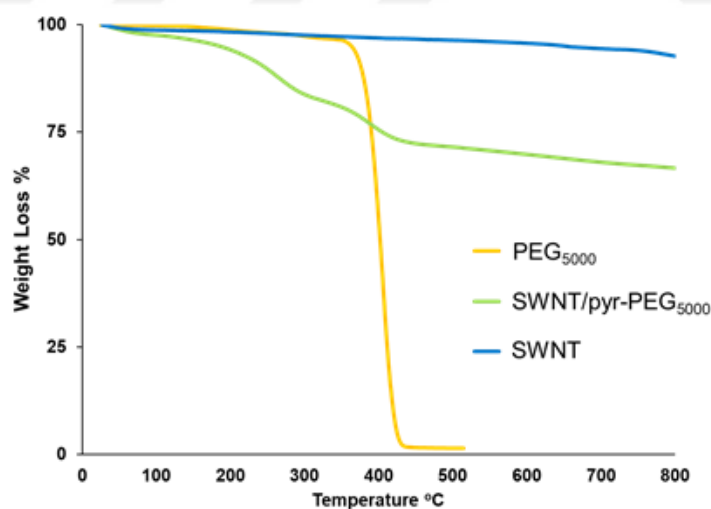
Figure 3.8 : Thermogravimetric curves of PEG$_{5000}$, short SWNT and Short SWNT/pyr-PEG$_{5000}$.

It is kown that the length of PEG chains did not affect the interaction energy of pyrene to SWNT. On the other hand, PEG chain length may play a significant role for attachment on the SWNTs. At this point, solvents with different polarities such as THF and dichloromethane (DCM) can provide an insight into this phenomenon. As it can

24

be seen from Figure 3.9, the amount of the linkage of pyr-PEG to SWNTs (both sSWNT and lSWNT) in DCM exhibited completely different trends compared to the THF results. As the molecular weight of PEG increased for the samples that were prepared in THF solvent, the amount of weight loss increased. However, in the case of DCM, this amount experienced an increase up to pyr-PEG$_{5000}$ subsequently a sharp decrease observed for pyr-PEG$_{12000}$. This can be attributed to the lower polarity index of DCM with respect to THF, which hinders the movement and therefore the diffusivity of pyr-PEG chains in the solvent. This effect of solvent is more pronounced once pyr-PEG$_{12000}$ was used for the coating. Therefore, to achieve a successful coating of SWNT, we used THF as a solvent for further studies. TGA analysis also revealed that the amount of noncovalent linkage for the pyr-PEG coated SWNT samples with sSWNT was higher than that of lSWNT. This can be attributed to the higher attachment of pyr-PEG to sSWNT because of its lower length with respect to lSWNT.
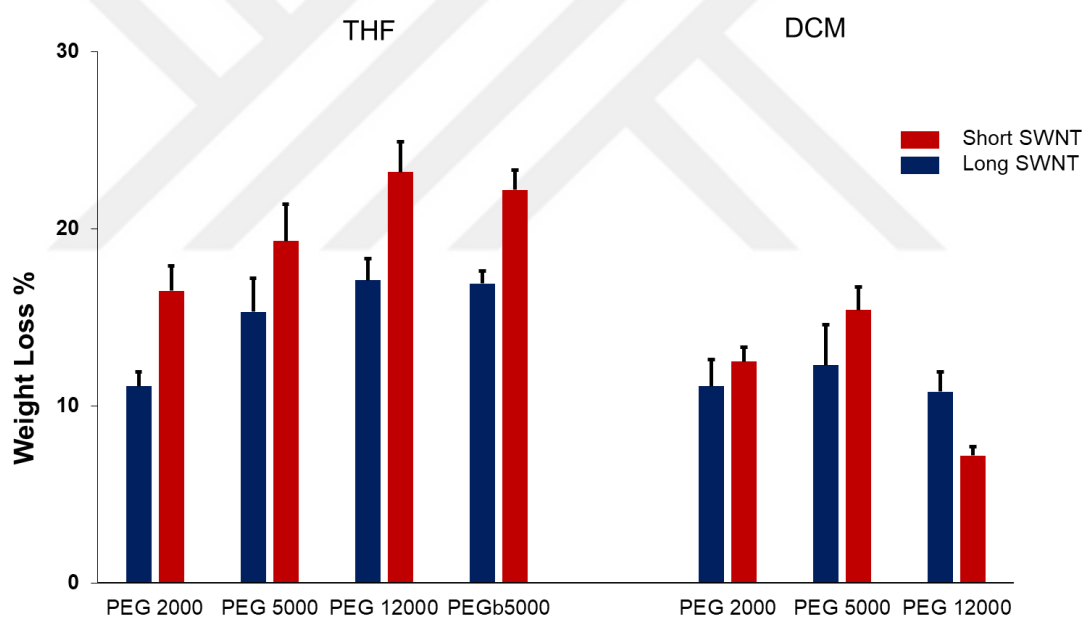
Figure 3.9 : Thermogravimetric results for SWNTs coated with pyr-PEG$_{2000}$, pyr-PEG$_{5000}$, pyr-PEG$_{12000}$ and pyr-PEG$_{b5000}$.

The number of nanotubes per unit volume for sSWNT in the solvent was higher than that of lSWNT, this may increase the number of successful collisions between pyr-PEG and sSWNT. Besides, the noncovalent linkage quantity for pyr-PEG$_{12000}$ was higher than that for the pyr- PEG$_{2000}$ and pyr- PEG$_{5000}$ samples obtained with both lSWNT and sSWNT. Thermogravimetric analysis for branched PEG$_{5000}$ demonstrated that the amount of PEG$_{b5000}$ binding onto the surface of short and long SWNTs was measured to be ~ 17 % and ~22 %, respectively. The quantity was slightly lower than

that of PEG_{12000}. It seems that although the PEG chain increase led to higher binding for linear PEG, however, in the case of branched PEG_{5000} has an upper limit $\sim 22\%$. To further gain insight into the efficiency of PEGylation, *in vitro* cytotoxicity, in vitro confocal microscopy imaging and in vivo blood circulation time studies were performed.

3.3 In Vitro Cell Viability

MTT and WST-1 assays were used to evaluate the effect of PEGylated SWNT on Human Umbilical Vein Endothelial (HUVEC) viability. HUVEC cell lines were utilized and treated with the short and long SWNTs coated with pyr-PEG_{2000}, pyr-PEG_{5000}, pyr-PEG_{12000} and at pyr-PEG_{b5000} concentrations of 5, 10, 50 and 100 µg/mL. The MTT viability results for pristine SWNT showed that the fabricated carbon nanotubes were cytotoxic at the applied concentration (Figure 3.10)(The asterisk (☐☐) denotes a statistically significant difference as for Student's t-test between long SWNT and short SWNT ($p \leq 0.05$)). After 12 h incubation, lSWNT coated with pyr-PEG_{2000} exhibited more cytotoxic effect on the cell viability than sSWNT coated with pyr-PEG_{2000} in all concentrations (Fig. 3.11).
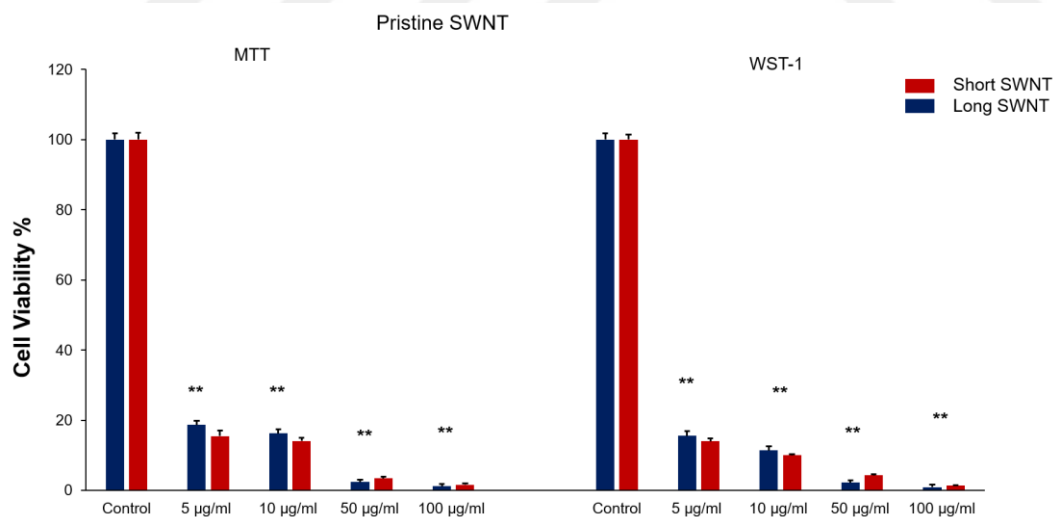
Figure 3.10 : Cell viabilities results for the pristine short and long SWNT.

Similarly, after an exposure time of 12h, lSWNT coated with pyr-PEG_{5000}, pyr-PEG_{12000} and pyr-PEG_{b5000} were observed with higher cytotoxicity behavior relative to sSWNT counterparts (Figure 3.12, 3.13 and 3.14). Analysis of MTT data with Student's t-tests revealed that the cell viability was decreased significantly after treatment with PEGylated lSWNT compared to the sSWNT. MTT assay demonstrated

that sSWNT had lower cell proliferation inhibition behavior when compared to lSWNT. Furthermore, WST-1 *in vitro* cell viability assay was performed to verify the reproducibility of the results. Likewise, lSWNT coated with different pyr-PEG reflected the same inhibitory trend of cell viability compared to the sSWNT counterparts.
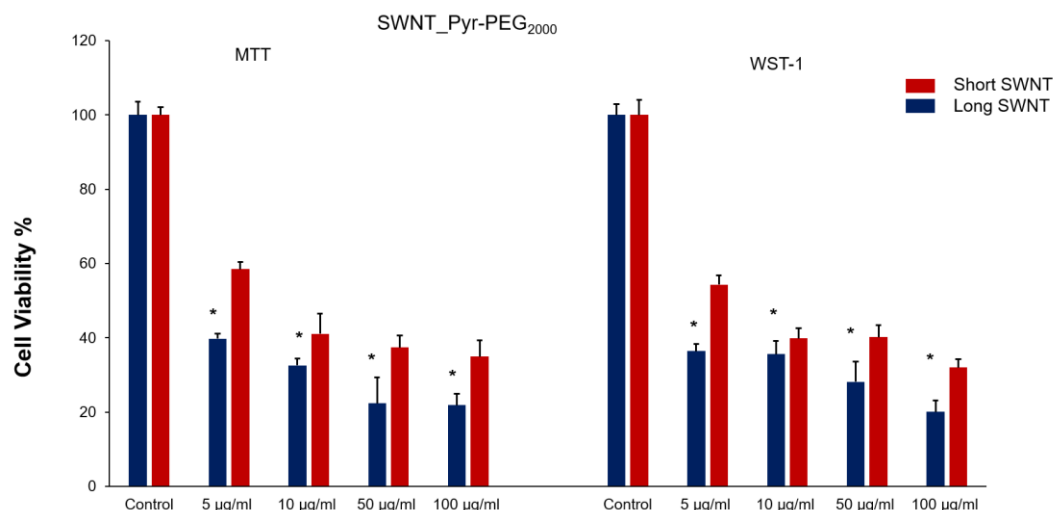
Figure 3.11 : Cell viabilities results for lSWNT and sSWNT coated with pyrene-PEG$_{2000}$ groups (p ≤ 0.05).
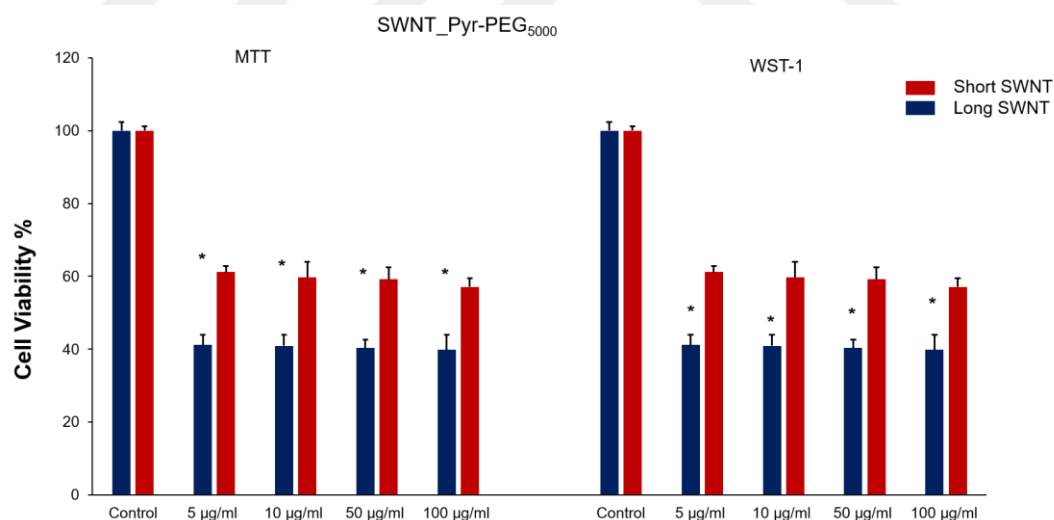
Figure 3.12 : Cell viabilities results for lSWNT and sSWNT coated with pyrene-PEG$_{5000}$ groups (p ≤ 0.05).

The enhanced cell growth inhibition with decreasing the PEG chain length corresponds to the fact that the molecular weight of PEG polymers plays a critical role in camouflaging the SWNT sidewalls. Briefly, WST-1 exhibited the same viability pattern for PEGylated SWNT cytotoxicity, thus, supporting the results obtained from the MTT assay. These results indicated that the short SWNT coated with longer PEG

chains has excellent safety and biocompatibility over a wide range of concentrations among the fabricated nanocarriers.
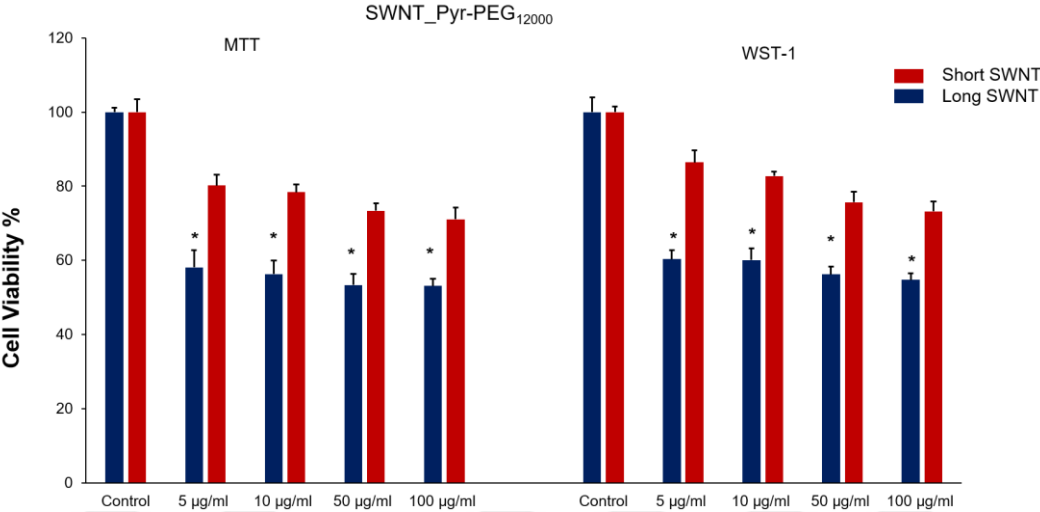
Figure 3.13 : Cell viabilities results for lSWNT and sSWNT coated with pyrene-PEG$_{12000}$ groups (p ≤ 0.05).
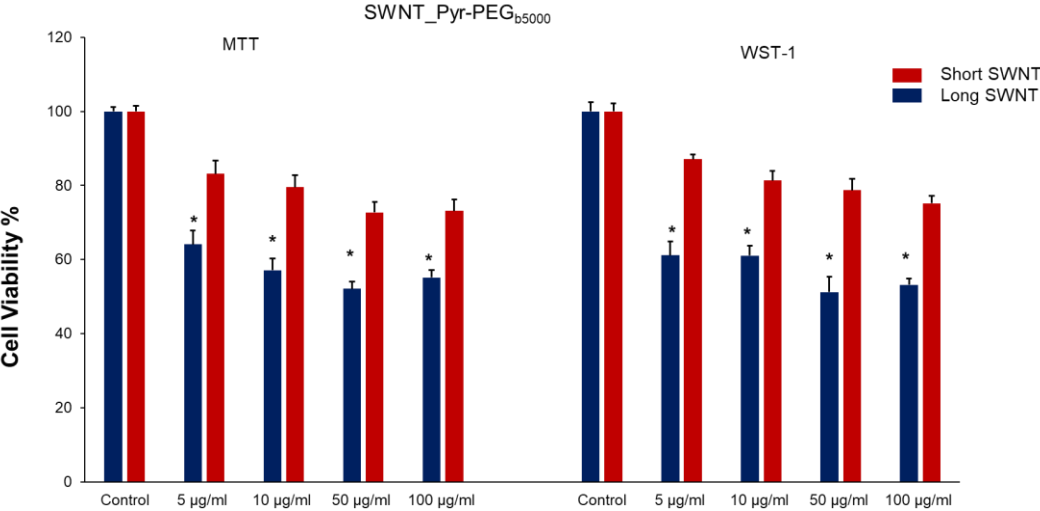
Figure 3.14 : Cell viabilities results for lSWNT and sSWNT coated with pyrene-PEG$_{b5000}$ groups (p ≤ 0.05).

3.4 In Vitro Confocal Microscopy Imaging

The actin cytoskeleton plays a major role in the physiology of endothelial cells including motility, adhesion, and permeability [75]. To visualize the effect of PEGylated carbon nanotubes on the actin cytoskeleton, actin filaments were fluorescently labeled with Phalloidin-TRITC in human umbilical vein endothelial cells (HUVECs) (Figure 3.15). HUVECs cultured in control conditions displayed both cortical (peripheral) and stress fibers. In this study, the PEGylated SWNT treated and

control HUVECs showed differences and similarities in the filament distribution information.
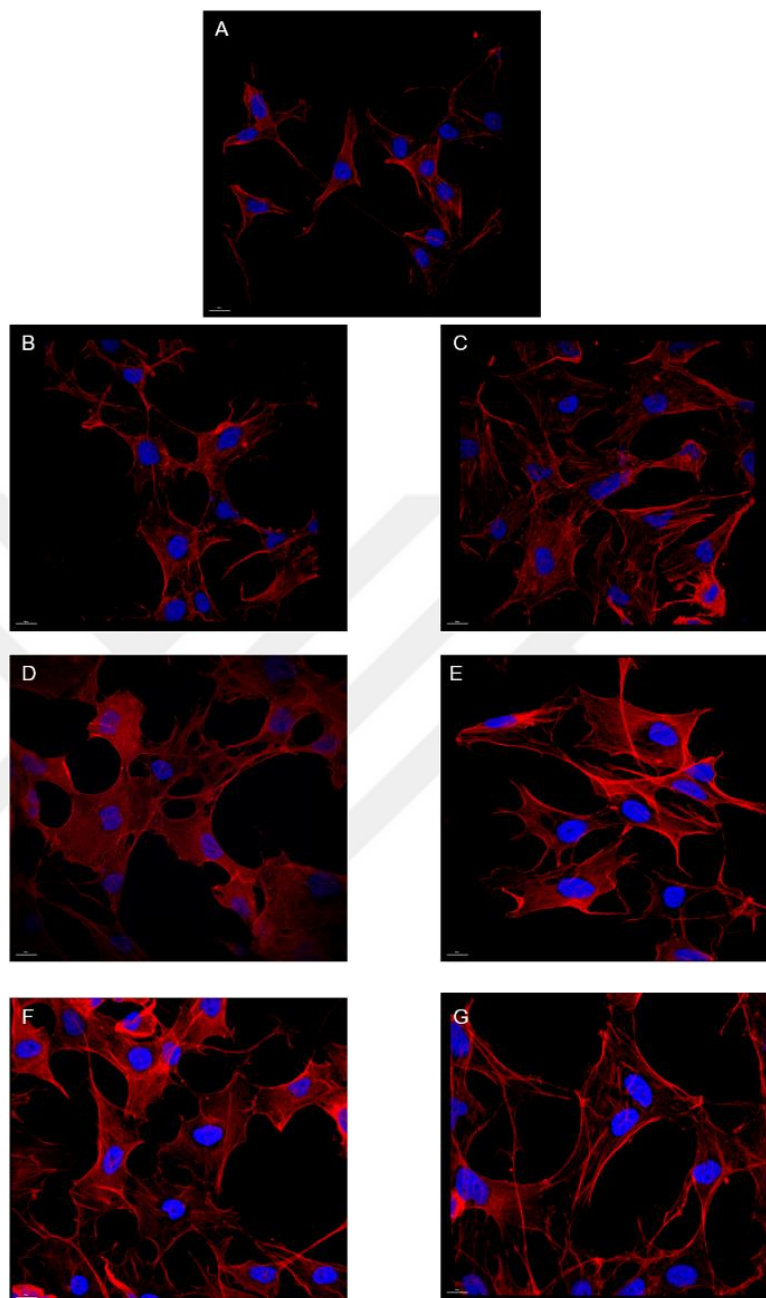
Figure 3.15 : Confocal fluorescence microscopy images of the actin cytoskeleton in HUVECs treated with PEGylated SWNT (a) Control, (b) Short SWNT/PEG$_{2000}$, (c) Long SWNT/PEG$_{2000}$, (d) Short SWNT/PEG$_{5000}$, (e) Long SWNT/PEG$_{5000}$, (f) Short SWNT/PEG$_{12000}$, (g) Long SWNT/PEG$_{12000}$.

Actin re-organization and cell shape changes were observed in cells treated with the short and long SWNT at all concentrations especially for the long SWNTs coated with pyr-PEG$_{2000}$. However, the actin filaments were occurred to interestingly be more comparable to the control cells (Figure 3.15 f-g) once treated with the short and long

SWNT/pyr-PEG$_{12000}$. The breakdown of actin filament occurred for the cells treated with the long SWNT/pyr-PEG$_{5000}$ (Figure 3.15 d,e). The impaired membrane integrity decreased as the molecular weight of PEG decreased for both short and long SWNTs.

In recent years, SWNT-based nanoparticles offer promising perspectives to the field of regenerative medicine including in situ cell engineering, building in vitro disease models, and in vitro instruction of therapeutic cells such as artificial extracellular matrixes[76]. The functionality of endothelial cells is essential for the vascular system [77]. SWNT can easily enter the bloodstream, consequently, endothelial cells would be the primary cells exposed to these nanoparticles [78]. Currently, a complete understanding of how SWNT interact with endothelial cells at the molecular level remains unclear. The cytoskeleton plays a fundamental role in many cellular processes including maintaining cellular shape, endosomal transport, cell polarity, cell division and formation of motility structures especially signal pathways with interacting many proteins [79]. In this study, HUVECs were considered to approximately characterized the endothelial cells in blood vessels. Actin filament rearrangement was correlated to direct contact of PEGylated SWNT with the HUVEC cells. It was observed that changes in actin organization as well as similar changes in cell proliferation. PEGylated SWNT effects were dose-dependent and most likely associated with mechanical damage to the cell membrane by actin re-organization. On the other hand, other SWNTs with low and higher dose treatment affected the cell viability and actin re-arrangement.

This can be attributed to the actin reorganization, which is involved in vital functions of the cells as it plays a practical role in important signal pathways. The study demonstrated that HUVEC cells experienced actin cytoskeleton disruption and induced reticulated fibrils formation, and a concomitant diminished viability as a result of exposure to long SWNTs coated with the low molecular weight of PEGs. This resulted in disruption of the actin cytoskeleton and the intercellular interactions which may have multiple effects on endothelium function. However, the endothelial cells extremely tolerated the high concentrations of short SWNT coated with PEG$_{12000}$ and PEG$_{b5000}$ without changes in viability, cytoskeleton, and function.

3.5 In Vivo Blood Circulation Time Studies

To investigate *in vivo* blood circulation time for the PEGylated SWNTs, eight-week-old BALB/c mice were used. Each sample was intravenously injected into the tail vein as seen in Figure 3.15. Raman spectroscopy was employed to measure the amount of SWNTs inside the blood using the density of the G bands. To achieve this, PEGylated SWNT solutions were prepared and the density of the G bands were recorded at 808 nm.

Liu et al. [66] have showed that PEGylated SWNTs exhibit similar Raman intensities in different mediums. They proposed that the Raman intensity of SWNTs independent and relatively insensitive to the molecular weight of PEG and type of the medium. Therefore, intrinsic NIR features of SWNTs can be exploited by using Raman intensity in PEG coated nanotubes.

Figure 3.16 : Eight-week-old BALB/c intravenously inject from the tail vein.

The *in vivo* blood circulation time results for PEG_{2000}, PEG_{5000}, PEG_{12000} and branched PEG_{5000} are presented in Figure 3.16. It was observed that as the molecular weight of PEG polymer increases from the 2 kDa to 12 kDa, the amount of blood circulation time appreciably increased (up to ~ 7h). These results are in consistent with the results of in vitro studies.

Nevertheless, SWNTs coated with branched PEG_{5000} chains experienced an outstanding increase in circulation to ~13.5 h. These results are indicative that branched PEG_{5000} structures on SWNTs can afford the optimal biological properties that avoid the nanotubes to be removed from the blood stream. This feature of SWNTs

can be attributed to the efficient coverage of SWNTs surface due to the compact density of hydrophilic PEG polymers on SWNTs.
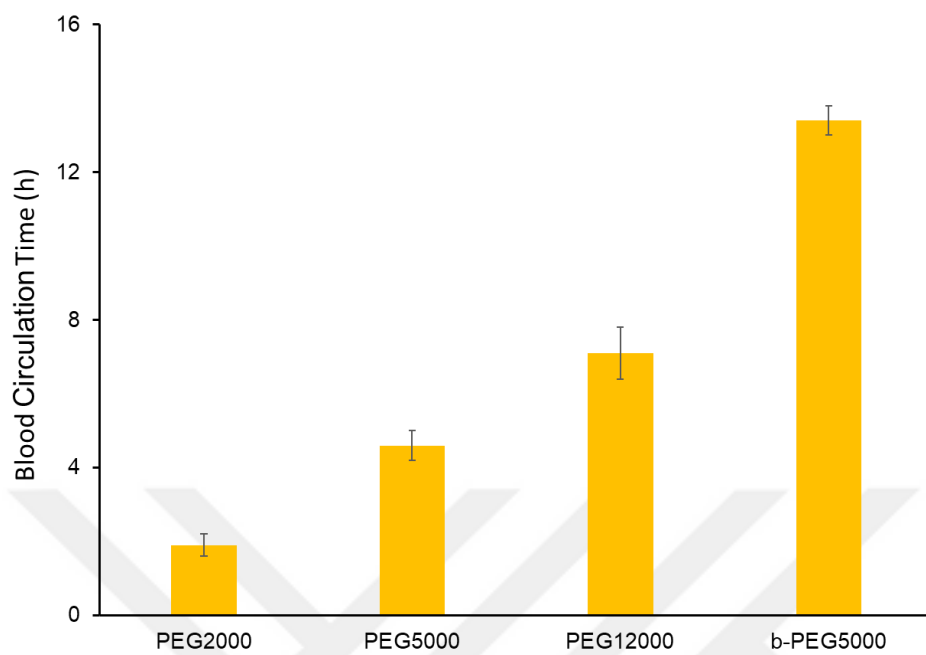
Figure 3.17 : *In vivo* blood circulation time results for PEG coated SWNTs nanocarriers.

4. DOX LOADED SWNTS FOR RECEPTOR-TARGETED DELIVERY

SWCNTs have been exploited as a nanoplatform for the delivery of various low molecular weight targeting agents, biomolecules and antibodies. Such nanoplatforms provide markedly efficacy after internalization into the intracellular matrix[80, 81]. The present chapter addresses the development and investigation of release performance of doxorubicin (DOX) loaded folate receptor-targeted PEGylated SWNTs for breast cancer therapy.

4.1 DOX Delivery

One of the low molecular weight agents that have been used extensively with PEGylated SWNTs as nanoplatfrom for therapy purpose is DOX. DOX is a chemotherapy medication drug used for the treatment of various types of cancer such as breast cancer, esophageal carcinomas, acute lymphocytic leukemia, bladder cancer and lymphoma since late 1960s [82]. To improve the pharmacokinetics and bioavailability of this anticancer drug, several studies have been conducted in order to enhance the efficiency of the DOX. Chemical structure of DOX is depicted in Figure 4.1.
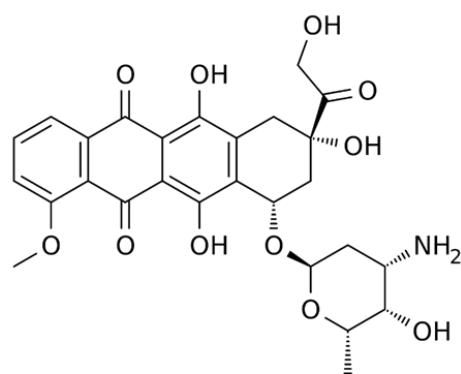
Figure 4.1 : Chemical structure of DOX molecule.

To clarify the antimitotic and cytotoxic activity of DOX, a number of mechanisms of action for DOX proposed by different researchers. Formation of complexes with DNA and disruption of base pairs, generation of reactive oxygen species by lipid

peroxidation in cell membrane, formation of iron-related free radicals and mitochondrial disruption all leads to apoptotic pathways activation which triggers cell death [83, 84].

There are some adverse side effects of conventional DOX therapy. Irreversible cardiomyopathy is one of the long-term aggressive effect of DOX administration. To overcome such irreversible cardiomyopathy and other severe side effects, PEGylated liposomal drug delivery methods [85, 86] polymeric micelles, inorganic materials and carbon based nanomaterials were employed. Among the aforementioned nanomaterials, carbon nanotubes hold promising applications specifically for molecular delivery in various types of cancer.

In this part of the chapter, we will explore synthesis of Folic acid targeted SWNTs followed by investigation of the DOX loading and release performance for PEGylated SWNTs.

4.2 Nanoparticle Synthesis and Characterization

4.2.1 Synthesis of folic acid bearing PEGylated SWNTs

Folic acid (FA) functionalized SWNTs are promising carbon based nanocarriers for targeted delivery of biomolecules to tumor sites. FA is a type of B vitamin that as medication can be used in the treatment folic acid deficiency. FA has high affinity to the folate receptor α (FR-α) and binds to folate receptors that overexpressed on the surface of many types of cancer cells [87, 88].

To attach FA on the surface of SWNTs non-covalent attachment approach was utilized. The pyrene anchor of 1-pyreneacetic-acid (Figure 4.2) was used to bind FA to the SWNTs. It is worthy to note that the reaction took place between –NH$_2$ group of FA and –COOH group of pyreneacetic acid.

Therefore, an amide bond formed as result of reaction between pyr-AA and FA. The chemical structure of pyr-FA is given is Figure 4.3.

Mark and colleagues [89] was also used amide formation approach to attached FA on the surface of SWNTs. They first treated SWNTs with strong nitric acid to purify and to form carboxylic acid groups on the end and side walls of nanotubes.
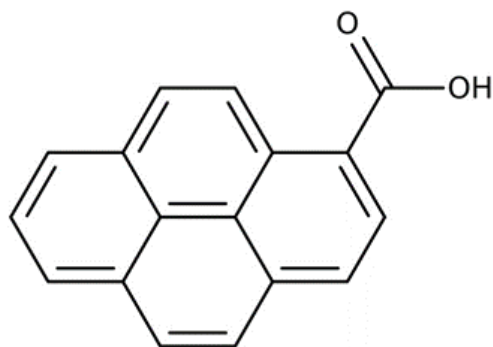
Figure 4.2 : Chemical structure of 1-pyreneacetic-acid.

Then, the mixture of FA with oxidized SWNTs in DMF as solvent were refluxed overnight. Their results exhibited that FA was chemically attached to the surface nanotubes.
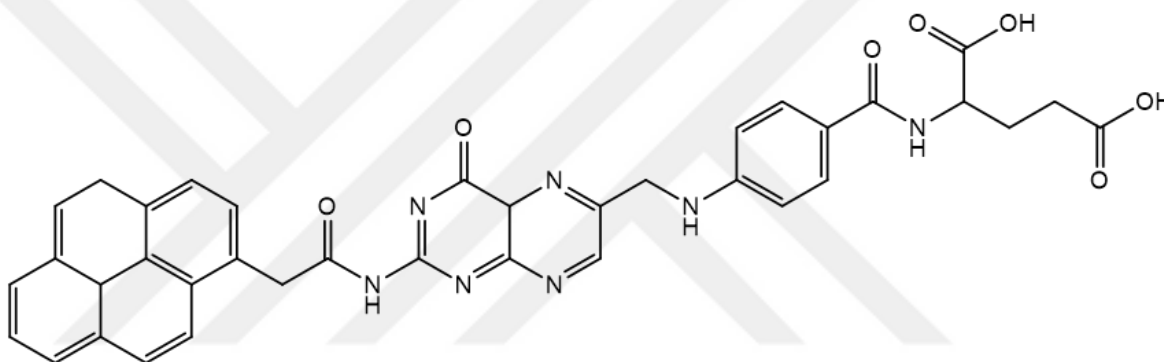
Figure 4.3 : Chemical structure of the synthesized pyr-FA.

In our case, ^{1}HNMR and FTIR analysis were employed to assess the reaction between Pyr-OH and FA. Figure 4.4 shows the FTIR spectrum for pyr-FA structure. As it can be seen, the characteristic peaks for –C=O stretch bond and aromatic double bond for pyrene-FA was obtained at 1574 cm^{-1} and 1625 cm^{-1} respectively. The formation of amide C–N stretch at 1296 cm^{-1} and amide N–H bends at 1530 and 1510 cm^{-1} corroborates the attachment of FA to the nanotubes.

^{1}HNMR measurement also verified the formation of pyr-FA structure (Figure 4.5). The characteristic peaks of pyrene aryl group (δ = 8–8.2 ppm, ArH) and folic acid functional groups ($\delta \sim$ 5.85 ppm (a), 4.62 ppm (b), 6.64 ppm (c), 7.1 ppm (d), 2 ppm (e), 7.6 ppm (f), 2.5 ppm (g) ppm) are all presented in the Figure 4.5. The obtained results were further confirmed the formation of pyr-FA.
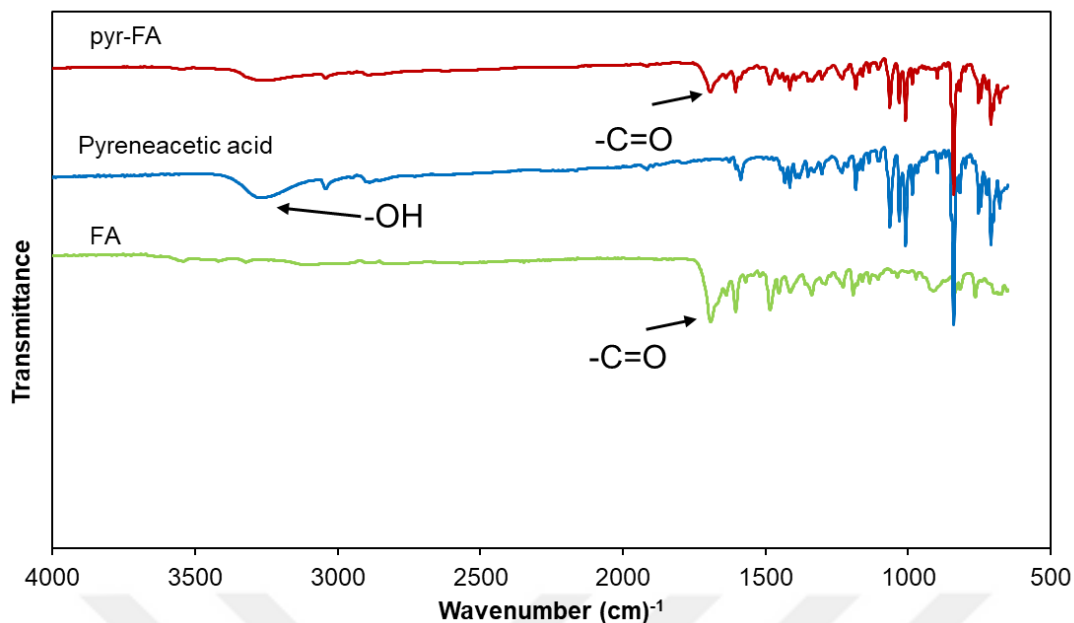
Figure 4.4 : FTIR characterization of FA, pyreneacetic acid and pyr-FA.
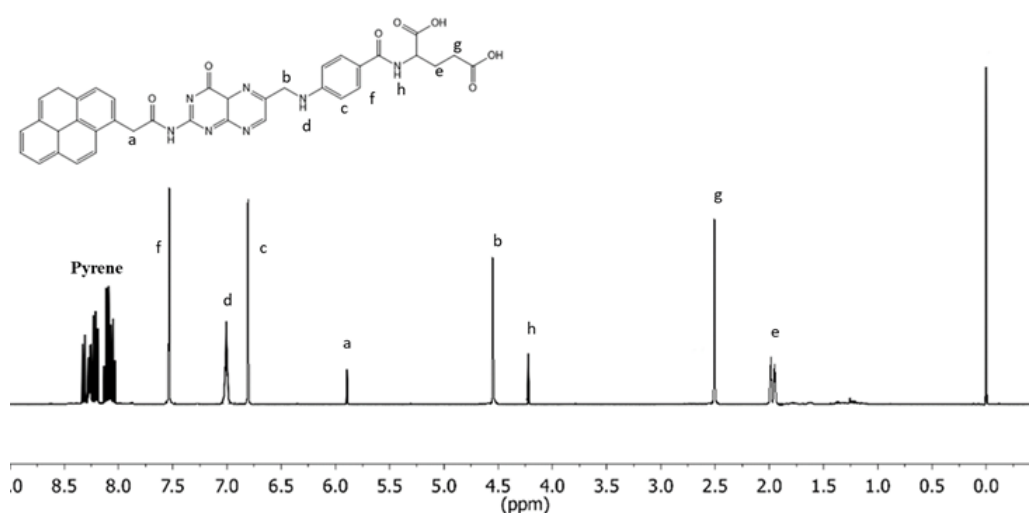
Figure 4.5 : ^{1}HNMR characterization of pyr-FA.

These two characterization methods were used to be assured that the amide bond was successfully formed between FA and pyreneacetic acid. In the next step, the obtained pyr-FA powder was utilized to physically mix with SWNTs. The objective was to achieve FA functionalized SWNTs. This nano-structure was then dispersed in THF and was mixed branched PEG$_{5000}$ and PEG$_{12000}$ separately.

The amount of pyr-FA binding to SWNTs would play important role in targeted delivery of DOX molecules to the tumor tissues. Thus, the efficacy of the non-covalently coating of SWNTs with pyr-FA was required to be investigated.

The TGA results for short SWNTs coated with pyr-FA and pyr-PEGb$_{5000}$/pyr-FA are presented in Figure 4.6. Although, in PEGylation of SWNTs two different nanotubes in terms of length were employed, due to the higher cytotoxicity of long SWNTs, in all DOX loading and release studies, only short SWNTs were utilized. As mentioned before, through the purification of SWNTs small of amount of functional groups can be formed on the end caps of nanotubes. The observed nearly 7 % weight loss for pristine SWNTs can be attributed to these functional groups disappearance while the heat flow reaches to higher temperatures in TGA analysis. In the case of pyr-FA, the amount of weight loss reached to about 20 %.
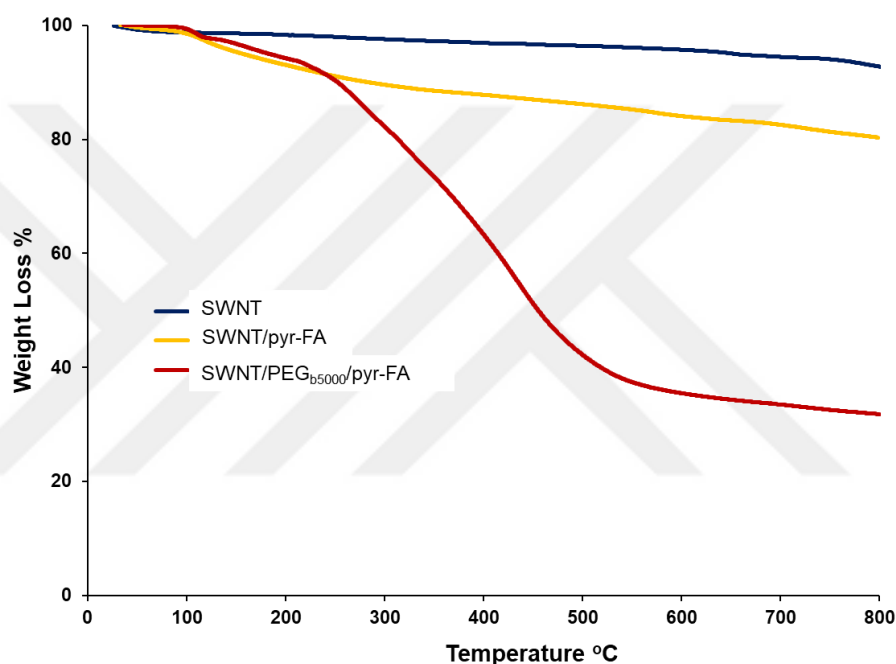
Figure 4.6 : Thermogravimetric results of short SWNTs coated with pyr-FA and SWNT/PEG$_{b5000}$/pyr-FA.

It is needed to mention that in this part of the study for all SWNTs coating, we applied 1mg SWNTs/5 mg PEG to achieve the desired PEG coated SWNTs. However, for FA functionalized SWNTs, the weight ratio was lower than 1/5 due to the fact that using the similar amount for pyr-FA would cover SWNTs surface to huge amount with pyr-FA and therefore, conjugation of PEG onto SWNTs in the next step would significantly drop. Based on this consideration, we applied 1mg SWNTs/2 mg pyr-FA formula followed with 1mg SWNTs/5 mg PEG formula. It means that we first coated SWNTs with pyr-FA afterward, FA functionalized SWNTs were treated with branched PEG$_{5000}$ and PEG$_{12000}$. The pure amount of weight loss for SWNTs/pyr-FA was 12 %. These results corroborate the attachment of FA on the side walls of nanotubes. Thus

far, we achieved receptor targeted SWNTs by employing FA. However, biocompatible SWNTs are required for cancer therapy purpose. Therefore, the synthesized SWNT/pyr-FA complex was coated with both branched PEG_{5000} and PEG_{12000} which provide higher biocompatibility to the nanotubes.

Interestingly, the amount of binding for $SWNT/PEGb_{5000}/pyr$-FA is significantly higher than that of SWNTs coated with pyr-FA. The result indicates that incorporation of branched PEG_{5000} to the SWNT/pyr-FA led to high amount of weight loss. It can be said that the fabricated SWNTs has coated successfully with branched PEG_{5000} and has the targeted agent necessary for targeted delivery.

4.3 Drug Loading on SWNTs

Due to their intriguing features, CNTs have been used as drug delivery nanocarriers specially for the delivery of anticancer drugs. Various studies have been conducted to enhance the amount of drug accumulation in tumor tissues. To conjugated the anticancer drugs on to CNTs covalent and noncovalent approach can be applied. In this study, noncovalent types of attachment were employed. In the literature, this type of drug loading attracted huge amount of attention from various research groups. Camptothecin (CPT) as an anticancer drug was non-covalently attached onto poly (vinyl alcohol) (PVA)-functionalized MWNTs via $\pi-\pi$ interactions in PBS buffer of pH 7.4 at 37 °C. The purpose of the study was to raise water solubility and antitumor effect of CPT [90]. In an *in vitro* study by Nahid et al [82], the group developed PEGylated MWNTs to be used for DOX delivery to HeLa cells. The loading studies was conduct in PBS medium at pH 5. In an another study, Co-delivery of DOX and paclitaxel (PTX) were investigated using amphiphilic triblock copolymer as drug carrier [91]. In their study, despite using triblock copolymer, $\pi-\pi$ interactions between amphiphilic polymer and DOX and PTX provided the core fragment of the nanovehicle. The loading for codelivery of DOX and PTX process was performed in ambient temperature and pH was adjusted to pH 7-7.5.

In our study, DOX loading studies were conducted in two step. At first step, short and long SWNTs were dissolved in buffer solutions with different pH to understand its effect on the amount of DOX loading. UV–vis spectrometer was used to explore the amount of DOX loading and release. To gain a clear understanding to the characteristic peak of DOX wavelength scan was conducted between 350-650 nm. It is observed that

490 nm can be exploited for further studies. Accordingly, 490 nm was used for DOX loading and release studies.

The measurement of UV–vis absorbance for DOX loaded short and long SWNTs at different pH medium (pH= 5.5, 7.4 and 9) are presented in Figure 4.7. It can be seen that the amount of loading for both short and long SWNTs are pH-dependent. Furthermore, the amount of DOX loading for both short and long SWNTs exhibit a maximum performance at pH = 9. By moving from basic pH to the acidic medium, a substantial decline in DOX loading was observed for both SWNTs. It can be clearly said that the best medium for noncovalent loading of DOX is basic medium. On the other hand, short SWNT displayed slightly higher loading performance with respect to long ones. This may be due to the fact that as the number of SWNTs per weight of SWNTs increase in the medium the probability of the collision between DOX and nanotubes increase and this leads to a higher amount of DOX attachment to the sidewall of the SWNTs. Therefore, basic pH was used for DOX loading of all PEGylated SWNTs.
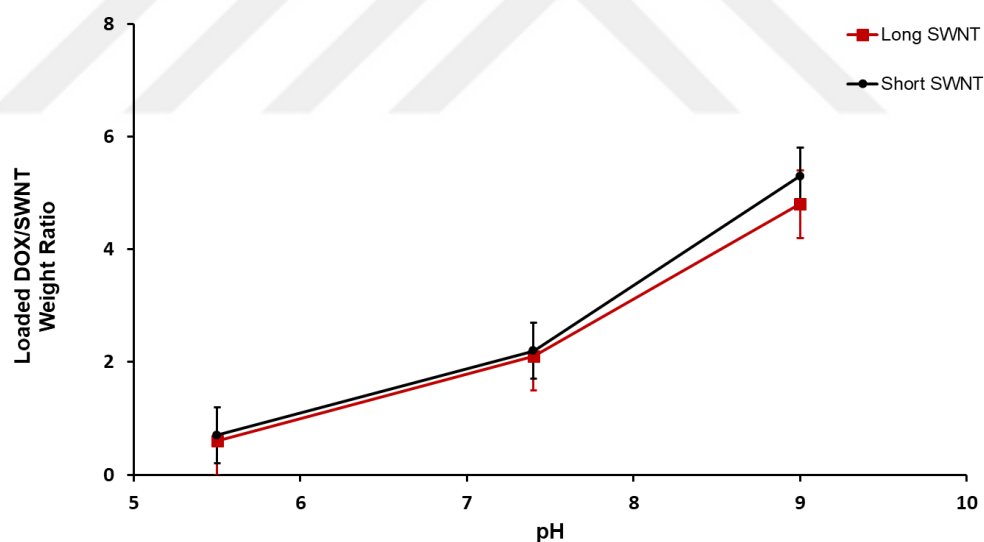
Figure 4.7 : pH-dependent loading of DOX on short and long SWNTs.

In the second step of DOX loading studies, PEGylated SWNTs were separately dissolved in basic buffer (pH=9) and then was simply stirred with DOX to achieve DOX laoded nanocarriers. The results of drug loading on SWNTs nanocarriers are represented in Figure 4.8.

It can be seen that as the molecular weight of the PEG increases the amount of loaded DOX on SWNTs showed an uptrend.
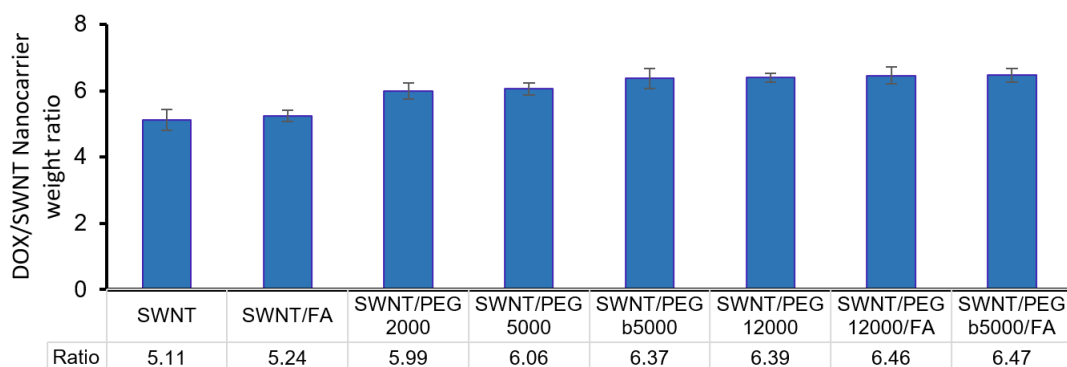
Figure 4.8 : DOX loading ratios for PEGylated short SWNTs at pH 9.

It seems that at higher pH values DOX molecules tend to stay away from hydrophilic aqueous medium because of low solubility and hydrophobic nature of doxorubicin at basic environments. Morover, DOX molecules have the capability to interact with PEG polymers leading to higher amount of drug binding. The caculated DOX/SWNTs ratios for different nanocarriers were in the rage of 5.11-6.47 % as shown in Figure 4.8. The obtained results are in consistant with the results reported in the literature[92]. Furthermore, FA conjugated nanocarriers that exhibited higher drug loading capacity with respect to their counterparts. It appears that DOX can interact with FA via Van der Waals interaction. In the literature, the attachment of DOX on SWNTs was linked up to the π–π stacking interactions between nanotubes and the aromatic nature of the DOX molecules[82, 92, 93]. Similar results were reported by Dai et al [92]. They fabricated supramolecular assembly of phospholipid functionalized SWNTs. The DOX loading studies at different pH showed that at lower pH the amount of loading decreased by factor ~ 4. As a consequence, to attain an effective DOX loading onto the SWNTs side walls, basic pH values can be preferred.

4.4 Drug Release Performance of FA Receptor-targeted PEGylated SWNTs

As is explained in the previous chapter, DOX release studies were conducted at 37 °C at pH 7.4 and pH 5.5 PBS buffered solutions. After different time intervals, the released DOX was assessed via UV-Vis spectroscopy. The cumulative release performance of the SWNTs non covalently coated with different PEG and FA were measured in physiological pH 7.4 and PH 5.5 typical of the micro-environments of cancerous tissue. As it can be seen in Figure 4.9 and Figure 4.10, the release of the DOX from SWNTs is clearly pH-triggered. The release performance of different

SWNTs nanocarriers displayed a slow and sustained release pattern in both pH values, and however, there were substantial differences between the release rates at pH 7.4 and 5.5. The release performance of the SWNT nanocarriers in physiological pH 7.4 shows that, after a quick release within 20 h, DOX release tended to be flat and the amount of release for the PEGylated samples were between 25-45% as shown in Figure 4.11. The difference observed between the release rate of PEGylated and pristine SWNTs is indicative that as the hydrophilicity of the PEGylated SWNTs increase, π-π stacking interaction between the DOX aromatic parts with the inner and outer side walls of SWNTs begin to weaken.
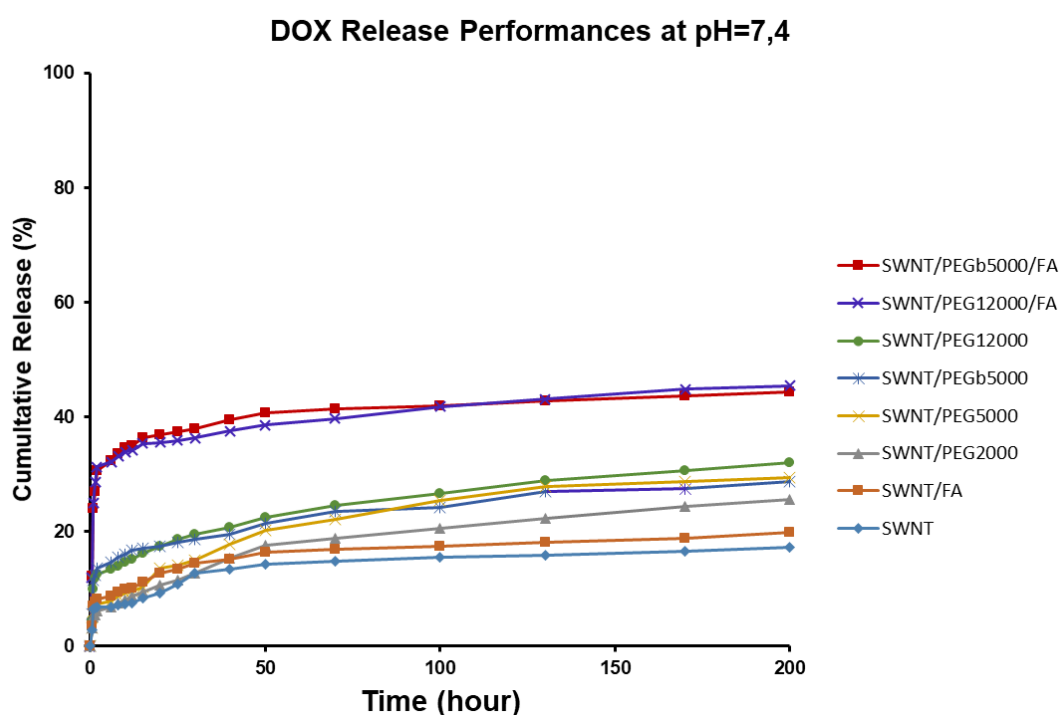
Figure 4.9 : Cumulative release profiles of various DOX loaded SWNT samples at pH 7.4.

Furthermore, the amount of release for PEGylated SWNTs/FA nanocarriers are higher than that of PEGylated SWNTs nanocarriers. This behavior might be due to the establishment of Van der Waals interactions between FA and DOX molecules which weaker than π-π stacking interaction between DOX and SWNTs. As it can be seen for SWNTs coated with branched PEG_{5000} and PEG_{12000}, there are noticeable difference between the release rates of these samples and PEG_{2000} and PEG_{5000}. Therefore, as the molecular weight of the PEG chain decreases the amount of cumulative release decreased which shows that the more hydrophilic the surface of SWNTs are, the higher amount of release can be obtained.
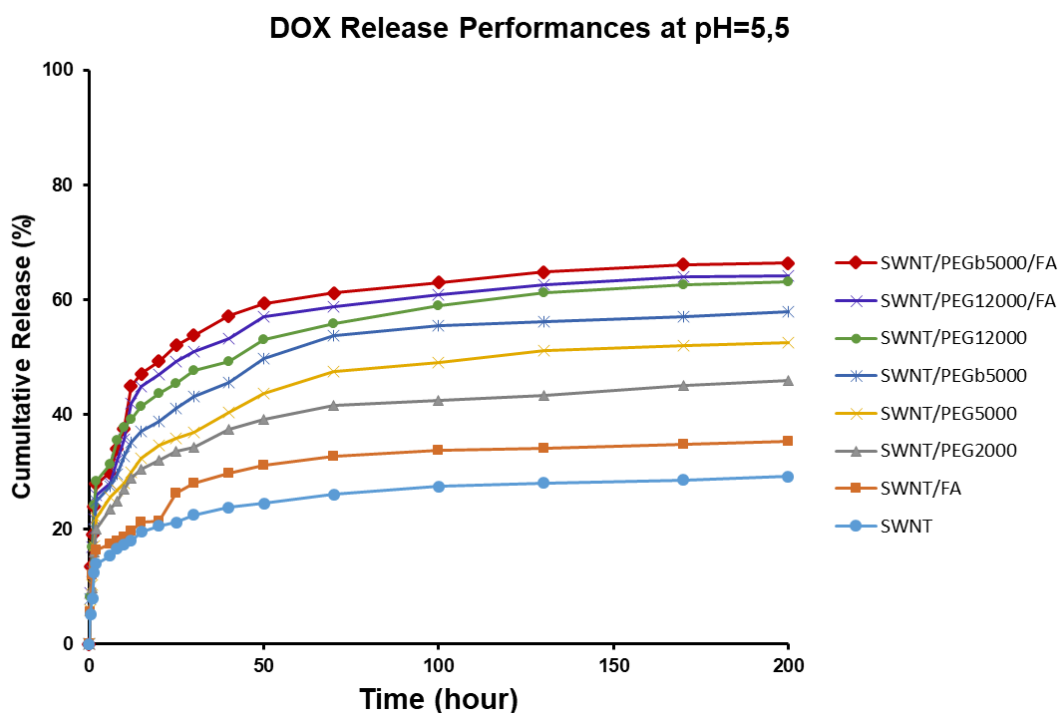
Figure 4.10 : Cumulative release profiles of various SWNT samples at pH 5.5.

This behavior aslo confirms that DOX molecules establish van der Waals interactions with PEG chains. The slow DOX release from pristine SWNTs might be ascribed to the strong hydrophobic interaction between DOX and the inner and outer side walls of the nanotubes. In the case of SWNT/DOX nanocarriers functionalized with FA, the amount of release increased compared with the non-FA-conjugated construct. It seems that incorporation of FA onto the SWNTs surface, due to weakening of π-π stacking interaction between SWNTs and DOX, the amount of cumulative release increased which validate once more that the degree of the hydrophilicity of the SWNTs controls the amount of DOX release from these nanocarriers. In similar studies, it was demonstrated that supramolecular CNT/DOX complexes functionalized with FA provide higher amount of loading and release performance leading to be taken up more effectively by cancerous tissues via FR-mediated endocytosis, leading to higher cytotoxicity than non-targeted CNT/DOX [93, 94].

pH-triggered drug release from the fabricated SWNTs nanotubes, in which the DOX is loaded onto the SWNTs surface under basic pH medium and released at pH 5.5, corresponding to lysosomal pH provide an in-depth understanding mechanism for DOX release from the nanocarriers. To explore this release behavior, SWNTs with and without tumor targeting properties, FA, were investigated at reduced pH value. The release performance for the same SWNTs samples at pH 5.5 are presented in Figure

42

4.10. Interestingly, the amount of release for all nanostructures experienced a substantial increase at pH 5.5 and was significantly affected by the environment acidity. Furthermore, the amount of release for PEGylated SWNTs are again higher than the SWNTs without coating. It appears that PEGylation of the SWNTs with hydrophobic surface led to the dispersion of the SWNTs due to the hydrophilicity that obtained by PEG chains. On the other hand, van der Wales interactions between DOX molecule and SWNTs require large surface area which significantly covered by PEG chains in PEGylated SWNTs.

	SWNT	SWNT/FA	SWNT/PEG 2000	SWNT/PEG 5000	SWNT/PEG b5000	SWNT/PEG 12000	SWNT/PEG 12000/FA	SWNT/PEG b5000/FA
pH=7.4	17.21	19.84	25.60	29.49	28.80	32.09	45.49	44.31
pH=5.5	29.20	35.40	46.03	52.61	58.02	63.07	64.18	66.42
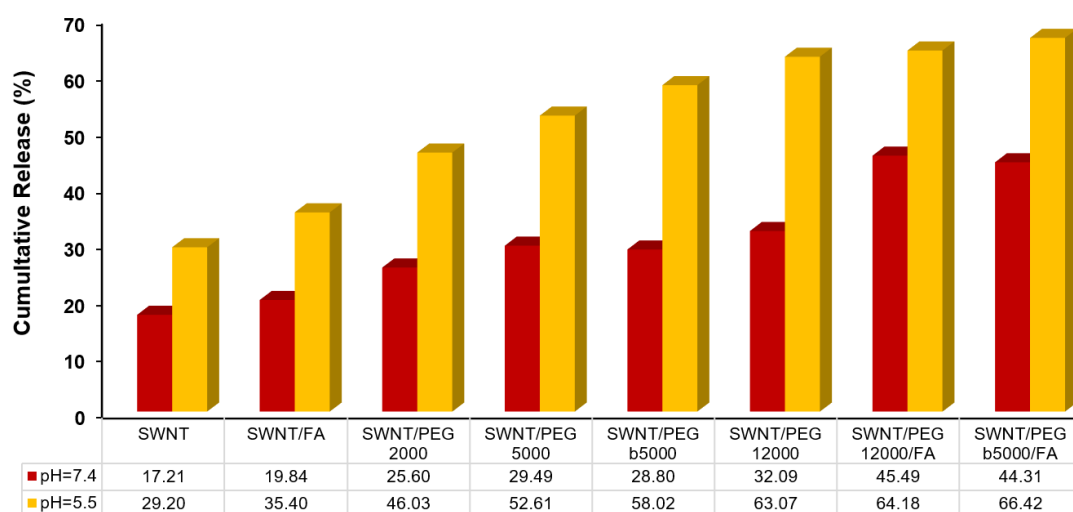
Figure 4.11 : Cumulative release amount for various SWNT nanocarriers at pH=7.4 pH=5.5.

Therefore, DOX molecules, which are in van der Wales interactions with PEG chains, due to the weaking of hydrophobicity of the DOX molecuels at acidic pH, tend to detach from the nanocarries. Morover, strong π- π interactions between DOX and SWNTs are available only in SWNTs without PEGylation. In acidic medium, π- π interactions between DOX and SWNTs weaken due to the protonation of the DOX molecule leading to detachment of the DOX from the SWNTs surface. The similar behaviors can be observed for SWNTs coated with low molecular weight PEG. In this case, as the length of PEG chain decreases the hydrophobicity of the SWNTs increases which provides strong π- π interactions between DOX and SWNTs.

The results of release performances for the fabricated SWNTs nanocarries were compared in Figure 4.11. It can be seen that the amount of release at pH=5.5 are higher than that at pH=7.4. The amount of release at pH=5.5 increased between 11.99– 22.11 %. Consequently, as the molecular weight of PEG chain increases the amount of

release increase for PEGylated SWNTs for both pH. The remarkable DOX release at pH 5.5 for FA-conjugated SWNTs/DOX systems might be ascribed to the significantly increased protonation degree of the $-NH_2$ group in DOX molecules resulting in the weakening of π- π interactions interactions between the SWNTs nanoparticles and DOX molecules. In the literature, there are similar result for FA-conjugated CNT/DOX system in which FA bearing SWNTs systems are more efficient than non-FA-conjugated nanostructures apparently due to slow rate of DOX release [93].

4.5 Kinetic Modelling Studies of DOX Loaded Nanocarriers

There are number of kinetic models, which designates the overall release of drug from the nanomaterials. Because qualitative and quantitative changes in a formulation may alter drug release and in vivo performance, developing tools that facilitate product development by reducing the necessity of bio-studies is always desirable. In this regard, the use of *in vitro* drug dissolution data to predict *in vivo* bio-performance can be evaluated as the comprehensible development of controlled release formulations. Zero-order model, First-order model, Higuchi and Korsmeyer-Peppas are four models, which were investigated the kinetics of drug release from PEGylated SWNTs.

Drug dissolution from dosage forms that do not disaggregate and release the drug slowly can be represented by Zero-order model. To study the release kinetics, data obtained from in vitro drug release studies were plotted as cumulative amount of drug released versus time. First-order model has been used to describe absorption and/or elimination of some drugs although it is challenging to theorize this mechanism on a theoretical basis. The data obtained are plotted as log cumulative percentage of drug remaining vs. time, which would yield a straight line with a slope of -K/2.303.

The first example of a mathematical model aimed to describe drug release from a matrix system was proposed by Huguchi in 1961 [95]. Initially conceived for planar systems, it was then extended to different geometrics and porous systems. This model is based on the hypotheses that (i) initial drug concentration in the matrix is much higher than drug solubility; (ii) drug diffusion takes place only in one dimension (edge effect must be negligible); (iii) drug particles are much smaller than system thickness; (iv) matrix swelling and dissolution are negligible; (v) drug diffusivity is constant; and (vi) perfect sink conditions are always attained in the release environment.

Korsmeyer and colleagues [96] developed a modest relationship which defined drug release from a polymer based system equation. To figure out the mechanism of drug release, first 60% drug release data were fitted in Korsmeyer-Peppas model. In this model, the value of n characterizes the release mechanism of drug. For the case of cylindrical tablets, 0.45 ≥ n corresponds to a Fickian diffusion mechanism, 0.45 < n <0.89 to non-Fickian transport, n = 0.89 to Case II (relaxational) transport, and n > 0.89 to super case II transport (37, 38). To discover the exponent of n the portion of the release curve, where $M_t / M_\infty < 0.6$ should only be used. To study the release kinetics, data obtained from in vitro drug release studies were plotted as log cumulative percentage drug release versus log time.

Table 4.1 : n, k and regression values obtained from Zero-order, First-order, Higuchi and Korsmeyer Peppas Equation for DOX loaded PEGylated SWNTs.

Nanocarrier	Kornsmeyer-Peppas				Higuchi				Zero Order		First Order	
	pH =7.4		pH =5.5		pH =7.4		pH =5.5		pH =7.4	pH =5.5	pH =7.4	pH =5.5
	r^2	n	r^2	n	r^2	k	r^2	k	r^2	r^2	r^2	r^2
SWNT	0.93	0.22	0.93	0.22	0.91	30.71	0.90	40.44	0.81	0.72	0.75	0.56
SWNT/FA	0.95	0.21	0.95	0.22	0.93	36.89	0.92	35.96	0.78	0.76	0.70	0.66
SWNT/PEG$_{2000}$	0.95	0.32	0.91	0.26	0.98	13.47	0.86	37.33	0.90	0.66	0.79	0.48
SWNT/PEG$_{5000}$	0.93	0.32	0.93	0.28	0.98	11.30	0.91	31.27	0.92	0.74	0.81	0.54
SWNT/PEG$_{b5000}$	0.97	0.16	0.94	0.27	0.98	41.61	0.91	33.31	0.90	0.72	0.81	0.54
SWNT/PEG$_{12000}$	0.96	0.21	0.95	0.23	0.99	32.23	0.90	37.86	0.90	0.72	0.81	0.56
SWNT/PEG$_{12000}$/FA	0.95	0.10	0.95	0.27	0.89	65.66	0.86	34.76	0.74	0.66	0.66	0.53
SWNT/PEG$_{b5000}$/FA	0.95	0.10	0.95	0.25	0.82	66.04	0.85	36.93	0.61	0.64	0.54	0.53

In our study, a model-dependent approach was used to clarify drug release mechanisms and kinetics. To apply the model-dependent approach, drug release data were fitted to aforementioned models. The results of kinetic modelling for the mentioned models are represented in Table 4.1. It can be seen that the linear regression analysis for Korsmeyer-Peppas and Higuchi model are considerably higher than the first order and zero order models. When the fraction of DOX released was plotted against time, according to the first order and zero order models equations, the plots did not present satisfactory linearity, the releasing mechanism was not similar to zero order transport. The results indicated that the release mechanism can be significantly explained by Korsmeyer-Peppas. The value of n which characterizes the release mechanism of drug for all samples are 0.45 ≥ n. This value corresponds to a Fickian diffusion mechanism which in agreement with the results reported in the literature[96, 97].

4.6 In Vitro Cytotoxicity Studies of SWNTs/DOX Complexes

4.6.1 Cytotoxicity studies of pristine long and short SWNTs/DOX

To investigate the cellular uptake of SWNTs loaded with DOX MDBA-MB-231 breast cancer cell line was used. Figures 4.12 and 4.13 shows the cytotoxicity results for DOX-loaded long and short SWNTs.
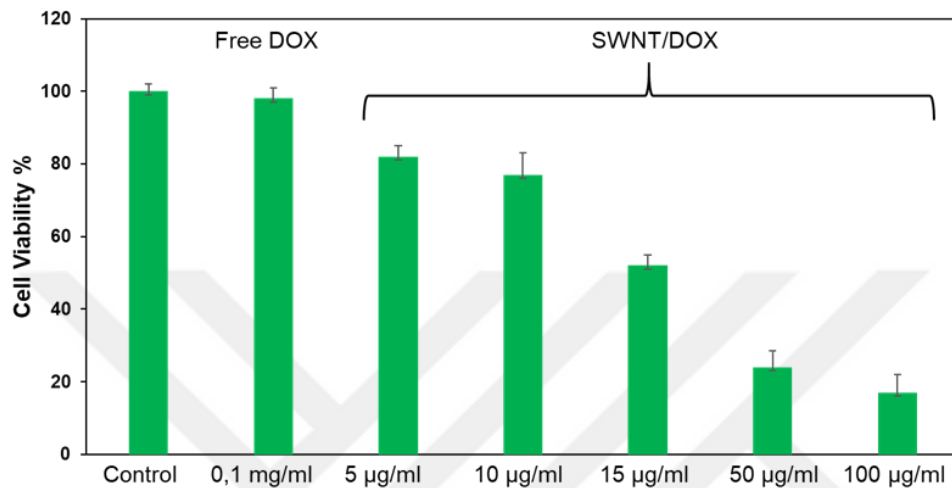
Figure 4.12 : Cell viability results of different concentrations of DOX-loaded short SWNTs in MDA-MB-231 breast (p <0.05).
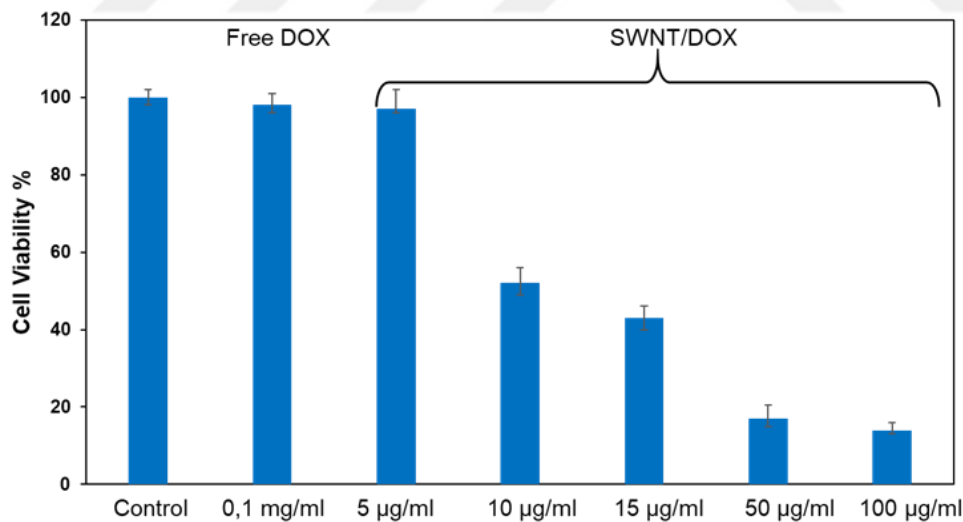
Figure 4.13 : Cell viability results of different concentrations of DOX-loaded long SWNTs in MDA-MB-231 breast (p <0.05).

It can be seen that the intracellular uptake of DOX in SWNTs/DOX systems is higher than free DOX for both short and long SWNTs. Interesting, as the concentration of DOX increases to higher than 5 µg/ml in the SWNTs/DOX construct in both short and long nanotubes, cell viability decreases significantly. Moreover, long SWNTs/DOX

samples exhibited higher cytotoxicity at concentration higher than 5 µg/ml than short SWNTs/DOX. These results demonstrated that pristine SWNTs loaded with DOX molecule could be a very interesting tool to obtain an efficient DOX delivery and extended to enhance the efficiency of cancer therapy in vivo. These findings suggest that drug-loaded SWNTs with desired length exhibit obviously therapeutic eﬀect on cancer cell lines and they become promising strategy in future cancer applications.

4.6.2 In vitro fluorescence imaging results for DOX loaded pristine SWNTs

To explore visually cellular uptake of short and long SWNTs samples, in vitro fluorescence imaging micrographs of the samples were gathered (Figure 4.14).
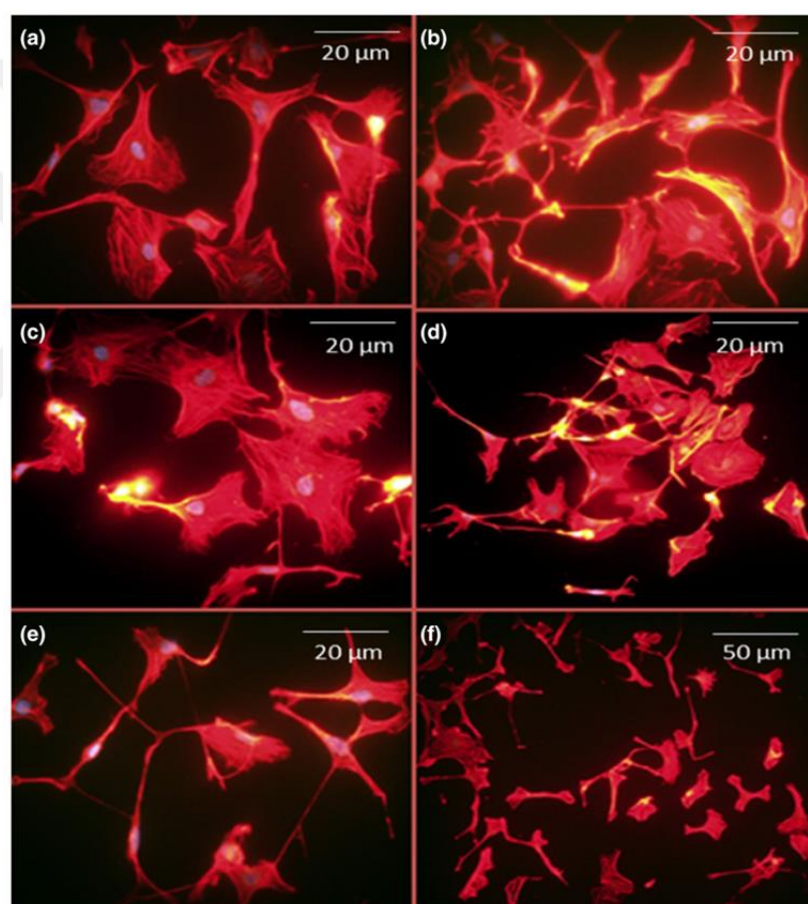
Figure 4.14 : In vitro fluorescence imaging of MDA-MB-231 cells after application of short and long SWNTs. (a) Control group for short SWNTs. (b) Control group for long SWNTs. (c) 10 µg/ml for short SWNTs. (d) 10 µg/ml for long SWNTs. (e) 100 µg/ml for short SWNTs. (f) 100 µg/ml for long CNTs.

The results exhibited that DOX release from short and long SWNTs are significantly high leading to the disruption of actin skeleton of the MDA-MB-231 breast cancer cells.

It is observed that fluorescence microscope images of long SWNTs with high aspect ratio effect were obvious in the samples. It seems that prior to intracellular uptake DOX loaded SWNTs disrupt actin structures of the cancer cells. Similar structural changes were observed at each three repetition of the assay at the same concentrations. The present data demonstrates that pristine short SWNTs may inhibit breast cancer cell line migration by modulating actin cytoskeleton to form a global array of clusters at relatively high concentration 100 µg/ml. Moreover, increasing the concentration of pristine short SWNTs increases disruption of cells proportionally and decreases focal adhesion assembly.

4.6.3 In vitro cytotoxicity studies of PEGylated SWNTs/DOX

Figure 4.15 shows the cell viability of free DOX and DOX-loaded different SWNTs nanocarriers at ~25 µg/ml SWNTs/DOX concentrations toward MDA-MB-231 breast cancer cell lines using MTT and WST-1 methods. While treated with an equivalent concentration of drug, cancer cells exhibited lower viability for DOX-loaded SWNTs and SWNTs/FA than that of PEGylated SWNTs. As expected, FA-conjugated SWNTs exhibited lower cell viability than non-targeted SWNTs due to the hydrophilicity of the PEG chains which bound onto the surface of nanotubes.

Similar results were reported by researchers confirming the sustain release of CNTs when covalent or non-covalent methods were applied to handle the cytotoxicity of these nanostructures [98]. Additionally, low cell viability (<40%) could be achieved only when cancer cell lines treated with DOX-loaded pristine SWNTs/FA (~75 µg/ml DOX). This suggests FA-targeted SWNTs are able to effectively deliver the drug to the intracellular matrix medium due to the efficient cellular internalization of FA-conjugated SWNTs via receptor binding endocytosis.

Selective targeting and delivery of drugs into cancer tissues has become a research hot spot due to the improving the efficacy and minimizing the toxicity of the drug by enhancing its concentration in desired parts of the body [99]. In particular, folic acid (FA) as a ligand for the targeted delivery of drug has been widely used due to the frequently overexpression of folate receptors (FRs) on the surface of numerous cancerous cells [100, 101].

Figure 4.15 : Cell viability results of DOX-loaded short SWNTs in MDA-MB-231 breast (p <0.05).

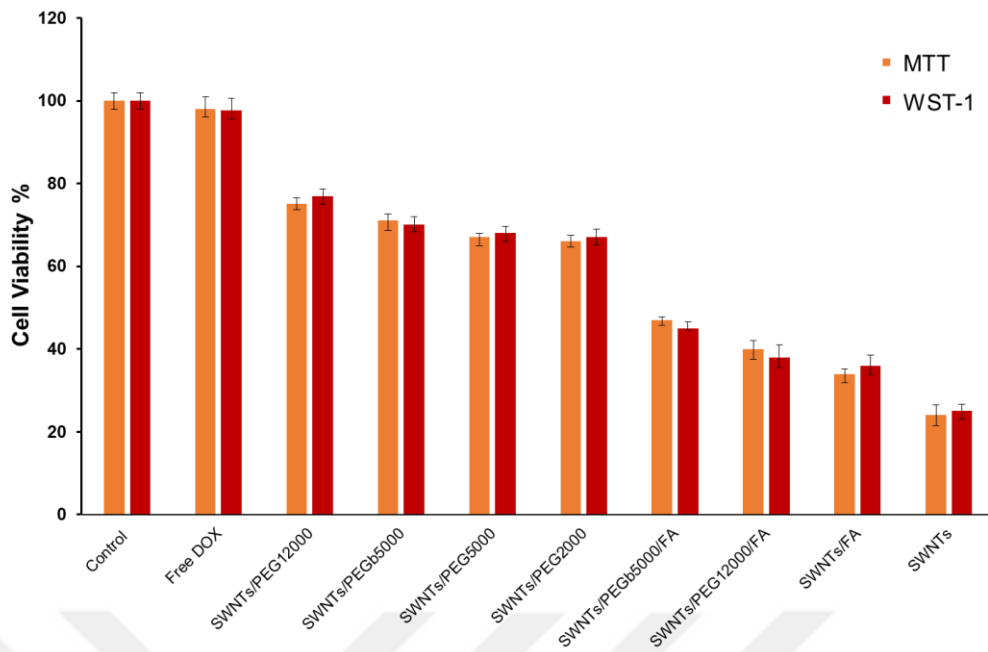Therefore, receptor-targeted delivery plays crucial role in diagnostic and treatment of various types of cancer. The obtained results displayed that PEGylated SWNTs are promising nanocarriers for biomedical applications.

5. EFFECT OF STRUCTURAL DEFECT ON PYRENE COATED SWNTS

In vast majority of the studies that have been conducted regarding CNTs, these nanostructures were considered as perfect arrangement of carbon atoms in aromatic cylindrical settings. However, through the nucleation and growth process[102] and also exposing to the electron irradiation [103] these nanomaterials inescapably hold structural defects. Undoubtedly, the density and site of these structural defects may have substantial impact on their unique physical, chemical electrical and mechanical properties. Therefore, it is very crucial to address this fundamental issue in CNTs with structural defects.

Despite the outstanding promise of non-covalently coated SWNTs for biomedical imaging and molecular therapy applications, a quantitative understanding of structural defects on the non-covalent interactions is lacking. In previous chapters, short and long SWNTs were used in in vitro and in vivo studies. However, it is believed that through the growth and purification phase of the SWNTs production, it is not avoidable to achieve defect-free SWNTs. Consequently, in this chapter, we will investigate the effect of defect bearing SWNTs on van der Waals interaction between nanotubes and pyrene bearing structures. Accordingly, to explore the role of π-stacking interaction in defect bearing SWNTs, molecular dynamics and experimental studies were conducted with a set of hydroxyl and carboxyl functionalized compounds designed to adsorb onto the SWNT sidewalls.

We introduce a multisegment SWNT model consisting of pristine, Stone-Wales defects bearing, and carboxyl functionalized/ Stone-Wales defects bearing SWNTs to theoretically and experimentally explore SWNTs behaviors with structural defects. In the model, the mentioned segments were separately created in Material Studio 8.0 software and each segment of the model was allowed to interact with strongly polar organic groups in aqueous medium.

5.1 SWNTs with Stone-Wales Structural Defects

The rearrangement of two π-bonded carbon atoms in CNTs, fullerenes and graphene creates a crystallographic defect, which is supposed to have important impact on the chemical, electrical, and mechanical properties of these materials. Topological Stone-Wales (SW) defects can be formed by changing the connectivity of C-C bonds in the SWNT sidewall by rotating them 90° as shown in Figure 5.1.
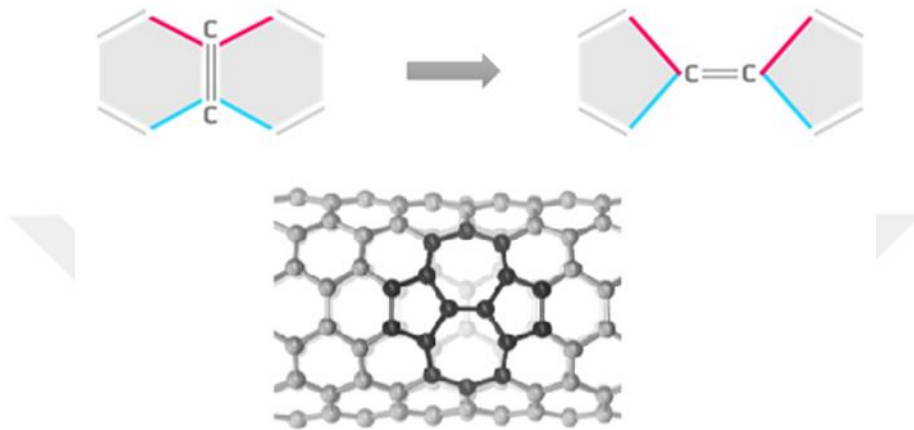
Figure 5.1 : Formation of Stone-Wales (SW) defect by changing the connectivity of C-C bonds.

This rotating leads to the formation of two pentagons connected by two heptagons with a 5-7-7-5 topological defect. Extensive studies on SW type defects have been showed that they have essential role in the structure transition of carbon-based nanostructures, such as the coalescence of carbon nanotubes and fullerenes [104, 105].
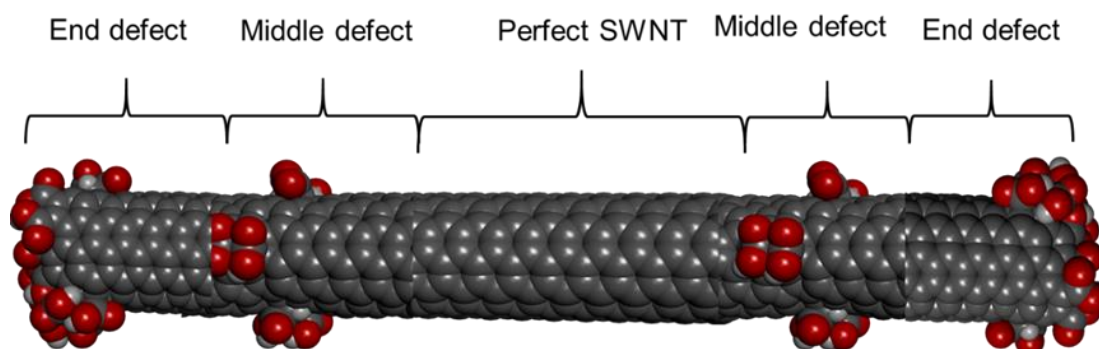
Figure 5.2 : Multisegment SWNT containing there different parts: (a) end defect (b) middle defect and (c) perfect segment.

As represented in figure 5.2, the multisegment SWNT was designed to have three segments as follows: 1) an ideal or perfect pristine SWNT in 2) two Stone-Wales

defects functionalized with carboxylic acid groups at the end wall 3) two Stone-Wales defects functionalized with carboxylic acid groups on the inner sidewall.

5.2 Chemical Structure of Compounds

In order to understand the π-π interaction mechanism between multisegment SWNTs and aromatic anchor-bearing molecules we devised three chemical compounds with different organic functional groups all sharing an aromatic pyrene molecule.

a) Pyr-COOH
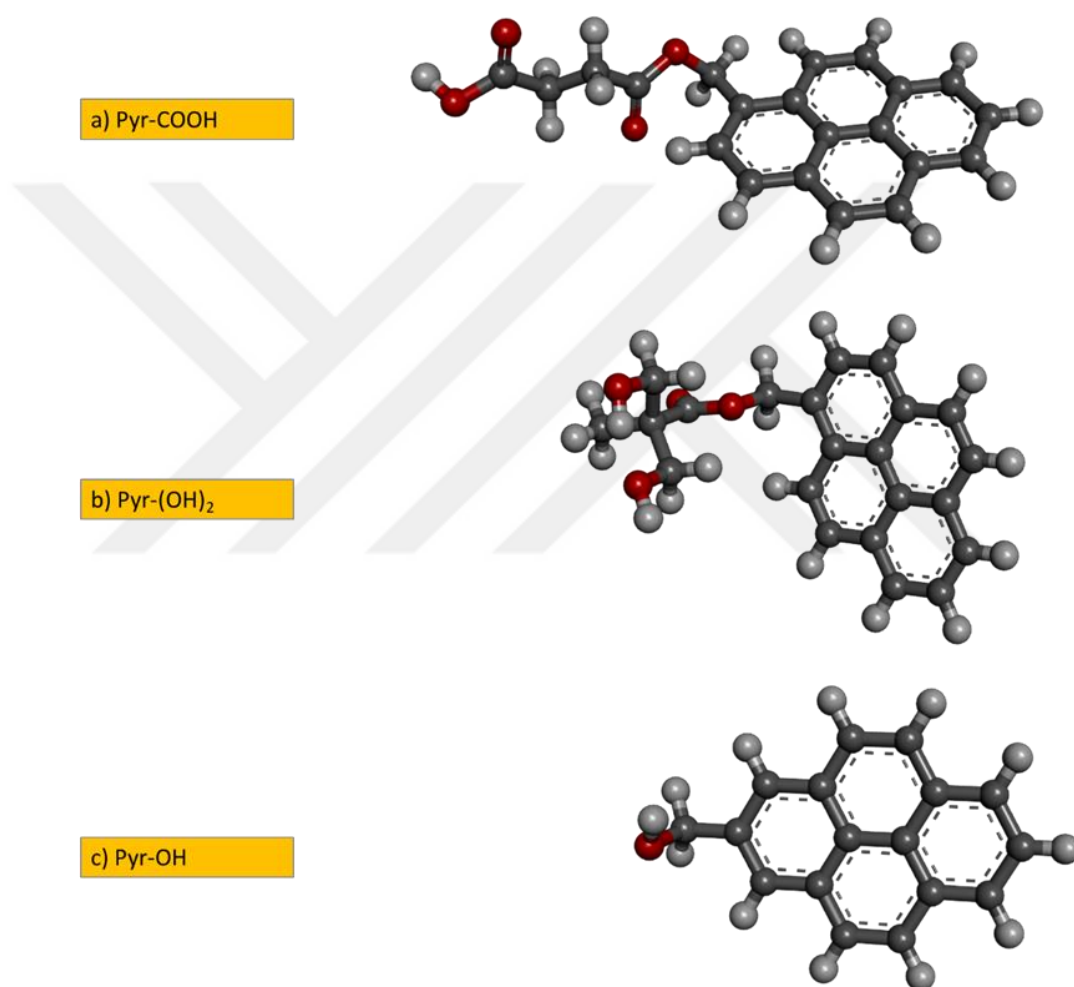
b) Pyr-(OH)$_2$

c) Pyr-OH

Figure 5.3 : Chemical structure of the compounds used for SWNT coating. a) pyr-COOH b) pyr-(OH)$_2$ c) pyr-OH.

As illustrated in Figure 5.3, there different functional groups including –COOH, –(OH)$_2$ and –OH were decided to integrate to the pyrene molecule. Therefore, both in simulation and experimental part, the pyr-COOH, pyr-(OH)$_2$ and pyr-OH were developed for further SWNTs coating. In this chapter, all these compounds will be designated as pyr-X when it is required.

5.3 Computational Results For Ideal Pristine SWNTs

The aromatic structure of four benzene ring in pyrene plays a key role in establishing van der Waals interaction between the generated pyr-X and SWNTs. Due to the hexagonal honeycomb and cylindrical structures of the nanotubes, pyrene anchor of the adsorbents can strongly attach onto the surface of nanotubes via π-π stacking interaction.
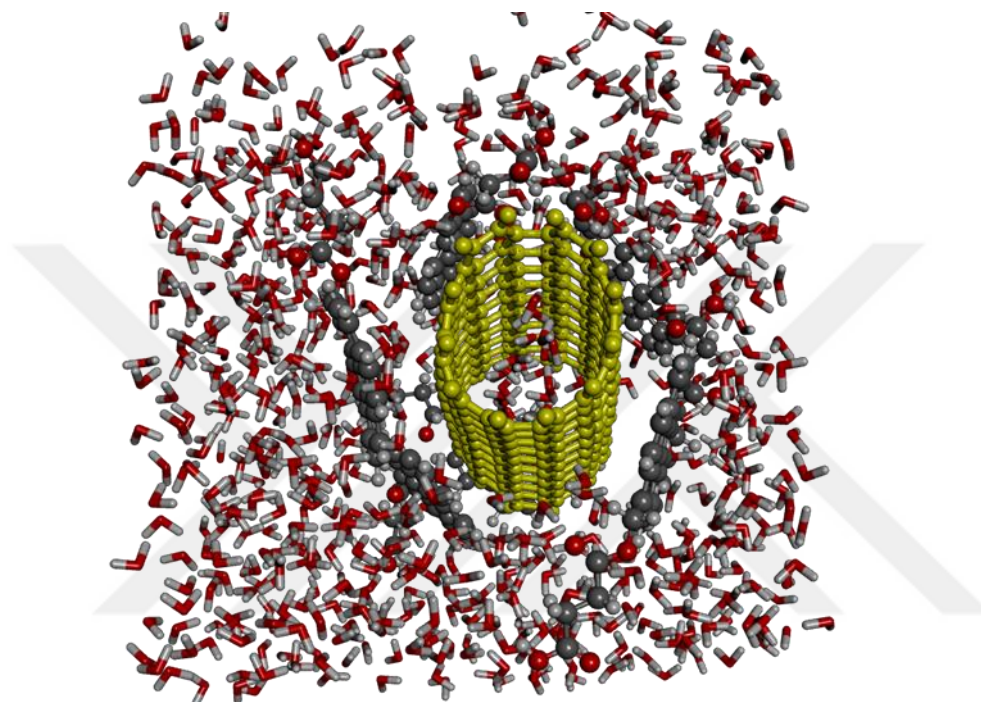
Figure 5.4 : Simulation cubic box and with all the components.

In the first step of the simulation, to generate the system a cubic box was selected to embed all the molecules. The simulation cubic box size was allowed to be 30×30×30 Å (Figure 5.4). Prior to the generation of the system, several adsorption annealing processes were carried out to gain information regarding the number of pyr-X molecules that cover the SWNT surface. It was observed that once the number of Pyr-X in the system was chosen to be seven, the successful coverage of the SWNTs surface can be obtained. Thereafter, the system was built with seven pyr-X molecules and one SWNT with water medium. It is worthy to note that all the components were experienced energy minimization prior to system construction.

The MD simulation time was allowed to be 5 ns for each run. As mentioned in Computational Methods, COMPASS forcefiled was utilized in each MD run. To calculate the amount of interaction energy, each MD trajectory output files was used

as input files for further 1 ns quenched MD simulation runs. Likewise, COMPASS forcefiled was employed for binding energy calculation in Quench.

In order to measure π-π interaction strength between SWNTs and pyrene-X structures the following interaction energy E_{BE} (kcal/mol) equation 5.1 is introduced.

$$E_{BE} = E_{complex} - (E_{SWNT} + E_{Pyr-X})$$ (5.1)

Here, $E_{complex}$ is the total energy of the Pyr-X adsorbed on SWNT, E_{SWNT} is the total energy of the SWNT without pyr-X and $E_{pyr-PEG}$ total energy of the pyr-X without the nanotube.

The average amount of Interaction energies E_{BE} (kcal/mol) per one pyr-X for perfect SWNTs coated with pyr-X are displayed in Table 5.1.

Table 5.1 : Average interaction energies E_{BE} (kcal/mol) per one pyr-X for SWNT/pyr-X systems.

Model	Ideal SWNT E_{BE} (kcal/mol)
pyr-COOH	-28.3
pyr-(OH)₂	-23.3
pyr-OH	-20.4

As it can be seen, the average amount of interaction energy for pyr-X are all in the same order of magnitude. There is, however, an increase in the interaction energy of pyr-COOH. It seems that as the polarity of the functional group in the pyr-X structure increases, there is a positive effect on the amount of interaction energy between Pyr-X and SWNTs. In terms of pyr-COOH, this increase might be attributed in part to the reorientation of pyr-COOH molecules on SWNT sidewall upon interacting with the water molecules.

In order to gain insight into hydrogen bond strength between Pyr-X and water molecules, radial distribution function (RDF) was used. The probability of finding a particle in a shell dr at the distance r of another particle represents the radial distribution function, g(r).

$$g(r) = \frac{1}{4\pi Nr^2 \rho_0} \sum_{j=1}^{N} \sum_{\substack{i=1 \\ i \neq j}}^{N} \delta(r - r_{ij}) = \frac{1}{2\pi Nr^2 \rho_0} \sum_{j=1}^{N} \sum_{i>j}^{N} \delta(r - r_{ij})$$ (5.2)

In this equation, ρ is the number density, N is the set of number of molecules, δ is the Kronecker delta, and ri is the position vector of molecule i. To measure the amount of H-bond for Pyr-X molecules, we first calculate g(r) function for every pyr-COOH, pyr-(OH)$_2$ and pyr-OH in each system (Figure 5.5). As expected, hydrogen bond strength between the H atom of the carboxyl group of pyr-COOH and water molecules are considerably higher than the other pair groups. A comparison between H-bond interaction between different polar atom with water molecules are presented in Figure 5. 5. Similar to the results of the RDF for pyr-COOH, the magnitude of hydrogen bond between hydroxyl groups of pyr-(OH)$_2$ and water molecules are significantly higher than the other pairs. Therefore, the mentioned pairs were considered in further comparisons.
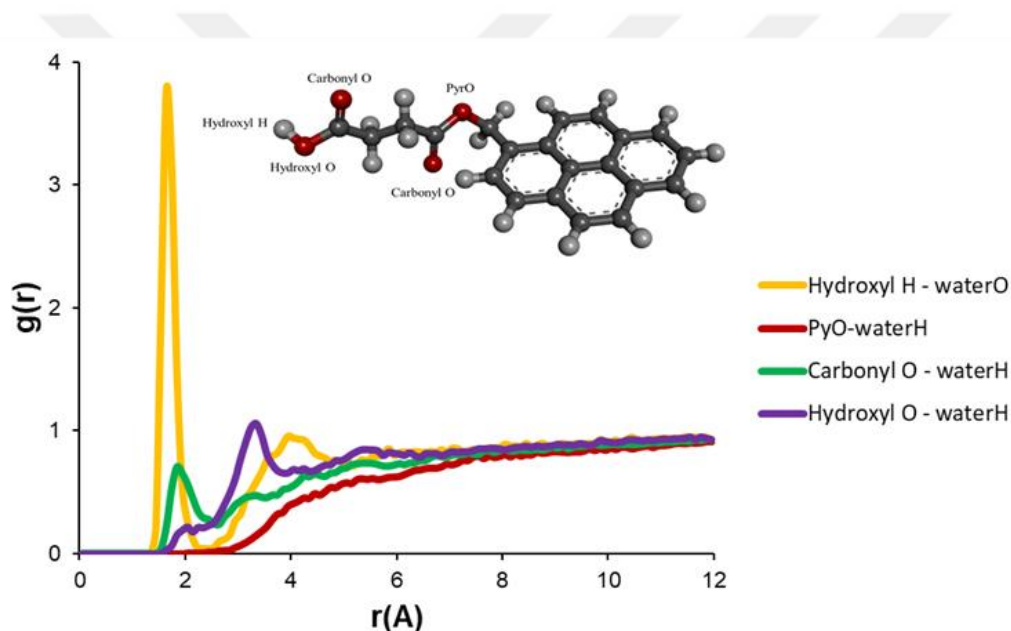
Figure 5.5 : Hydrogen bond between the different atoms of the carboxyl group of pyr-COOH and water molecules.

The amount of H-bond strength for pyr-X compounds are presented in Figure 5.6. The existence of –COOH group in SWNT/pyr-COOH system led to efficient H-bond interaction between water molecules and hydrogen atom of the carboxyl group.

Consequently, establishment of strong H-bond interaction in SWNT/pyr-COOH system with respect to the SWNT/pyr-(OH)$_2$ and SWNT/pyr-OH may handle SWNT/pyr-COOH dispersion in aqueous mediums.
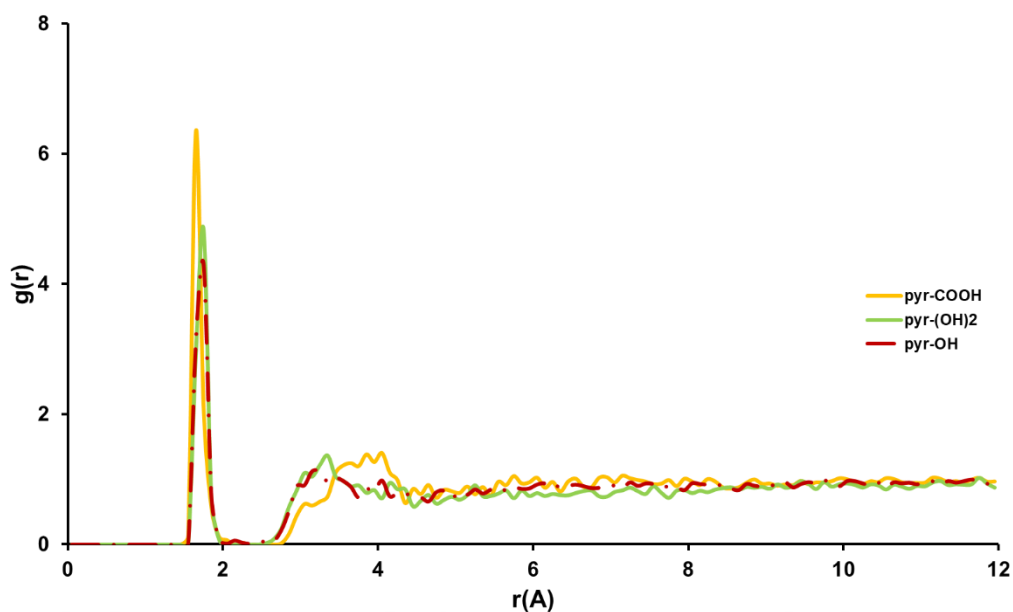
Figure 5.6 : Hydrogen bond between SWNT/pyr-X and water molecules.

In the case of SWNT/Pyr-(OH)$_2$ and SWNT/pyr-OH, such strong H-bond interaction was not occurred. This observation can be ascribed to the lower polarity of –OH group with respect to –COOH group.
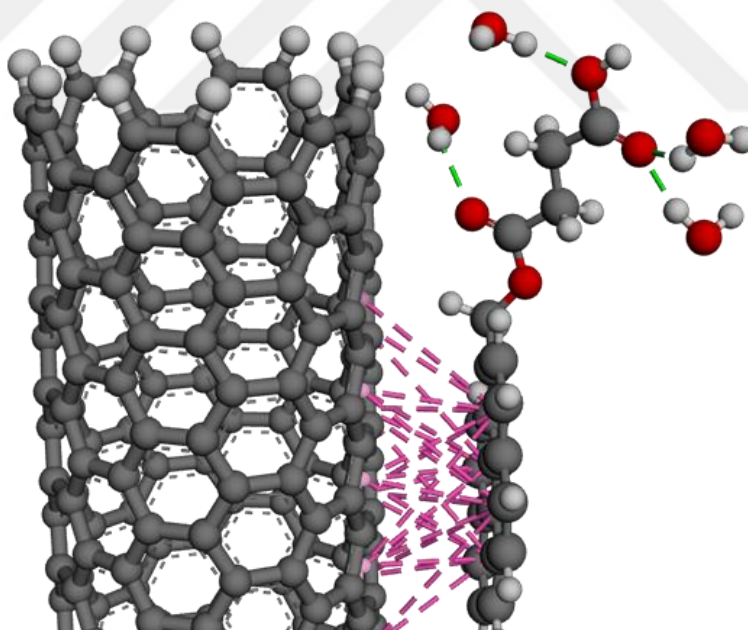
Figure 5.7 : Representation of π-π and hydrogen-bonded interactions in the system.

It is believed that there is competing interaction between π-π interactions and hydrogen-bonded interactions. The schematic π-π interactions and hydrogen-bonded interactions for a pyr-COOH are illustrated in Figure 5.7. If H-bonded interactions are extremely strong enough it can be assumed that pyr-X structures have the possibility to detach from the SWNTs sidewall. In the case of perfect SWNTs, due to the

establishment of strong π-π stacking interactions between pyr-X and SWNTs, it is not expected to observe such detachment for all three pyr-X. To further examine this competing interaction between π-π stacking interactions and hydrogen-bonded interactions and their impact on the configuration of pyr-X on the SWNTs surface, structural Stone-Wales defects were introduced to the SWNTs.

5.4 Computational Results For Defect Bearing SWNTs

Early theoretical study [106] has shown that perfect SWNTs as quasi one-dimensional nanostructures exhibit unique physicochemical, electrical and mechanical properties which arise from their diameter and chirality. However, these nanostructures are probably not perfect because the growth mechanism of SWNTs are still not sufficiently well understood. Therefore, various defects such as pentagons, heptagons, vacancies, can be readily formed which lead to drastically changes in the properties of these nanosystems.
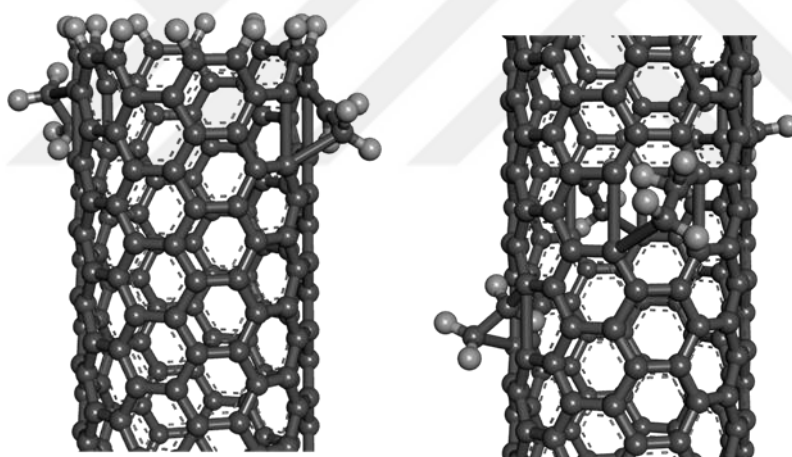
Figure 5.8 : Four Stone-Wales defects at the end (left) and middle (right) of each SWNTs.

In this part, we built two distinct SWNTs with end and middle defects. The topological stone-wales defects of the SWNTs are shown in the Figure 5.8. Two pentagons and two heptagons created in each SWNT. In SWNTs with end defects, these pentagons and heptagons were placed near to the end cap of SWNTs. It is aimed to assess the effect of these end defects on the strength of π-π stacking interactions. Another SWNT with middle defects containing similar pentagons and heptagons were built in the middle of the SWNT side wall. These two nanotubes were created to explore and compare the amount of binding strength and possible detachment of Pyr-X from the

surface of SWNT. The adsorption position of the seven pyr-COOH for SWNTs with end and middle defects at the beginning and the end of the MD runs are presented in Figure 5.9 and 5.10 respectively.
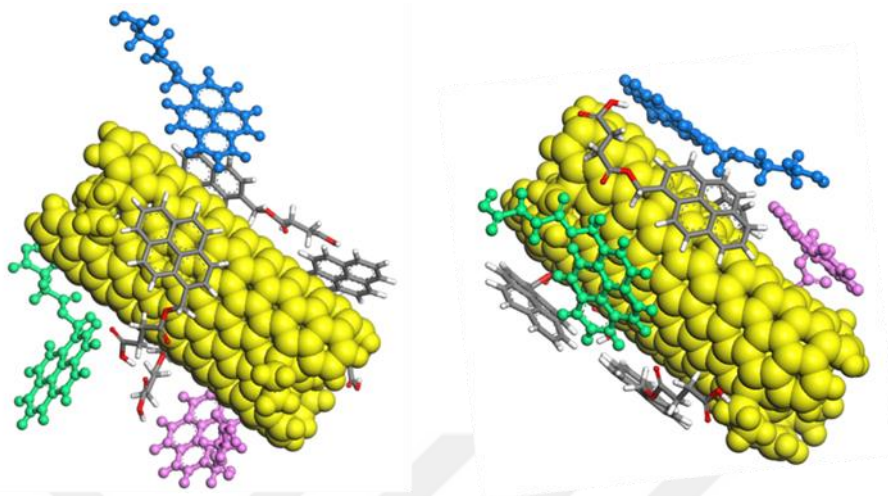
Figure 5.9 : Adsorption position of the pyr-COOH on the sidewall of SWNTs with end defects at the beginning (left) and end (right) of the MD run.

It can be seen from the Figure 5.9 that there is no stacking of pyr-COOH on each other once SWNT with end defect was utilized. However, the existence of middle defects in SWNT result in stacking of pyr-COOH on each other. The may be due to the fact that the local aromaticity of the SWNTs side wall in these points declined drastically.
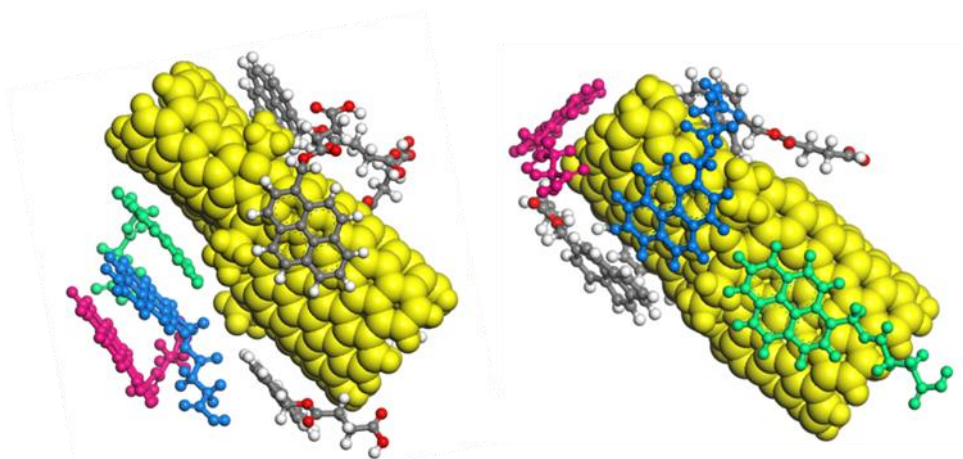
Figure 5.10 : Adsorption position of the pyr-COOH on the sidewall of SWNTs with middle defects at the beginning (left) and end (right) of the MD run.

Although, for SWNTs with end defect the aromatic behavior of that local site disrupted, however, the settlement of these Stone-Wales defect near to the end cap would not significantly affect the interaction between SWNT and pyr-X complex. Interesting, the pyr-COOH stacking in SWNTs with middle defects disappeared near

to the middle of the MD run and all pyr-COOH molecules directly attached to the SWNTs sidewall. Therefore, it seems that although middle defects on SWNT rigorously changes the configuration of the pyr-COOH on the SWNT side wall but, by giving the required time these pyr-COOH tends to displace and attach directly to SWNT surface. Moreover, no detachment happened for pyr-COOH on SWNTs with end and middle defects. In the case of pyr-(OH)$_2$ and pyr-OH, no stacking was observed at the beginning of simulation. MD simulation results revealed that reorientation of pyr-COOH groups on the SWNT surface were higher than that of pyr-(OH)$_2$ and pyr-OH.

It can be said that displacement of pyr-COOH on the surface of SWNT might be due to the strong H-bond interaction with water molecules and weak π-π interaction with SWNT. The interaction energy E_{BE} (kcal/mol) calculation for pyr-X on SWNTs with end and middle defects are displayed on table 5.2.

Table 5.2 : Interaction energies E_{BE} (kcal/mol) per one pyr-X for SWNT/pyr-X systems.

Model	Ideal SWNT
	E_{BE} (kcal/mol)
pyr-COOH	-24.3
pyr-(OH)$_2$	-23.3
pyr-OH	-21.1

It is noteworthy to mention that the equal conditions were employed in MD simulation to calculate the interaction energies. The similar range was acquired for defect bearing SWNTs as for perfect SWNTs.

These results revealed that despite the presence of defects, π-π interaction between pyr-X and SWNTs are strong enough. However, the presence of Stone-Wales defects on SWNTs surface led to continuous reorientation of pyr-X on the SWNTs surface especially in middle defects bearing SWNTs.

It can be said the observed continuous reorientation is due to the weaker π-π interaction with respect to defect-free SWNTs. The radial distribution function g(r) calculation for the models are illustrated in Figure 5. 11.
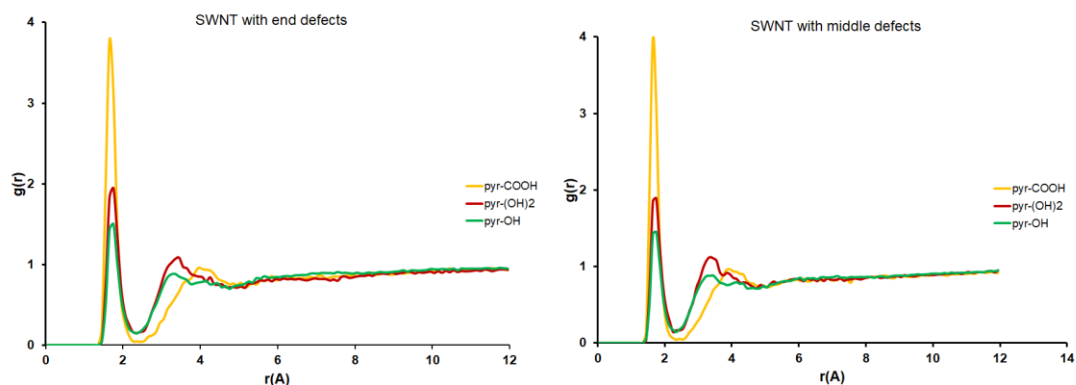
Figure 5.11 : Radial distribution function (RDF) for the pyr-X with end and middle defect bearing SWNTs.

The amount of RDF for pyr-COOH is significantly higher than that of pyr-$(OH)_2$ and pyr-OH for both end-defected and middle-defected SWNTs. There is no noticeable difference between pyr-$(OH)_2$ and pyr-OH. These results are in agreement with that obtained for defect-free SWNTs revealing that no huge changes take place in Interaction energy and radial distribution function of both SWNTs coated with Pyr-X.

5.5 Computational Results For Defect Bearing SWNTs Functionalized with – COOH Groups

Heretofore, we investigate defect-free SWNTs and SWNTs bearing middle and end Stone-Wales defects. However, studies revealed that in the production or purification phase of SWNTs, various functional groups such as –OH, –COOH, –COH and –CO can be formed on SWNTs side walls particularly at the end caps of SWNTs [107–109].
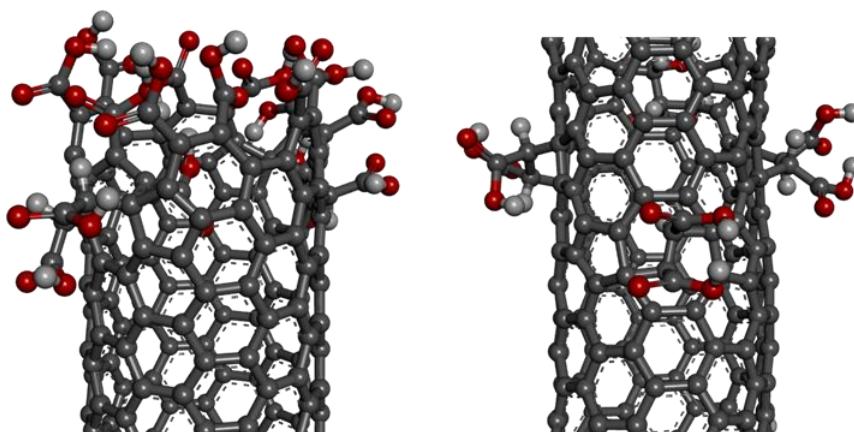
Figure 5.12 : Four Stone-Wales defects at the end (left) and in the middle (right) of SWNTs.

To mimic such alteration on the SWNT structure, –COOH groups along with topological Stone-Wales defects were created on SWNTs surface and MD simulations repeated for these structures with the same pyr-X. The illustration of these structures are given in Figure 5.12. It is better to note that the end caps of SWNTs with middle defects were also functionalized with –COOH groups. Additionally, –COOH was added to the end and middle defects of both SWNTs.There are no significant changes in Interaction energy of the Pyr-X molecules for both end and middle bearing defects SWNTs (Figure 5.11). However, for SWNTs coated with pyr-COOH detachment took place after 1 ns.
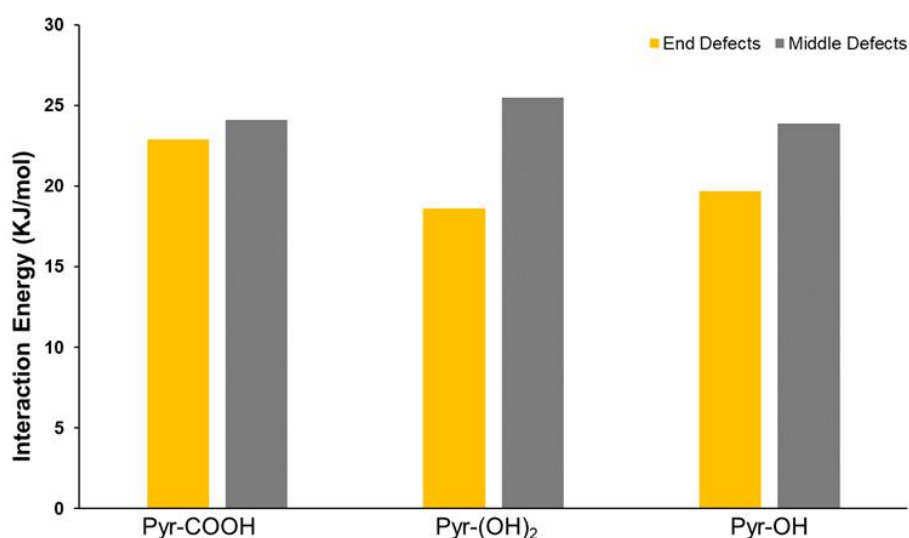
Figure 5.13 : Interaction energies of the pyr-X molecules for both end and middle bearing defects SWNTs.
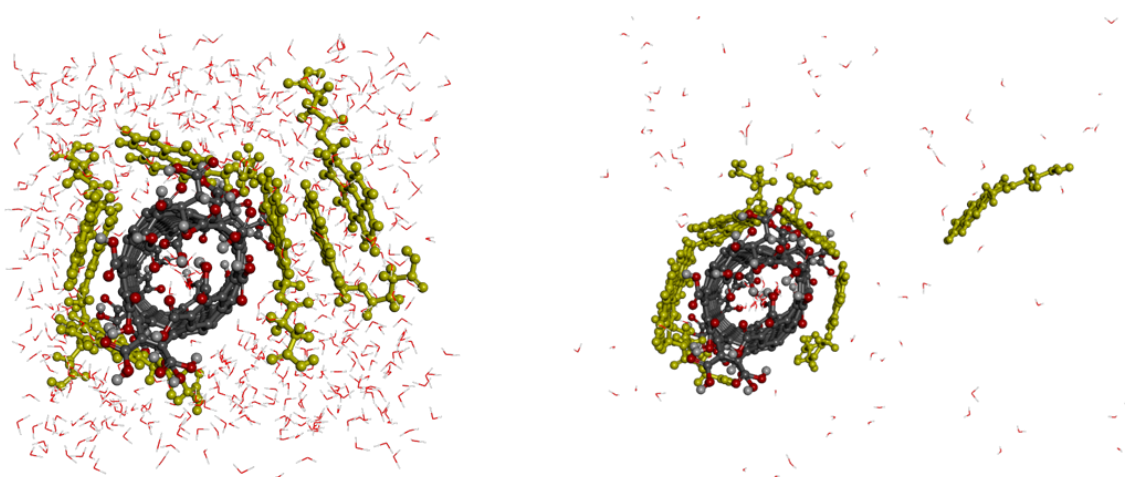
Figure 5.14 : Adsorption position of the pyr-COOH on the sidewall of SWNTs with end defects at the beginning (left) and end (right) of the MD run.

Figure 5. 14 and 5.15 illustrates the pyr-COOH adsorption position on SWNTs with end and middle defects before and after the MD runs respectively. It can be observed that one of the pyr-COOH molecules in SWNTs with end defects and two of the pyr-COOH in SWNTs with middle defects disconnected from the SWNTs sidewall at the end of MD run.
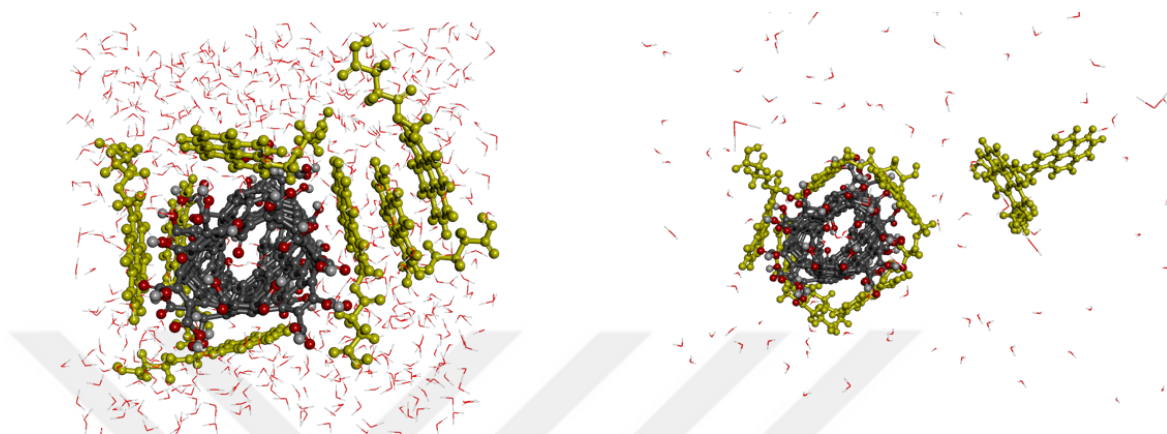
Figure 5.15 : Adsorption position of the pyr-COOH on the sidewall of SWNTs with middle defects at the beginning (left) and end (right) of the MD run.

This detachment of pyrene bearing molecule from the SWNTs surface have not been reported before. This incident might be due to competing interactions between hydrogen bond and π-stacking. The presence of –COOH functionalized Stone-Wales defects provide steric hindrance for pyrene bearing molecules to efficiently establish π-π stacking interaction with SWNTs. On the other hand, in these sites, the aromaticity of the SWNTs dramatically diminished. Therefore, the SWNTs cannot afford all seven pyr-COOH on its surface. Moreover, formation of strong H-bond with water molecules, Pyr-COOH molecules tend to be dispersed in the solvent.

As it can be seen from figure 5.13, the presence of topological Stone-Wales defects in the middle part of the SWNTs led to higher detachment with respect to SWNTs with end defects. This behavior can be associated to the drastic reduction in aromaticity of the SWNTs side wall.

The radial distribution function calculation for pyr-X molecules in water are given in Figure 5.16. A substantial increase in the amounts of g(r) function for all of pyr-X were obtained. This markedly increase can be associated to incorporation of the – COOH groups on the SWNTs end caps and at the defect sites. The carboxylic acid groups built up H-bonds with water molecules and this increase the density of the water

molecules adjacent to the pyr-X which leads to effective interaction with these molecules.
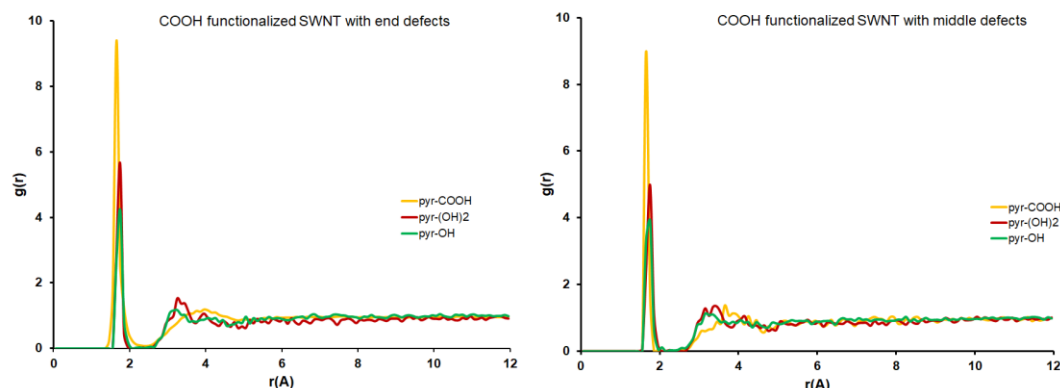
Figure 5.16 : Radial distribution function calculation for Pyr-X in water system.

These MD simulation results illustrate a noncovalent functionalization scheme for multisegment SWNTs and reveal how one could tailor the coating of SWNTs by judicious choice of Stone-Wales defects. The study also helps in building a quantitative understanding of non-covalent coating of SWNTs using pyrene as anchor molecule. As mentioned previously, through the production and purification process, both functional groups and defect can be generated in nanotubes. Recent studies (ref 12-16) revealed that hydroxyl, carboxyl and other functional groups tend to be formed at the end caps due to the existence of carbon with single bond at these sites. Moreover, the presence of defects on side walls of SWNTs provide such carbon atom to be functionalized with hydroxyl, carboxyl groups. Therefore, based on the results of computational studies we used SWNTs purified using nitric acid treatment in order to mimic the behavior of multisegment SWNT coated with pyr-COOH, pyr-(OH)$_2$ and pyr-OH molecules.

This detachment of pyrene bearing molecule from the SWNTs surface have not been reported before. This incident might be due to competing interactions between hydrogen bond and π-stacking. The presence of –COOH functionalized Stone-Wales defects provide steric hindrance for pyrene bearing molecules to efficiently establish π-π stacking interaction with SWNTs. On the other hand, in these sites, the aromaticity of the SWNTs dramatically diminished. Therefore, the SWNTs cannot afford all seven pyr-COOH on its surface. Moreover, formation of strong H-bond with water molecules, pyr-COOH molecules tend to be dispersed in the solvent.

5.6 Synthesis of Pyr-COOH, Pyr-(OH)₂ and Pyr-OH

Similar to simulation part of the study, we prepared pyr-COOH, pyr-(OH)₂ and pyr-OH. Pyrene methanol (pyr-OH) was used as starting point in synthesizing of both pyr-COOH and pyr-(OH)₂. To obtain pyr-COOH, Pyr-OH was treated with succinic anhydride in the conditions mentioned in the experimental part. In the case of Pyr-(OH)₂, acid ketal was used as start point and treated with pyr-OH to achieve pyrene diol (Pyr-(OH)₂). After synthesizing of pyr-COOH and pyr-(OH)₂, ^{1}HNMR measurements (Figure 5.17) confirmed the formation of the compounds.
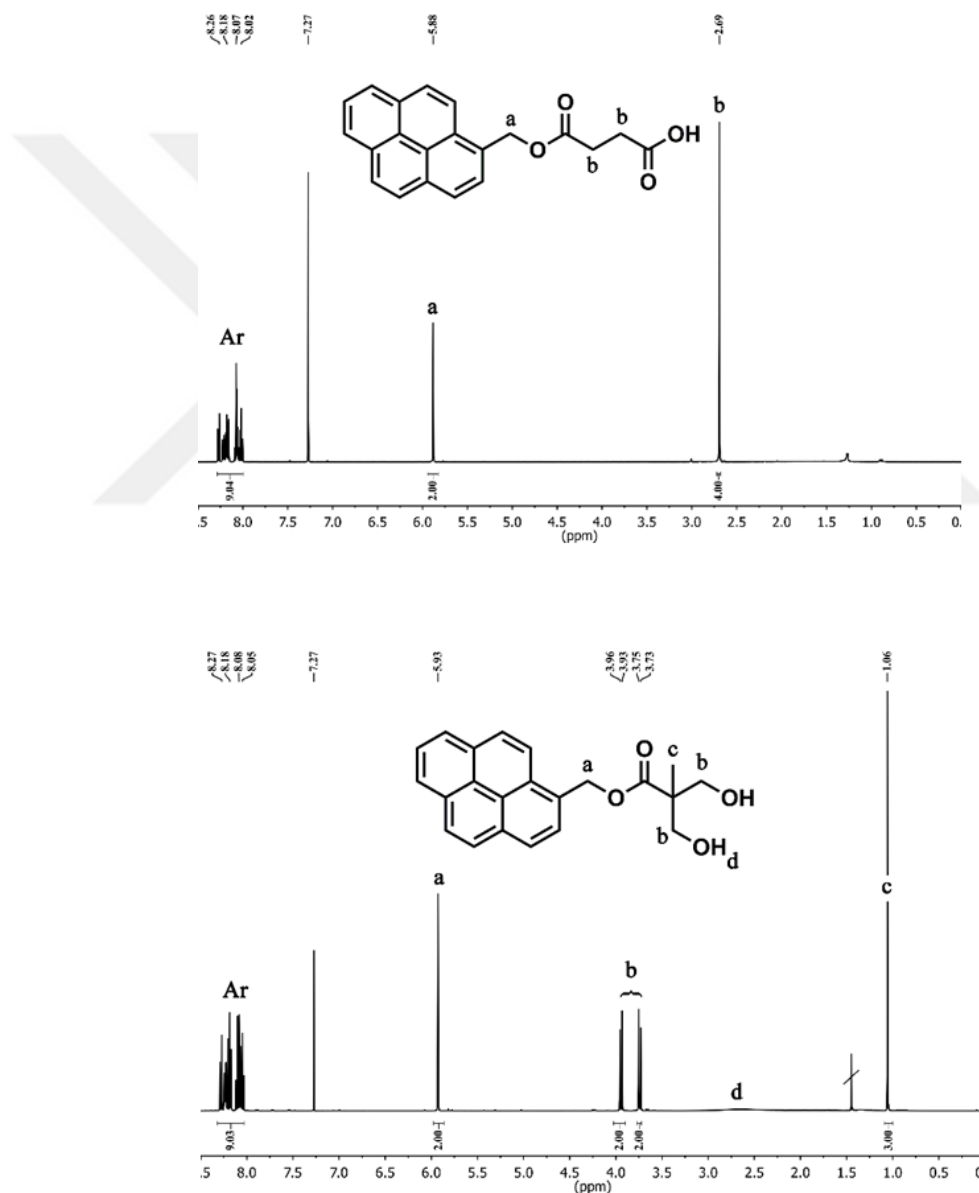
Figure 5.17 : [1]NMR spectrum of of pyr-COOH and pyr-(OH)₂.

As it can be seen from Figure 5.17, the signal attributed to the pyrene (δ = 8–9.2 ppm, ArH) appeared in both measurements. The ^{1}HNMR measurement for pyr-COOH also

exhibit the signals for –CH$_2$ groups of succinic anhydrate at δ = 2 ppm. Besides, the signals for –CH$_2$ (δ = 6 ppm) bound to the aromatic pyrene group and –CH$_2$ (δ = 3.5– 4 ppm) attached to the hydroxyl groups of pyr-(OH)$_2$ compound are all depicted in Figure 5.17. The synthesized pyr-X compounds were then used to non-covalently coat SWNTs in next step. Fluorescence spectroscopy was used to characterize pyr-X coated SWNTs. Fluorescence emission spectra of pyr-COOH, pyr-(OH)$_2$ and pyr-OH at 375 nm excitation wavelength are illustrated in Figure 5.18 to 5.20. The characteristic fluorescence peak of pyrene anchor of the pyr-X compounds were appeared at 375 excitation wavelength, however, after the incorporation of pyr-X to SWNTs, these peaks were completely disappeared. This behavior of pyrene molecule is due to the quenching of pyrene excitation after establishment of π-π stacking interaction with SWNTs and was confirmed by previous studies[27, 74, 110]. This results verify that the pyrene anchor of pyr-X directly interacted with the nanotubes surface as expected. Accordingly, both fluorescence spectroscopy and ^{1}HNMR measurements demonstrated successful formation of the SWNT/pyr-X nanostructures.
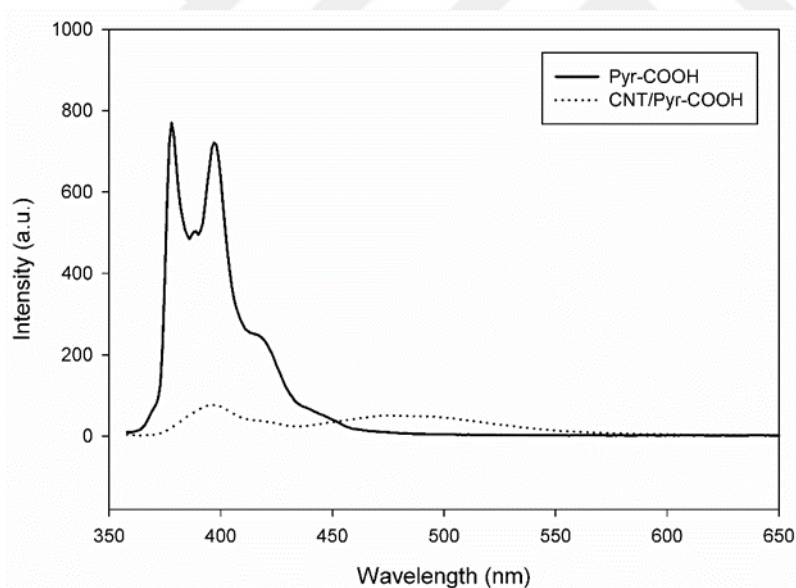
Figure 5.18 : Fluorescence emission spectra of pyr-COOH and SWNT/pyr-COOH at 375 nm excitation wavelength.

To gain a quantitative insight into the relative amount of the incorporated pyr-X on the SWNTs surface, thermogravimetric analysis (TGA) were carried out. As it can be seen from the Figure 5. 21 the decomposition temperature of the pyrene for all of the Pyr-X appeared between 350-450 °C [74]. The amount of weight loss for pristine SWNT and SWNTs coated with pyr-X are shown in Figure 5. 22. The weight loss observed

for pristine SWNT may be due to the carbon impurities such as amorphous carbon in the sample.
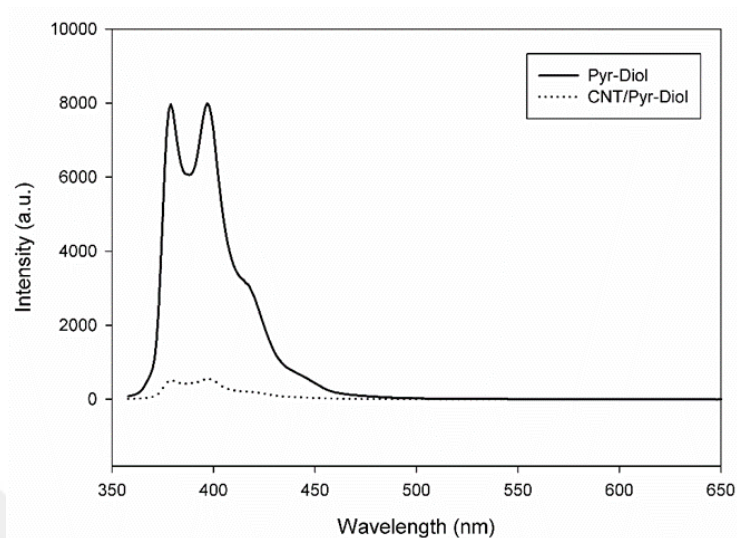
Figure 5.19 : Fluorescence emission spectra of pyr-Diol and SWNT/pyr-Diol at 375 nm excitation wavelength.

To gain a quantitative insight into the relative amount of the incorporated pyr-X on the SWNTs surface, thermogravimetric analysis (TGA) were carried out. As it can be seen from the Figure 5. 21, the decomposition temperature of the pyrene for all of the pyr-X appeared between 350-450 ℃ [74]. The amount of weight loss for pristine SWNT and SWNTs coated with pyr-X are shown in Figure 5. 21. The weight loss observed for pristine SWNT may be due to the carbon impurities such as amorphous carbon in the sample.
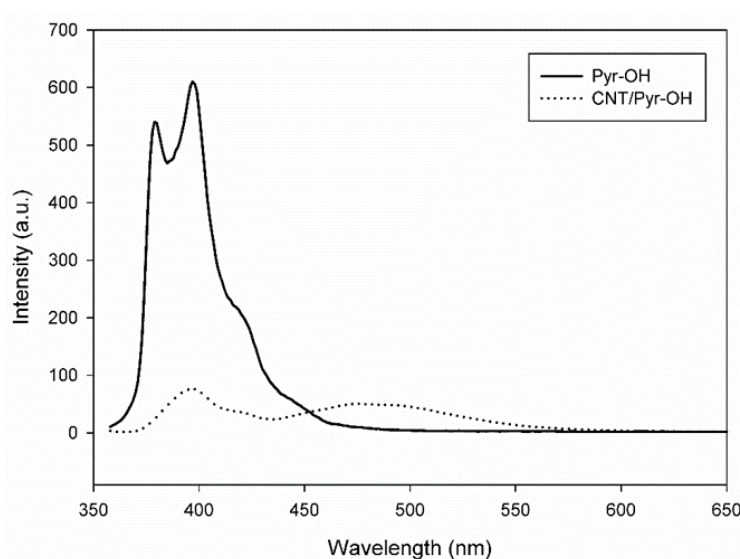
Figure 5.20 : Fluorescence emission spectra of pyr-OH and SWNT/pyr-OH at 375 nm excitation wavelength.

All Thermogravimetric curves for pyr-X coated SWNTs displayed similar trend with the weight loss amount between ~13-22 %. Interestingly, pyr-COOH exhibited higher weigh loss with respect to the pyr-$(OH)_2$ and pyr-OH. This may be attributed in part to higher attachment of pyr-COOH to the SWNTs because of its strong polar group which leads to smoothly gain mobility in the solvent.
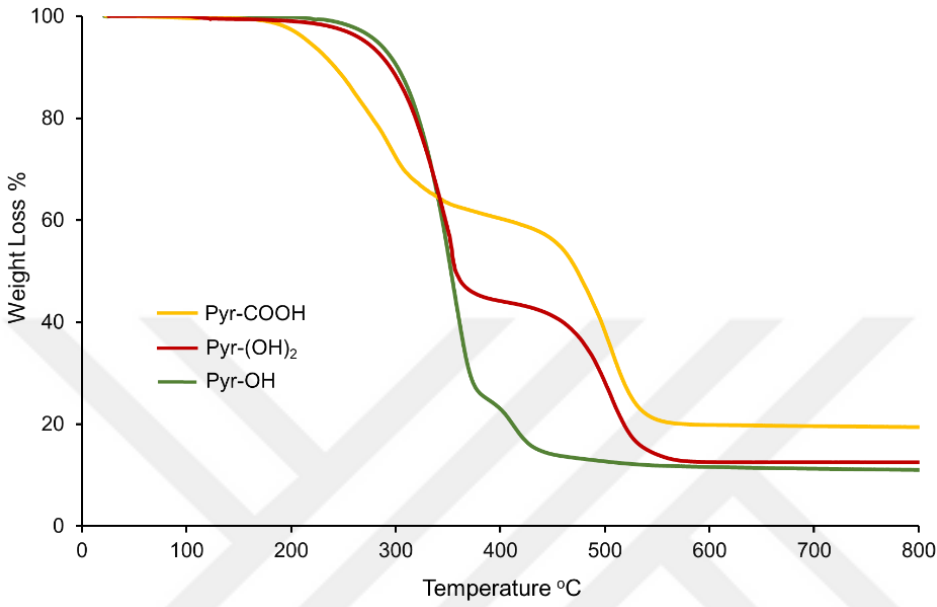
Figure 5.21 : Thermogravimetric analysis for pyr-COOH, pyr-$(OH)_2$ and pyr-OH.
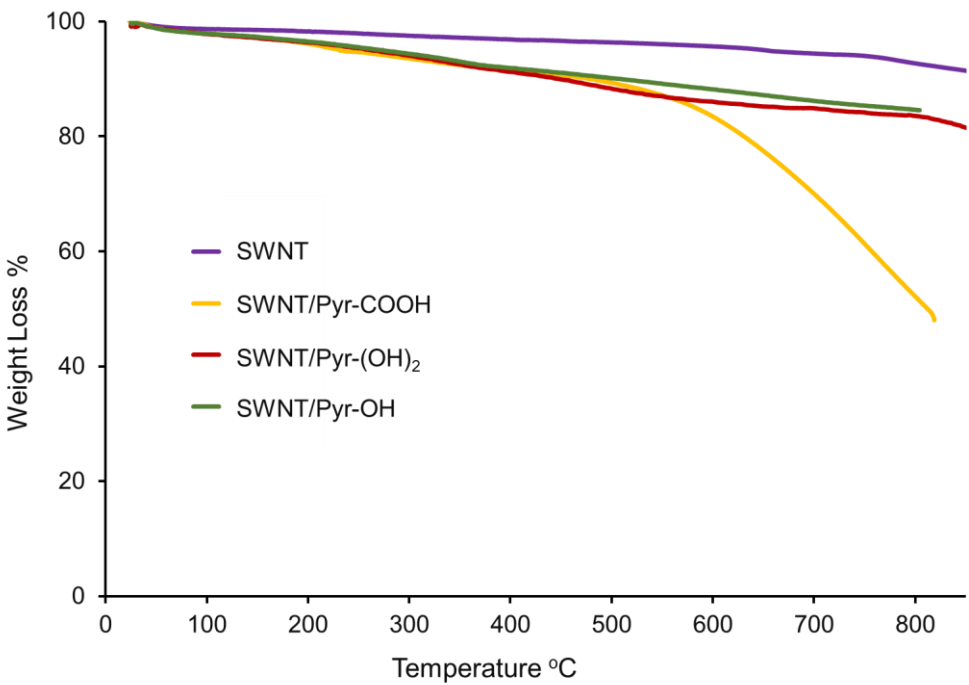
Figure 5.22 : Thermogravimetric analysis for SWNTs coated with pyr-X.

To gain visual insight into the dispersion of the pyr-X coated SWNTs, the dispersion of the SWNTs in distilled water at t=0, 1,3,5 h time intervals was photographed (Figure 5.21).
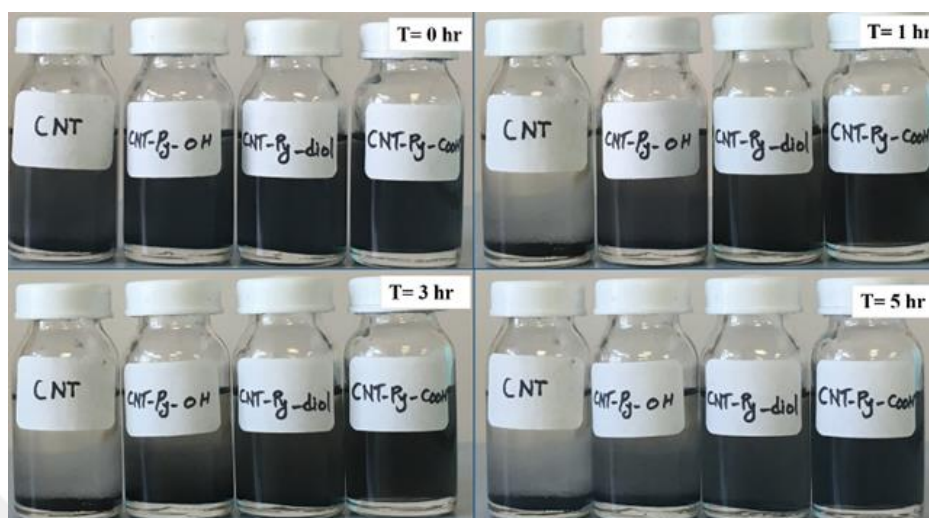
Figure 5.23 : Dispersion images of the pyr-X coated SWNTs in distilled water.

To gain visual insight into the dispersion of the pyr-X coated SWNTs, the dispersion of the SWNTs in distilled water at t=0, 1,3,5 h time intervals was photographed (Figure 5.21). The results clearly displayed that the SWNTs were successfully dispersed in the distilled water after 1 hour. It can be seen that precipitation of the SWNTs coated with pyr-OH and pyr-$(OH)_2$ were taken place as time progressed. This can be explained via lower H-bond formation between with Pyr-OH and pyr-$(OH)_2$ and water molecules. In the case of SWNTs coated with pyr-COOH, the solution is completely homogeneous after 5 hours.

6. CONCLUSIONS AND RECOMMENDATIONS

An approach was utilized to devise a biocompatible PEG-coated SWNT nanocarrier for further drug delivery studies. We first fabricated noncovalent assembly of SWNTs bearing PEG was synthesized by using pyrene as an anchor. Two types of SWNT with different length were functionalized by incorporation of different pyr-PEGs (PEG_{2000}, PEG_{5000}, PEG_{12000} branched PEG_{5000}). Cell viability results revealed that short SWNT enhanced cell proliferation, however, long SWNT had inhibitive behavior. Longer PEG chains provided lower cytotoxicity of SWNTs and higher biocompatibility to the endothelial cells lines (HUVEC). In vivo blood circulation time study on mice revealded the fabricated PEGylated short SWNTs have obtained biocompatibility, with substantial biocompatility from branched PEG. Further Folic acid introduced the SWNTs and DOX as anticancer drug was loaded to the fabricated nanocarriers. The loading results at different pH indicated that at basic pH values, higher amount of loading can be obtained. Release performance from the nanocarriers exhibited that at acid pH 5.5 FA-conjugated nanocarriers have higher relase rate with respect to nontargeted nanoccaries. Finally, MD simulation results along with experimental results showed that the defect bearing SWNTs although can provide lower π-π stacking interaction at the defect site however, if the site of the defects is located near to the end caps it would not severly affect the amount of hydrophobic interaction. The present study indicated that effectively PEGylated short SWNT system provides a promising platform not only for cellular imaging but also for therapeutic purposes in the treatment of different types of cancerogenic tissues.

As recommendation, the length and type of the SWNTs can be considered for further studies. In this study, it was showed that, the length of nanotubes plays important role on their biocompatibility. Therefore, an optimization of SWNTs length and also on its chirality may provide deeper insight into the structure of these nanocarriers. To gain in depth insight to the receptor targeted SWNTs, in vivo studie would also provide valuable information about the fabricated SWNTs/PEG/FA/DOX nanocarriers.

6.1 Practical Application of This Study

The fabricated nanocarreis have the potential to be used not only for cancer imaging and therapy purpose but also for other type of deseases in case of introduction of appropriate receptor targeted ligand.

REFERENCES

[1] **Siegel, R. L., Miller, K. D., & Jemal, A.** (2019). Cancer statistics, 2019, *CA. Cancer J. Clin.*, vol. 69, pp. 7–34.

[2] **Peppas L. B. & Blanchette, J. O.** (2012). Nanoparticle and targeted systems for cancer therapy, *Advanced Drug Delivery Reviews*, vol. 64, pp. 206–212.

[3] **Sawyers, C.** (2004). Targeted cancer therapy, *Nature*, vol. 432, pp. 294–297.

[4] **National Cancer Institute**. (2010). Radiation Therapy for Cancer - National Cancer Institute, *National Institutes of Health*, Retrieved from https://www.cancer.gov/about-cancer/treatment/types/radiation-therapy

[5] **National Collaborating Centre for Cancer**. (2009). Early and Locally Advanced Breast Cancer: diagnosis and treatment, *NICE Clin. Guidel. No. 80*.

[6] **Wang, A. Z. Langer, R. & Farokhzad, O. C.** (2012). Nanoparticle Delivery of Cancer Drugs, *Annu. Rev. Med.*, vol. 63, pp. 185-198.

[7] **Mura, S. Nicolas, J. & Couvreur, P.** (2013). Stimuli-responsive nanocarriers for drug delivery, *Nat. Mater.*, vol. 12, pp. 991–1003.

[8] **Brigger, I. Dubernet, C. & Couvreur, P.** (2002). Nanoparticles in cancer therapy and diagnosis, *Advanced Drug Delivery Reviews*, vol. 54, no. 5, pp. 631-651.

[9] **Alley, S. C. Okeley, N. M. & Senter, P. D.** (2010). Antibody-drug conjugates: Targeted drug delivery for cancer, *Current Opinion in Chemical Biology*, vol. 14, no. 4, pp. 529-537.

[10] **Bertrand, N. Wu, J. Xu, X. Kamaly, N. & Farokhzad, O. C.** (2014). Cancer nanotechnology: The impact of passive and active targeting in the era of modern cancer biology, *Advanced Drug Delivery Reviews*, vol. 66, pp. 2-25.

[11] **Wilczewska, A. Z. Niemirowicz, K. Markiewicz, K. H. & Car, H.** (2012). Nanoparticles as drug delivery systems, *Pharmacological Reports*, vol. 64, no. 5, pp. 1020–1037.

[12] **Sheikhpour, M. Golbabaie, A. & Kasaeian, A.** (2017). Carbon nanotubes: A review of novel strategies for cancer diagnosis and treatment, *Mater. Sci. Eng. C*, vol. 76, pp. 1289–1304.

[13] **Sunderland, C. J. Steiert, M. Talmadge, J. E. Derfus A. M. & Barry, S. E.** (2006). Targeted nanoparticles for detecting and treating cancer, *Drug Dev. Res.*, vol. 67, no. 1, pp. 70-93.

[14] **dos Santos, G. C. de Oliveira, R. E.C. Ribeiro, R. T. G. Leite, E. A. Lacerda, R. G. Ramaldes, G. A. & de Oliveira, M. C.** (2011). Study of the pilot production process of long-circulating and pH-sensitive liposomes containing cisplatin, *J. Liposome Res.*, vol. 22, no. 3, pp. 60-69.

[15] **Paavola, A. Kilpeläinen, I. Yliruusi, J. & Rosenberg, P.** (2000). Controlled release injectable liposomal gel of ibuprofen for epidural analgesia, *Int. J. Pharm.*, 2000. vol. 199, no. 1, pp. 85-93.

[16] **Turkova, A. Roilides, E. & Sharland M.** (2011). Amphotericin B in neonates: Deoxycholate or lipid formulation as first-line therapy - Is there a 'right' choice?, *Current Opinion in Infectious Diseases*, vol. 24 no. 2, pp.163-71.

[17] **Yukihara, M. Ito, K. Tanoue, O. Goto, K. Matsushita, T. Matsumoto, Y. Masuda, M. Kimura, S. & Ueoka, R.** (2011). Effective Drug Delivery System for Duchenne Muscular Dystrophy Using Hybrid Liposomes Including Gentamicin along with Reduced Toxicity, *Biol. Pharm. Bull.*,vol. 34 no. 5, pp. 712–6.

[18] **Afergan, E. Epstein, H. Dahan, R. Koroukhov, N. Rohekar, K. Danenberg, H.D. Golomb, G.** (2008). Delivery of serotonin to the brain by monocytes following phagocytosis of liposomes, *J. Control. Release*, vol. 132, no. 2, pp. 84–90.

[19] **Jason, P. Peter, M. F. Jing, L. Kerry, S. R. Carmen, J. B. Mark, S. & Tarek M. F.** (2009). PEGylated PLGA nanoparticles for the improved delivery of doxorubicin, *Nanomedicine Nanotechnology, Biol. Med.*, 2009. vol. 5, no. 4, pp. 410–418.

[20] **Edward, T. Jeung-Yeop, S. Yang, W. Kerriann, G. Suresh,K. R. Sonja, D. & Daniel, V. L.** (2007). Antibiotic-conjugated polyacrylate nanoparticles: New opportunities for development of anti-MRSA agents, *Bioorganic Med. Chem. Lett.*,. vo. 17, no. 1, pp. 53–56.

[21] **Pandey, R. Ahmad, Z. Sharma, S. & Khuller, G. K.** (2005). Nano-encapsulation of azole antifungals: Potential applications to improve oral drug delivery, *Int. J. Pharm.*, 2005. vol. 301, no. 1–2, pp. 268–76.

[22] **Agnihotri, S. A. & Aminabhavi, T. M.** (2006). Novel interpenetrating network chitosan-poly(ethylene oxide-g-acrylamide) hydrogel microspheres for the controlled release of capecitabine, *Int. J. Pharm.*, vol. 324 no. 2, pp. 103–15.

[23] **Kam, N. W. S. Liu, Z. & Dai, H.** (2006). Carbon nanotubes as intracellular transporters for proteins and DNA: An investigation of the uptake mechanism and pathway, *Angew. Chemie - Int. Ed.*, vol. 45, no. 4, pp. 577–581.

[24] **Horibata K. Akiko, U. Akio, O. Dai, N. Hiroshi, A. Yoshikazu, K. Akemichi, N. Yuzawa, K. & Honma M.** (2017). Absence of in vivo mutagenicity of multiwalled carbon nanotubes in single intratracheal instillation study using F344 gpt delta rats, *Genes Environ.*, vol. 39, no. 1, pp. 4–8.

[25] **Herzog, E. Casey, A. Lyng, F. M. Chambers, G. Byrne, H. J. & Davoren, M.** (2007). A new approach to the toxicity testing of carbon-based nanomaterials-The clonogenic assay, *Toxicol. Lett.*, vol. 174, no. 1–3, pp. 49–60.

[26] **Da Ros, T. Ostric, A. Andreola, F. Filocamo, M. Pietrogrande, M. Corsolini, F. Stroppiano, M. Bruni, S. Serafino, A. & Fiorito, S.** (2018). Carbon nanotubes as nanovectors for intracellular delivery of laronidase in Mucopolysaccharidosis type I, *Nanoscale*, vol. 10, no. 2, pp. 657–665.

[27] **Meran, M., Akkus, P. D. Kurkcuoglu, O. Baysak, E. Hizal, G. Haciosmanoglu, E. Unlu, A. Karatepe, N. & Guner, F. S.** (2018). Noncovalent Pyrene-Polyethylene Glycol Coatings of Carbon Nanotubes Achieve in Vitro Biocompatibility, *Langmuir*, vol. 34, no. 40, pp. 12071–12082.

[28] **Maniecki, T. Shtyka, O. Mierczynski, P. Ciesielski, R. Czylkowska, A. Leyko, J. Mitukiewicz, G. Dubkov, S. & Gromov, D.** (2018). Carbon Nanotubes: Properties, Synthesis, and Application, *Fibre Chem.*, vol. 50. no. 4.

[29] **Dai, H.** (2002). Carbon nanotubes: Synthesis, integration, and properties, *Acc. Chem. Res.*, 2002. vol. 35, no. 12, pp. 1035–1044.

[30] **Hagen, A. & Hertel, T.** (2003). Quantitative analysis of optical spectra from individual single-wall carbon nanotubes, *Nano Lett.*, vol. 3, no. 3, pp. 383–388.

[31] **Lasjaunias, J. C.** (2003). Thermal properties of carbon nanotubes, *Comptes Rendus Physique*. 2003. vol. 4, no. 9, pp. 1047–1054.

[32] **Huang, X. Zhi, C, & Jiang, P.** (2012). Toward effective synergetic effects from graphene nanoplatelets and carbon nanotubes on thermal conductivity of ultrahigh volume fraction nanocarbon epoxy composites, *J. Phys. Chem. C*, vol. 116, no. 44, pp. 23812–23820.

[33] **Zhou, C. Kong, J. & Dai, H.** (2000). Electrical measurements of individual semiconducting single-walled carbon nanotubes of various diameters, *Appl. Phys. Lett.*, vol. 76, no. 12, 10.1063/1.126107.

[34] **Jang, W. Y. Kulkarni, N. N. Shih, C. K. & Yao, Z.** (2004). Electrical characterization of individual carbon nanotubes grown in nanoporous anodic alumina templates, *Appl. Phys. Lett.*, 2004. vol. 84, no. 7, 10.1063/1.1646752.

[35] **Liu, Z. Tabakman, S. Welsher, K. & Dai, H.** (2009). Carbon nanotubes in biology and medicine: In vitro and in vivo detection, imaging and drug delivery, *Nano Res.*, vol. 2, no. 2, pp. 85–120.

[36] **Saito, R. Hofmann, M. Dresselhaus, G. Jorio, A. & Dresselhaus, M. S.** (2011). Raman spectroscopy of graphene and carbon nanotubes, *Adv. Phys.*, vol. 60, no. 3, pp. 413–550.

[37] **Hong, G. Diao, S. Antaris, A. L. & Dai, H.** (2015). Carbon Nanomaterials for Biological Imaging and Nanomedicinal Therapy, *Chem. Rev.*, vol. 115, no. 19, pp. 10816–10906.

[38] **Luo, G. Yu, X. Jin, C. Yang, F. Fu, D. Long, J. Xu, J. Zhan, C. & Lu, W.** (2010). LyP-1-conjugated nanoparticles for targeting drug delivery to lymphatic metastatic tumors, *Int. J. Pharm.*, vol. 385, no. 1–2, pp. 150–6.

[39] **Chen, Z. Meng, H. Xing, G. Yuan, H. Zhao, F. Liu, R. Chang, X. Gao, X. Wang, T. Jia, G. Ye, C. Chai, Z. & Zhao, Y.** (2008). Age-related differences in pulmonary and cardiovascular responses to SiO_2 nanoparticle inhalation: Nanotoxicity has susceptible population, *Environ. Sci. Technol.*, vol. 42, no. 23, pp. 8985–92.

[40] **Staii, C. Johnson, A. T. Chen, M. & Gelperin, A.** (2006). DNA-decorated carbon nanotubes for chemical sensing, in *Physica Status Solidi (B) Basic Research*, vol. 5, no. 9, pp. 1774–8.

[41] **Li, J. Ng, H. T. Cassell, A. Fan, W. Chen, H. Ye, Q. Koehne, J. Han, J. & Meyyappan, M.** (2003). Carbon nanotube nanoelectrode array for ultrasensitive DNA detection, *Nano Lett.*, vol. 3, no. 5, 597–602.

[42] **Choi, Y. Olsen, T. J. Sims, P. C. Moody, I. S. Corso, B. L. Dang, M. N. Weiss, G. A. & Collins, P. G.** (2013). Dissecting single-molecule signal transduction in carbon nanotube circuits with protein engineering, *Nano Lett.*, vol. 13, no. 2, pp. 625–31.

[43] **So, H. M. Won, K. Kim, Y. H. Kim, B. K. Ryu, B. H. Na, P. S. Kim, H. & Lee, J. O.** (2005). Single-walled carbon nanotube biosensors using aptamers as molecular recognition elements, *J. Am. Chem. Soc.*, vol. 127, no. 34, pp. 11906–7.

[44] **Chen, Z. Tabakman, S. M. Goodwin, A. P. Kattah, M. G. Daranciang, D. Wang, X. Zhang, G. Li, X. Liu, Z. Utz, P. J. Jiang, K. Fan, S. & Dai, H.** (2008). Protein microarrays with carbon nanotubes as multicolor Raman labels, *Nat. Biotechnol.*, vol. 26, no. 11, pp. 1285–92.

[45] **Liu, S. & Liu, Y.** (2011). Classical Molecular Dynamics, in *Modeling and Simulation for Microelectronic Packaging Assembly*, Chapter 19, pp. 234–5.

[46] **González, M. A.** (2011). Force fields and molecular dynamics simulations, *École thématique la Société Française la Neutron.*, vol. 12, pp. 169–200

[47] **Yao, H. J. Y. Zhang, G. Sun, L. & Liu, Y.** (2014).The effect of hyaluronic acid functionalized carbon nanotubes loaded with salinomycin on gastric cancer stem cells, *Biomaterials*, vol. 35, no. 33, pp. 9208–9223.

[48] **Minati, L. Antonini, V. Dalla Serra, M. & Speranza G.** (2012). Multifunctional branched gold-carbon nanotube hybrid for cell imaging and drug delivery, *Langmuir*, vol. 28, no. 45, pp. 15900–15906.

[49] **Welsher, K., Liu, Z. Sherlock, S. P. Robinson, J. T. Chen, Z. Daranciang, D. & Dai H.** (2009). A route to brightly fluorescent carbon nanotubes for near-infrared imaging in mice, *Nat. Nanotechnol.*, vol. 4, no. 11, pp. 773–780.

[50] **Kumar, S. Rani, R. Dilbaghi, N. Tankeshwar, K. & K. Kim, H.** (2017). Carbon nanotubes: A novel material for multifaceted applications in human healthcare, *Chem. Soc. Rev.*, vol. 46, no. 1, pp. 158–196.

[51] **Chen, B. Zhang, H. Zhai, C. Du, N. Sun, C. Xue, J. Yang, D. Huang, H. Zhang, B. Xiec Q. & Wu, Y.** (2010). Carbon nanotube-based magnetic-fluorescent nanohybrids as highly efficient contrast agents for multimodal cellular imaging, *J. Mater. Chem.*, vol. 20, no. 44, pp. 9895–9902.

[52] **Meran, M. Baysak, E. Hizal, G. Haciosmanoglu, E. Unlu, A. Karatepe, N. & Guner, F. S.** (2018). Noncovalent Pyrene-Polyethylene Glycol Coatings of Carbon Nanotubes Achieve in Vitro Biocompatibility, *Langmuir*, vol. 34, no. 40, pp. 12071–12082.

[53] **Unlu, A. Meran, M. Dinc, B. Karatepe, N. Bektas, M. & Guner, F. S.** (2018). Cytotoxicity of doxrubicin loaded single-walled carbon nanotubes, *Mol. Biol. Rep.*, vol. 45, no. 4, pp. 523–531.

[54] **Bianco, A. Kostarelos, K. Partidos, C. D. & Prato, M.** (2005). Biomedical applications of functionalised carbon nanotubes, *Chem. Commun.*, no. 5, pp. 571–577.

[55] **Demir, E. & Marcos, R.** (2018). Toxic and genotoxic effects of graphene and multi-walled carbon nanotubes, *J. Toxicol. Environ. Heal. Part A*, vol. 81, no. 14, pp. 645–660.

[56] **Yu, S. Su, X. Du, J. Wang, J. Gao, Y. Zhang, L. Chen, L. Yang, Y. & Liu, X.** (2018). The cytotoxicity of water-soluble carbon nanotubes on human embryonic kidney and liver cancer cells, *New Carbon Mater.*, vol. 33, no. 1, pp. 36–45, 2018.

[57] **Cui, D. Tian, F. Ozkan, C. S. Wang, M. & Gao, H.** (2005). Effect of single wall carbon nanotubes on human HEK293 cells, *Toxicol. Lett.*, vol. 155, no. 1, pp. 73–85.

[58] **Sharma, C. S. Sarkar, S. Periyakaruppan, A. Barr, J. Wise, K. Thomas, R. Wilson, B. L. Ramesh, G. T.** (2007). Single-Walled Carbon Nanotubes Induces Oxidative Stress in Rat Lung Epithelial Cells, *J Nanosci Nanotechnol*, vol. 7, no. 7, pp. 2466–2472.

[59] **Knop, K. Hoogenboom, R. Fischer, D. & Schubert, U. S.** (2010). Poly(ethylene glycol) in drug delivery: Pros and cons as well as potential alternatives, *Angew. Chemie - Int. Ed.*, vol. 49, no. 36, pp. 6288–6308.

[60] **Prencipe, G. Tabakman, S. M. Welsher, K. Liu, Z. Goodwin, A. P. Zhang, L. Henry, J. & Dai, H.** (2009). PEG branched polymer for functionalization of nanomaterials with ultralong blood circulation, *J. Am. Chem. Soc.*, vol. 131, no. 13, pp. 4783–4787.

[61] **Bottini, M. Rosato, N. & Bottini, N.** (2011). PEG-modified carbon nanotubes in biomedicine: Current status and challenges ahead, *Biomacromolecules*, vol. 12, no. 10, pp. 3381–3393.

[62] **Chen, R. J. Zhang, Y. Wang, D. & Dai, H.** (2001). Noncovalent Sidewall Functionalization of Single-Walled Carbon Nanotubes for Protein Immobilization, *J. Am. Chem. Soc.*, no. 123, pp. 3838–3839, 2001.

[63] **Chen, G. Wright, P. M. Geng, J. Mantovani, G. & Haddleton, D. M.** (2008). Tunable thermoresponsive water-dispersed multiwalled carbon nanotubes, *Chem. Commun.*, no. 9, pp. 1097–1099.

[64] **Gref, J. M. R. Domp, A. Quellec, P. Blunk, T. Muller, R.H. & Verbavatz, R. L.** (1995). The controlled intravenous delivery of drugs using PEG coated sterically stabilized nanospheres, *Adv. Drug Del. Rev*, vol. 16, no. 95, p. 215.

[65] **Peracchia, M.T. Vauthier, C. Passirani, C. Couvreur, P. & Labarre, D.** (1997). Complement consumption by poly(ethylene glycol) in different conformations chemically coupled to poly(isobutyl 2-cyanoacrylate) nanoparticles, *Life Sci.*, vol. 61, no. 7, pp. 749–761.

[66] **Liu, Z. Davis, C. Cai, W. He, L. Chen, X. & Dai, H.** (2008). Circulation and long-term fate of functionalized, biocompatible single-walled carbon nanotubes in mice probed by Raman spectroscopy, *Proc. Natl. Acad. Sci.*, vol. 105, no. 5, pp. 1410–1415.

[67] **Kostarelos, K.** (2008). The long and short of carbon nanotube toxicity, *Nat. Biotechnol.*, vol. 26, no. 7, pp. 774–776.

[68] **Chen, Z. Kobashi, K. Rauwald, U. Booker, R. Fan, H. Hwang, W. F. & Tour, J. M.** (2006). Soluble Ultra-Short Single-Walled Carbon Nanotubes, *J. Am. Chem. Soc.*, no. 19, pp. 10568–10571.

[69] **Yau, H. C. Bayazit, M. K. & Steinke, J. H. G.** (2014). Diamond Rings or Dumbbells: Controlling the Structure of Poly(ethylene glycol) − Fullerene [60] Adducts by Varying Linking Chain Length, *Macromolecules*, vol. 47, pp. 4870–4875.

[70] **Abdelhameed, M. Martir, D. R. Chen, S. Xu, W. Z. Oyeneye, O. O. Chakrabarti, S. Colman, E. Z. & Charpentier P. A.** (2018). Tuning the Optical Properties of Silicon Quantum Dots via Surface Functionalization with Conjugated Aromatic Fluorophores, *Sci. Rep.*, vol. 8, no. 1, pp. 1–10.

[71] **Baskaran, X. Vigila, A. V. G. Parimelazhagan, T. Muralidhara-Rao, D. & Zhang, S.** (2016). Biosynthesis, characterization, and evaluation of bioactivities of leaf extract-mediated biocompatible silver nanoparticles from an early tracheophyte, Pteris tripartita Sw, *Int. J. Nanomedicine*, vol. 11, pp. 5789–5805.

[72] **Tasis, D. Tagmatarchis, N. Bianco, A. & Prato, M.** (2006). Chemistry of carbon nanotubes, *Chem. Rev.*, vol. 106, no. 3, pp. 1105–1136.

[73] **Besteman, K. Lee, J. O. Wiertz, F. G. M. Heering, H. A. & Dekker, C.** (2003). Enzyme-coated carbon nanotubes as single-molecule biosensors, *Nano Lett.*, vol. 3, no. 6, pp. 727–730.

[74] **Durmaz, H. Dag, A. Tunca, U. & Hizal, G.** (2012). Synthesis and characterization of pyrene bearing amphiphilic miktoarm star polymer and its noncovalent interactions with multiwalled carbon nanotubes, *J. Polym. Sci. Part A Polym. Chem.*, vol. 50, no. 12, pp. 2406–2414.

[75] **Moreau, V. Tatin, F. Varon, C. & Ge, E.** (2003). Actin Can Reorganize into Podosomes in Aortic Endothelial Cells , a Process Controlled by Cdc42 and RhoA Actin Can Reorganize into Podosomes in Aortic Endothelial Cells , a Process Controlled by Cdc42 and RhoA, *Mol. Cell. Biol.*, vol. 23, no. 19, pp. 6809–6822.

[76] **Singh, A. V. Mehta, K. K. Worley, K. Dordick, J. S. Kane, J. R. & Wan,L. Q.** (2014). Carbon nanotube-induced loss of multicellular chirality on micropatterned substrate is mediated by oxidative stress, *ACS Nano*, vol. 8, no. 3, pp. 2196–2205.

[77] **Cai, H. & Harrison, D. G.** (2000). Endothelial Dysfunction in Cardiovascular Diseases: The Role of Oxidant Stress, *Circ. Res.*, 2000. vol. 87, no. 10, pp. 840–4.

[78] **Bobadilla, A. D. Samuel, E. L. G. Tour, J. M. & Seminario, J. M.** (2013). Calculating the hydrodynamic volume of poly(ethylene oxylated) single-walled carbon nanotubes and hydrophilic carbon clusters, *J. Phys. Chem. B*, vol. 117, no. 1, pp. 343–354.

[79] **Walker, V. G. Li, Z. Hulderman, T. Schwegler-Berry, D. Kashon, M. L. & Simeonova, P. P.** (2009). Potential in vitro effects of carbon nanotubes on human aortic endothelial cells, *Toxicol. Appl. Pharmacol.*, vol. 236, no. 3, pp. 319–328.

[80] **Feazell, R. P. Nakayama-Ratchford, N. Dai, H. & Lippard, S. J.** (2007). Soluble single-walled carbon nanotubes as longboat delivery systems for platinum(IV) anticancer drug design, *J. Am. Chem. Soc.*, vol. 129, no. 27, pp. 8438–8439.

[81] **Bottini, M. Cerignoli, F. Dawson, M. I. Magrini, A. Rosato, N. & Mustelin, T.** (2006). Full-length single-walled carbon nanotubes decorated with streptavidin-conjugated quantum dots as multivalent intracellular fluorescent nanoprobes, *Biomacromolecules*, 2006. vol. 7, no. 8, pp. 2259–63.

[82] **Dinan, N. M. Atyabi, F. Rouini, M. R. Amini, M. Golabchifar, A. A. & Dinarvand, R**. (2014). Doxorubicin loaded folate-targeted carbon nanotubes: Preparation, cellular internalization, in vitro cytotoxicity and disposition kinetic study in the isolated perfused rat liver, *Mater. Sci. Eng. C*. vol. 39, pp. 47–55.

[83] **Gewirtz, D. A.** (1999). A critical evaluation of the mechanisms of action proposed for the antitumor effects of the anthracycline antibiotics adriamycin and daunorubicin, *Biochem. Pharmacol.*, vol. 57, no. 7, pp. 727–41.

[84] **Wallace, K. B.** (2007). Adriamycin-induced interference with cardiac mitochondrial calcium homeostasis, in *Cardiovascular Toxicology*, vol. 7, no. 2, pp. 101–7.

[85] **Carvalho, C. Santos, R. X. Cardoso, S. Correia, S. Oliveira, P. J. Santos, M. S. & Moreira, P. I.** (2009). Doxorubicin: The Good, the Bad and the Ugly Effect, *Curr. Med. Chem.*, vol. 16, no. 25, pp. 3267–85.

[86] **Rafiyath, S. M. Rasul, M. Lee, B. Wei, G. Lamba, G. &Liu, D.** (2012). Comparison of safety and toxicity of liposomal doxorubicin vs. conventional anthracyclines: a meta-analysis, *Exp. Hematol. Oncol.*, vol. 1, no. 1, pp. 10.

[87] **Low, P. S. & Kularatne, S. A.** (2009). Folate-targeted therapeutic and imaging agents for cancer, *Current Opinion in Chemical Biology*, vol. 13, no. 3, pp. 256–62.

[88] **Vassie, J. A. Whitelock, J. M. & Lord, M. S.** (2017).Endocytosis of cerium oxide nanoparticles and modulation of reactive oxygen species in human ovarian and colon cancer cells, *Acta Biomater.*, vol. 50, pp. 127–141.

[89] **Ellison M. D. & Chorney, M.** (2016). Reaction of folic acid with single-walled carbon nanotubes, *Surf. Sci.*, vol. 652, pp. 300–303.

[90] **Sahoo, N. G. Bao, H. Pan, Y. Pal, M. Kakran, M. Cheng, H. K. Li, L. & Tan, L. P.** (2011). Functionalized carbon nanomaterials as nanocarriers for loading and delivery of a poorly water-soluble anticancer drug: A comparative study, *Chem. Commun.*, vol. 47, no. 18, pp. 5235–7.

[91] **Lv, S. Tang, Z. Li, M. Lin, J. Song, W. Liu, H. Huang, Y. Zhang, Y. & Chen, X.** (2014). Co-delivery of doxorubicin and paclitaxel by PEG-polypeptide nanovehicle for the treatment of non-small cell lung cancer, *Biomaterials*, vol. 35, no. 23, pp. 6118–6129.

[92] **Liu, Z. Sun, X. Nakayama-Ratchford, N. & Dai, H.** (2007). Supramolecular chemistry on water- Soluble carbon nanotubes for drug loading and delivery, *ACS Nano*, vol. 1, no. 1, pp. 50–6.

[93] **Heister, E. Neves, V. Tilmaciu, C. Lipert K. Beltran, V. S. Coley, H. M. Silva, S. R. P. & McFadden, J.** (2009). Triple functionalisation of single-walled carbon nanotubes with doxorubicin, a monoclonal antibody, and a fluorescent marker for targeted cancer therapy, *Carbon N. Y.*, vol 47, no 9, pp. 2152–2160.

[94] **Niu, L. Meng, L. & Lu, Q.** (2013). Folate-conjugated PEG on single walled carbon nanotubes for targeting delivery of doxorubicin to cancer cells, *Macromol. Biosci.*, vol. 13, no. 6, pp. 735–44.

[95] **Higuchi, T.** (1963). Mechanism of sustained- action medication. Theoretical analysis of rate of release of solid drugs dispersed in solid matrices, *J. Pharm. Sci.*, vol. 52, pp. 1145–9.

[96] **Korsmeyer, R. W. Gurny, R. Doelker, E. Buri, P. & Peppas, N. A.** (1983). Mechanisms of potassium chloride release from compressed, hydrophilic, polymeric matrices: Effect of entrapped air, *J. Pharm. Sci.*, 1983. vol. 72, no. 10, pp. 1189–91.

[97] **Tan, J. M. Karthivashan, G. Gani, S. A. Fakurazi, S. & Hussein, M. Z.** (2016). In vitro drug release characteristic and cytotoxic activity of silibinin-loaded single walled carbon nanotubes functionalized with biocompatible polymers, *Chem. Cent. J.*, vol. 10, pp. 81.

[98] **Lu, Y. J. Wei, K. C. Ma, C. C. M. Yang, S. Y. & Chen, J. P.** (2012). Dual targeted delivery of doxorubicin to cancer cells using folate-conjugated magnetic multi-walled carbon nanotubes, *Colloids Surfaces B Biointerfaces*, vol. 89, pp. 1–9.

[99] **Rani, K. & Paliwal, S.** (2014). A Review on Targeted Drug Delivery: its Entire Focus on Advanced Therapeutics and Diagnostics, *Sch. J. Appl. Med. Sci.*, vol. 2, no. 1C, pp. 328–331.

[100] **Zhang, H. Li, F. Yi, J. Gu, C. Fan, L. Qiao, Y. Tao, Y. Cheng, C. & Wu, H.** (2011). Folate-decorated maleilated pullulan-doxorubicin conjugate for active tumor-targeted drug delivery, *Eur. J. Pharm. Sci.*, vol. 42 no. 5, pp. 517–26.

[101] **Kim, S. H. Jeong, J. H. Chun, K. W. & Park, T. G.** (2005). Target-specific cellular uptake of PLGA nanoparticles coated with poly(L-lysine)-poly(ethylene glycol)-folate conjugate, *Langmuir*, vol. 21, no. 19, pp. 8852–7.

[102] **Mawhinney, D. B. Naumenko, V. Kuznetsova, A. Yates, J. T. Liu, J. & Smalley, R. E**. (2000). Surface defect site density on single walled carbon nanotubes by titration, *Chem. Phys. Lett.*, vol. 324, no 1–3, pp. 213–216.

[103] **Volpe, M. & Cleri, F.** (2003). Role of surface chemistry in hydrogen adsorption in single-wall carbon nanotubes, *Chem. Phys. Lett.*, vol. 371, no. 3–4, pp. 476–482.

[104] **Ding, F.** (2005). Theoretical study of the stability of defects in single-walled carbon nanotubes as a function of their distance from the nanotube end, *Phys. Rev. B - Condens. Matter Mater. Phys.*, vol. 72, no. 24, pp. 1–21.

[105] **Wei, L. Yanhui, F. Jia, P. & Xinxin, Z.** (2012). Effects of Stone-Wales Defects on the Thermal Conductivity of Carbon Nanotubes, *J. Heat Transfer*, vol. 134, no. 9, p. 092401–5.

[106] **Charlier, J. C.** (2002). Defects in carbon nanotubes., *Accounts of chemical research*, vol. 35, no. 12. pp. 1063–9.

[107] **Kumar M. & Ando, Y.** (2010). Chemical Vapor Deposition of Carbon Nanotubes: A Review on Growth Mechanism and Mass Production, *J. Nanosci. Nanotechnol.*, vol. 10, no. 6, pp. 3739–58.

[108] **Eatemadi, A. Daraee, H. Karimkhanloo, H. Kouhi, M. Zarghami, N. Akbarzadeh, A. Abasi, M. Hanifehpour, Y. Joo, S. W. (**2014). Carbon nanotubes: properties, synthesis, purification, and medical applications., *Nanoscale Res. Lett.*, vol. 9, no. 1, pp. 393.

[109] **Bonard, J. M. Stora, T. Salvetat, J. P. Maier, F. Stokli, T. Duschl, C. Forro, L. Heer, W. A. & Chatelain, A.** (1997). Purification and size-selection of carbon nanotubes, *Adv. Mater.*, vol. 9, no. 10, pp 827–831.

[110] **Schmucker, W. Klumpp, S. Hennrich, F. Kappes, M. & Wagenknecht, H. A.** (2013). A simple pyrene 'click'-type modification of DNA affects solubilisation and photoluminescence of single-walled carbon nanotubes, *RSC Adv.*, vol. 3, no. 18, pp. 6331–6333.

CURRICULUM VITAE

Name Surname	: Mehdi PARTOVI MERAN
Place and Date of Birth	: Iran – 10.07.1981
E-Mail	: mmeran@itu.edu.tr

EDUCATION :

- **B.Sc.** : 2006, University of Tabriz, Faculty of Chemistry, Department of Applied Chemistry
- **M.Sc.** : 2011, Sahand University of Technology, Faculty of Chemical Engineering, Department of Polymer Engineering

PROFESSIONAL EXPERIENCE AND REWARDS:

- Research Assistant at TÜBİTAK 133S334 No. 3501. Investigation of the Three-Dimensional Structure of the Nicotinamide Adenine Dexline in the ADP-Ribose Polymers and ADP-Ribozylated Toxins by Using the Theoretical and Experimental Methods 1953 Nobel Prize for Physics
- TÜBAP 2017/67 Project (Trakya University) Research Assistan Investigation of Functionalized Carbon Nanotube Materials in Biological Environment
- 2018.05.01 Animal Experiments Ethics Study (Trakya University) Research Assistant Investigation of Blood Circulation Time Nanoparticles coated with PEG
- Language Skills English (TOEFL iBT: 80) Turkish, Persian, Azeri

PUBLICATIONS, PRESENTATIONS AND PATENTS ON THE THESIS:

- **Meran, M.** Akkus, P. D. Kurkcuoglu, O. Baysak, E. Hizal, G Haciosmanoglu, E. Unlu, A. Karatepe, N. Güner, F. S. (2018). Non-covalent Pyrene-PEG Coatings of

Carbon Nanotubes Achieve In Vitro Biocompatibility *Langmuir*, DOI: 10.1021/acs.langmuir.8b00971

- Ünlü, A. **Meran, M.** Dinc, B. Karatepe, N. Bektaş, M. Güner F. S: (2018). Cytotoxicity of doxrubicin loaded single-walled carbon nanotubes" *Molecular Biology Reports* DOI 10.1007/s11033-018-4189-5

- **Mehdi Meran,** F. Seniha Guner, Ozge Kurkcuoglu "Molecular Dynamics Studies of Functionalized Pyrene Adsorption on Single-Walled Carbon Nanotubes with Structural Defects" *5. BAU Drug Desing Congress, 2018, İstanbul*

- **Mehdi Meran,** Elif Baysak, Ozge Kurkcuoglu, Gurkan Hizal, Nilgun Yavuz, F. Seniha Guner "Pyrene-functionalized Carbon Nanotubes as Emerging Nanocarriers: Insight From Experimental and Molecular Dynamic Simulation" *1. Biological and Chemical Sience Kongresi,2018, Ankara*

- **Mehdi Meran,** Pelin Deniz Akkus, Ozge Kurkcuoglu, Nilgun Karatepe, Gurkan Hizal, F. Seniha Guner "Doxorubicin Loaded Carbon Nanotubes as Multimodal Nanocarriers for Cancer Treatment" *5. BAU Drug Desing Congress, 2017, İstanbul*

- **Mehdi Meran**, Bircan Dinç, Ayhan Ünlü "Design of High-affinity PARP-2 Inhibitors by Dynamic Structure-Based Pharmacophore Approach" *5. BAU Drug Desing Congress, 2017, İstanbul*

- **Mehdi Meran,** Pelin Deniz Akkus, Ozge Kurkcuoglu, Nilgun Karatepe, Gurkan Hizal, F. Seniha Guner "PEG modified single-walled carbon nanotubes: Molecular dynamics simulations and experimental approach" PPM 2017, Kuşadası, İzmir

- **Mehdi Meran,** Ayhan Ünlü, Ebru Hacıosmanoğlu, Gürkan Hızal, Nilgün Yavuz, Pelin Deniz Akkuş, Özge Kürkçüoğlu, F. Seniha Güner "Preparation of PEG Modified Single-Walled Carbon Nanotubes: CNT and PEG Chain Length Effect" *World Polymer Congress 2016, İstanbul*

- Ayhan Ünlü, **Mehdi Meran,** Gürkan Hızal, Nilgün Yavuz, F. Seniha Güner, "Preparation of PEG Modified Single-Walled Carbon Nanotubes: CNT and PEG Chain Length Effect" *World Polymer Congress 2016, İstanbul*

- **Mehdi Meran,** Gonca Akdere, Elif Baysak, Gürkan Hızal, Ayhan Ünlü, F. Seniha Güner, "PEG ile Fonksiyonel Hale Getirilmiş Karbon Nanotüp Malzemelerin Sentezi Ve Bağlanma Oraninin İncelenmesi" *12. Ulusal Kimya Mühendisliği Kongresi, 2016, İzmir*